



Michael Mascara, MSc

A Bonded Particle Model to Predict the Mechanical Properties of Viscoelastic Materials

DOCTORAL THESIS

to achieve the university degree of
Doktor der technischen Wissenschaften

submitted to

Graz University of Technology

Supervisor

Stefan Radl, Assoc.Prof. Dipl.-Ing. Dr.techn.
Institute of Chemical and Process Engineering

Graz, April 2024

Mentor

Christoph Kloss, Dipl.-Ing., Dr.techn.
DCS Computing GmbH
Linz

First Assessor

Stefan Pirker, Assoc.Prof., Dipl.-Ing. Dr.techn.
Department of Particulate Flow Modelling
Johannes Kepler University
Linz

Second Assessor

Dr. J.A. (Joshua) Dijksman
Faculty of Science
University of Amsterdam
Amsterdam

Affidavit

I declare that I have authored this thesis independently, that I have not used other than the declared sources/resources, and that I have explicitly indicated all material which has been quoted either literally or by content from the sources used. The text document uploaded to tugrazonline is identical to the present doctoral thesis.

Acknowledgements

I want to thank my supervisor, Prof. Stefan Radl, and my mentor, Dr. Christoph Kloss, for their continuous support throughout the entire project, for which I will always be grateful.

Special thanks go to the CALIPER¹ project coordinator, Dr. Joshua Dijksman, who is also the second assessor of this thesis, for being supportive of my research as well as being a great scientist. I want to thank the other researchers of CALIPER, with whom I shared moments that I will remember for a long time.

I acknowledge the first assessor of the thesis, Prof. Stefan Pirker, for taking the interest and the time to assess my work.

I am also very thankful to the colleagues at DCS Computing, for they have shared their expertise with me without hesitation, which helped me advancing in my project.

I want to thank my loving family and friends for laughing with me at my best and being by my side at my worst.

Lastly, a special mention to this PhD. If I had never started this journey, I would have never met the love of my life, my biggest fan, my best friend, Miriam.

¹This project is funded through Marie SKŁODOWSKA-CURIE Innovative Training Network **CALIPER** of the European Union's Horizon 2020 Programme H2020 under REA grant agreement No.812638.

Abstract

The goal of this thesis is to implement and validate a novel Discrete Element Method model to characterize the behavior of viscoelastic materials in the most general way possible, from single grains to more continuous media. Viscoelastic materials can come in different flavours and properties, they can be continuous, like a paste, or discrete, like hydrogel spheres.

To be able to obtain a reliable solver, two different models have been implemented, namely the Burgers model and the Generalized Maxwell model. The Burgers model is investigated first by means of a test case, used to obtain the rheological properties of a given viscoelastic material, the storage shear modulus G' and the loss shear modulus G'' . The test consists of a cubic lattice, sheared with a periodic motion, to mimic the effect of a shear rheometer. After appropriate filtering of the stress response, the rheological properties are obtained, highlighting the effect of the lattice geometry, as well as the particle size, on the accuracy of the model. Moreover, the Burgers parameters are calibrated by analytically fitting the experimental dataset, showing its limitations. After completing a frequency sweep, the simulated G' and G'' show a relatively large error, around 25% for G' for example. For this reason, the Generalized Maxwell Model has been implemented. The calibration procedure is performed in the same fashion as for the Burgers model. Moreover, the tangential micro-contact parameters are scaled with respect to the normal ones. This scaling parameter, called α , is calibrated by minimizing the Root Mean Square Error between simulation and experimental data, giving errors below 10% in both G' and G'' for a large dataset. Additionally, a full ring plate-plate rheometer setup is simulated, and the simulation is compared with the given experimental dataset, again finding a good agreement.

Given the good accuracy of the model in simulating a continuous material by means of discrete bonded particles, the next challenge is to be able to describe the mechanical properties of a single grain, in this case a hydrogel sphere. The use of hydrogels has exponentially increased in recent years in many fields, such as biology, medicine, pharmaceuticals, agriculture, and more. These materials are so widely used because their mechanical properties change drastically with the different chemical compositions of the constituent polymer chains, making them highly versatile for different applications. The model used in the Generalized Maxwell model. A benchmark test, namely an oscillatory compression test on a single hydrogel, is used to calibrate the model parameters, obtaining a good agreement on the material's rheological properties. Specifically, it is shown that the Tensile Storage modulus [Pa] (E') and Tensile Loss modulus [Pa] (E''), obtained in the simulation match the experimental data with a small relative error, around 3%, for E' and 11% for E'' . This result aligns with recent work on numerical modeling of hydrogels, introducing a novel approach with bonded particles and a viscoelastic consti-

tutive relation that can capture a wide range of applications thanks to the higher number of elements. Moreover, we validate the model on a particle-particle compression test by comparing the simulation output with the contact force in the compression direction, again obtaining promising results.

Contents

1. Introduction	3
1.1. Motivation	3
1.1.1. Viscoelastic paste	3
1.1.2. Hydrogel sphere	3
1.2. Viscoelastic materials	4
1.3. Numerical models	9
1.4. Goals and Contents	13
1.5. Contributions to publications	14
1.5.1. Publication on the viscoelastic paste calibration and validation . .	14
1.5.2. Publication on the hydrogel experimental calibration and validation	14
2. Implementation and validation of a Bonded Particle Model to predict the Rheology of viscoelastic materials	15
2.1. Introduction	15
2.2. Methodology	16
2.2.1. Modified BPM with Burgers relation	17
2.2.2. The generalized Maxwell model	20
2.2.3. Simulation test case	21
2.3. Calibration strategy	28
2.3.1. Limitation of Burgers model	31
2.3.2. Fitting quality of a generalized Maxwell model	33
2.3.3. Calibrating the normal-to-shear scaling parameter	34
2.4. Oscillatory plate-plate shear rheometer simulation	37
2.5. Conclusions	40
3. A Viscoelastic Bonded Particle Model to Predict Rheology and Mechanical Properties of Hydrogel Spheres	43
3.1. Introduction	43
3.2. Methodology	44
3.2.1. Bonded Particle Model	44
3.2.2. Generalized Maxwell Model	45
3.3. Experimental setups on Hydrogel spheres	48
3.3.1. Cyclic compression-extension	48
3.3.2. Particle-Particle compression	50
3.4. DEM simulation	53
3.4.1. Parameters calibration	53
3.4.2. Calibration theory	53

3.4.3. Simulation of the single sphere cyclic compression-extension test	56
3.4.4. Validation of the particle-particle compression test	60
3.5. Conclusions and Outlook	64
4. Additional work on hydrogels	67
4.1. Simulation of coefficient of restitution	67
4.2. Low impact velocity simulation	69
4.2.1. Prediction of the impact velocity using a variable coefficient of restitution	72
4.3. Hydrogel Particle-particle shear test	74
4.3.1. Simulation setup, output and comparison with experiment	74
4.3.2. Numerical friction	77
5. Conclusions and outlook	81
5.1. Conclusions from chapter 2	81
5.2. Conclusions from chapter 3 and chapter 4	82
5.3. Model limitations and outlook	82
Appendix A. Validation of the bonded generalized Maxwell model	85
Appendix B. Post processing and modelling codes	89
Bibliography	91

List of Figures

1.1. Shear flow	4
1.2. Shear deformation	5
1.3. Stress response of different materials under oscillatory strain input	8
1.4. Hertz model in DEM	11
2.1. Graphic representation of the viscoelastic Bonded Particle Model	16
2.2. Generalized Maxwell model schematics	20
2.3. Lattice configuration for initial model assessment	22
2.4. Raw stress response of lattice test case	23
2.5. Fast Fourier Transform of the lattice test case stress response	23
2.6. Viscoelastic stress response of the lattice test case	24
2.7. Spatial convergence of a simple cubic lattice configuration	25
2.8. Uniaxial compression of the lattice test case	26
2.9. Spatial convergence of a Face Centered Cube lattice configuration	28
2.10. Spatial convergence in a creep recovery test	29
2.11. Experimental dataset of a viscoelastic paste used for calibrating the model parameters	30
2.12. Fitting quality of the Burgers model	32
2.13. Improved fitting quality of the Burgers model	32
2.14. Simulation output of the Burgers model with calibrated parameters . . .	34
2.15. Fitting quality of the generalized Maxwell model with 3 elements	34
2.16. Fitting quality of the generalized Maxwell model with 4 elements	35
2.17. Simulation output of the generalized maxwell model with calibrated pa- rameters	37
2.18. Graphical representation of a plate-plate rheometer	38
2.19. Simulation domain for the ring shear rheometer	39
2.20. Simulation output of the ring shear rheometer vs experimental data of material 1	40
2.21. Simulation output of the ring shear rheometer vs experimental data of material 2	40
3.1. Schematic representation of the viscoelastic element forming the Gener- alized Maxwell Model.	45
3.2. Flowchart of the algorithm used to compute particle-particle interactions. .	47
3.3. Experimental setup for the oscillatory compression of a single hydrogel sphere	49
3.4. Particular of the hydrogel sphere placement in the experimental setup . .	50

3.5. Rheological properties measured from the oscillatory compression of a single hydrogel sphere	51
3.6. a) Schematics on the particle-particle compression test. b) Particles under compression during the experiment	52
3.7. Analytical fitting of the oscillatory compression data using the Generalized Maxwell model.	55
3.8. Discretization of the hydrogel sphere used to simulate the oscillatory compression experiment.	57
3.9. Global vertical force measured on a single hydrogel sphere linear compression simulation	58
3.10. Rheological properties of the simulated hydrogel sphere vs experimental data.	59
3.11. Discretization of the particle-particle linear compression simulation	61
3.12. Fitting of the global vertical force for the case with compression velocity $v = 1 \text{ mm/s}$	62
3.13. Global vertical force measure from the particle-particle linear compression simulation.	63
3.14. Comparison of the global vertical force obtained in the simulation vs experimental data for a particle-particle linear compression test.	64
4.1. Experimental data of the coefficient of restitution of a hydrogel	67
4.2. Simulation setup for calculating the coefficient of restitution of hydrogel spheres.	68
4.3. Velocity output for the freely bouncing hydrogel simulation with higher initial speed	69
4.4. Calculated coefficient of restitution for the freely bouncing hydrogel simulation with higher initial speed	70
4.5. Velocity output for the freely bouncing hydrogel simulation with lower initial speed	70
4.6. Calculated coefficient of restitution for the freely bouncing hydrogel simulation with lower initial speed	71
4.7. Improved fit on the simulated coefficient of restitution at lower initial speed	71
4.8. Analytical fit of the impact velocity of the bouncing hydrogel	73
4.9. Experimental setup of the particle-particle shear test	75
4.10. Simulation setup for the particle-particle shear test	76
4.11. Effect of the velocity on the maximum global vertical force measured . . .	76
4.12. Simulation output of the global vertical force	77
4.13. Simulation output of the global horizontal force	78
4.14. Low pass filtered vs. raw data plot of the global horizontal force on the particle-particle shear test	78
4.15. Averaged vs raw data for a set of particle-particle shear test simulations at different relative positions	79
4.16. Filtered vs raw data of the simulation output with projected normal Hertzian contact forces	80

A.1. Geometrical representation of the FCC lattice cube used for the convergence study and validation of the model.	85
A.2. Stress response detail comparing different DEM particles sizes and their relative accuracy in an FCC	87
A.3. Stress response detail comparing different DEM particle sizes and their relative accuracy in a BCC	87

List of Tables

2.1. Particles size comparison in Simple Cubic lattice	26
2.2. Particles size comparison in Face Centered Cube lattice	27
2.3. Numerical error of elastic Burgers at different normal-to-shear ratios . . .	29
2.4. Calibrated parameters of Burgers model for material 1	33
2.5. Calibrated parameters of the Generalized Maxwell model	36
2.6. Root mean square deviation between analytical fit and experimental data	36
2.7. Calibrated normal-to-shear ratios	36
2.8. Root mean square deviations between simulated and experimental data .	37
3.1. Model parameters used in the oscillatory compression test for the hydrogel sphere	55
3.2. Parameters used in the single particle compression oscillation test. . . .	58
3.3. Parameters used in the particle-particle compression test.	60

List of Acronyms and Symbols

Acronyms

BPM	Bonded Particle Model
CFD	Computational Fluid Dynamics
DEM	Discrete Element Method
FCC	Face Centered Cubic
FEM	Finite Element Method
FFT	Fast Fourier Transform
FVM	Finite Volume Method
RMSD	Root Mean Square Deviation
SC	Simple Cubic
SAOS	Small Amplitude Oscillatory Shear

Latin Letters

A	Oscillation amplitude
A_b	Bond cross-section area [m^2]
c_f	Friction coefficient Hertz model
c_j	Micro-contact viscosity of j^{th} element of Generalized Maxwell model [$\text{N}\cdot\text{m}^{-1}\cdot\text{s}$]
c_k	Micro-contact viscosity of Kelvin element of Burgers model [$\text{N}\cdot\text{m}^{-1}\cdot\text{s}$]
c_m	Micro-contact viscosity of Maxwell element of Burgers model [$\text{N}\cdot\text{m}^{-1}\cdot\text{s}$]
D	Diameter [m]
e	Coefficient of Restitution
E	Young's Modulus [Pa]
E'	Tensile Storage modulus [Pa]

\mathbf{E}''	Tensile Loss modulus [Pa]
\mathbf{f}	Force [N]
f_{cost}	Cost function
\mathbf{G}	Shear Modulus [Pa]
\mathbf{G}'	Shear Storage modulus [Pa]
\mathbf{G}''	Shear Loss modulus [Pa]
\mathbf{J}'	Storage compliance [Pa^{-1}]
\mathbf{J}''	Loss compliance [Pa^{-1}]
\mathbf{k}	Stiffness [Pa]
k_e	Spring stiffness of elastic element of Generalized Maxwell model [Pa]
k_j	Spring stiffness of j^{th} element of Generalized Maxwell model [Pa]
k_k	Spring stiffness of Kelvin element of Burgers model [Pa]
k_m	Spring stiffness of Maxwell element of Burgers model [Pa]
k_n	Normal spring stiffness Hertz model [Pa]
k_t	Shear spring stiffness Hertz model [Pa]
\mathbf{L}	Bond length [m]
\hat{n}	Normal unit vector
r_i	Particle's i radius [m]
r_b	Bond radius [m]
\hat{s}	Shear unit vector
u_m	Kelvin element displacement in Burgers model [m]
u_k	Maxwell element displacement in Burgers model [m]
\mathbf{V}	Volume [m^3]
$\vec{x}_{i,j}$	Particle's i, j position
y_j	Micro-contact stiffness of j^{th} element of Generalized Maxwell model [$\text{N}\cdot\text{m}^{-1}$]
y_k	Micro-contact stiffness of Kelvin element of Burgers model [$\text{N}\cdot\text{m}^{-1}$]
y_m	Micro-contact stiffness of Maxwell element of Burgers model [$\text{N}\cdot\text{m}^{-1}$]
xx	

Greek Letters

α	Normal-to-shear ratio
γ	Shear deformation
δ	Lattice scaling factor
Δt	Simulation timestep [s]
ε	Tensile deformation
θ	Deformation angle [rad]
λ	Radius Multiplier
μ	Viscosity [Pa· s]
μ_j	Viscosity of j^{th} element of Generalized Maxwell model [Pa· s]
μ_k	Viscosity of Kelvin element in Burgers model [Pa· s]
μ_m	Viscosity of Maxwell element in Burgers model [Pa· s]
μ_n	Normal viscosity Hertz model [Pa· s]
μ_t	Shear viscosity Hertz model [Pa· s]
ν	Poisson's ratio
σ	Tensile stress [Pa]
τ	Shear stress [Pa]
τ_m	Maxwell time [s]
τ_k	Kelvin time [s]
φ	Phase lag between stress and deformation in oscillatory test [rad]
χ	Relative error
ω	Oscillation frequency [rad·s ⁻¹]

1. Introduction

1.1. Motivation

Viscoelastic materials are widely used in a variety of processes, and there has been an increasing interest in developing fast and reliable methods to simulate such materials. In this thesis, the focus is on two types of materials. One is a viscoelastic paste used by BOSCH in one of their industrial processes, the other one is a hydrogel sphere used in experiments at Wageningen University and Research.

1.1.1. Viscoelastic paste

Regarding the viscoelastic paste, most of the processes involving this material introduce a complexity in modeling the interface between the material and a solid surface [1]. If an Eulerian method is used to simulate such process, a fine mesh size is needed to capture near-wall flows. Additionally, multi-mode analysis is needed in complex geometries to achieve a reasonable agreement with experimental data [2]. The Finite Element Method has also been used to predict the properties of viscoelastic materials [3, 4], with the limitation of being unable to deal with flowing scenarios. Hence, it is hard for this methods to describe the material's behavior in an industrial application involving strong viscous effects, usually encountered with dynamically moving boundary conditions and extreme situations. At the same time, since Cundall and Strack developed the first Discrete Element Method code [5], a whole new approach was now possible by using particle-based methods. However, most of the work involving numerical modeling and simulations done in literature is material specific [6, 7], i.e. it has been designed and tuned for a particular application and/or material. The idea of this work is the extension of a particle-based method to both homogeneous and inhomogeneous systems. It can predict the rheological properties of a large variety of materials equally, which can then be used to optimize a certain industrial process involving said materials.

1.1.2. Hydrogel sphere

Hydrogels are polymer-based compounds that are highly hydrophilic. When a hydrogel absorbs water, its volume can contain up to 99% water, making it almost identical to it for some physical properties, such as refractive index [8] and density. However, its mechanical properties differ significantly from water, especially its stiffness and flow behavior. A slight change in the composition can lead to vastly different mechanical

properties. Hence, spherical hydrogels have been the focus of research in many other fields, such as biomedical, [9, 10, 11] pharmaceutical [12], agricultural [13], and so on. The most common way to characterize hydrogels is experimental rheology, however, numerical methods have also been used to predict the behavior of hydrogels as a single particle or in a packing [14]. In this thesis, we introduce a new methodology where the single grain is composed of hard spheres that do not account for high deformability themselves. However, given the model's accurate viscoelastic constitutive relation, it can realistically capture high deformability for the single grain. A similar implementation is used in [15], where the single grain deformation is still modeled but with a linear, more complex viscoelastic response. Still, the goal of our work is to be able to capture the real deformation of highly deformable hydrogels and to predict the behavior of single grains and grain-grain contact.

1.2. Viscoelastic materials

Under the name viscoelastic, we address the property of a material behaving both under Hookean law, i.e. (almost) perfectly elastic, or as a viscous fluid, or something in between, depending on the timescale of the external stress/strain at which the material is subjected to. Before diving into the definition of viscoelasticity, it is important to define the limits of the domain in which such materials lie and their story.

Newtonian fluid

In his work, "Philosophiae Naturalis Principia Mathematica" [16], Sir Isaac Newton described the resistance to motion experienced by fluids. His hypothesis defines the behavior of a Newtonian fluid: The resistance encountered when moving a fluid is proportional to the velocity with which the parts of the fluid are separated from one another.

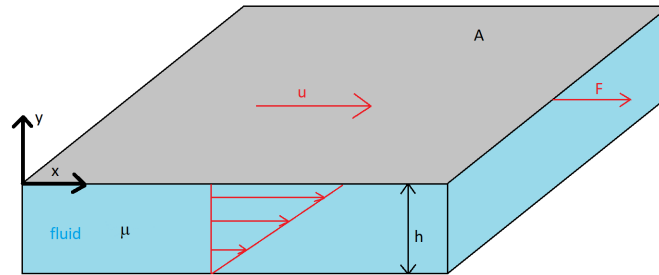


Figure 1.1.: Shear flow of a fluid between two parallel plates in Cartesian coordinates.

Newton attributed this “lack of slipperiness” between two fluid particles to “attritus,” which is Latin for friction. The main conclusion of his work still stands to this day. Keeping in mind the picture of Fig. 1.1, it states that the force F required to maintain the

motion of a fluid between two plates located at an arbitrary distance h , is proportional to the relative velocity between the plates, u , the viscosity μ and inversely proportional to h , giving

$$\frac{F}{A} = \tau_{xy} = \mu \frac{u}{h} = \mu \dot{\gamma}_{xy} \quad (1.1)$$

where τ_{xy} is the stress in the x-direction that lays on the plane perpendicular to the y-axis, while $\dot{\gamma}_{xy}$ is its relative shear rate.

Hookean solid

Robert Hooke was an English engineer, who lived in the same time as Isaac Newton. There was not a good relationship between the two, since Cook claimed that Newton's law of gravitation was based on his work [17]. Regardless of Hooke's popularity in the 17th century, today we remember him for his theory on linear elasticity. In fact, he was the first person to define the relation between force and deformation in a spring [17].

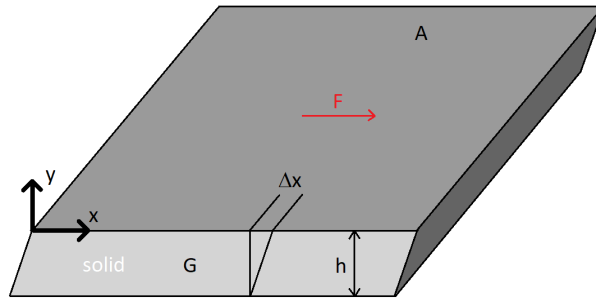


Figure 1.2.: Shear deformation of a solid in Cartesian coordinates.

Looking at Fig. 1.2, the basic theory, summarized in Latin by Hooke's words "*Ut tensio sic vis*" states that the force, F , is directly proportional to the deformation, Δx , giving

$$F = k\Delta x \quad (1.2)$$

where k is the stiffness of the solid. Later in the years, Euler modified Hooke's law by expressing the relation in terms of the stress, resulting in

$$\frac{F}{A} = \tau_{xy} = G \frac{\Delta x}{h} = G \gamma_{xy} \quad (1.3)$$

where G is, in this case, the shear modulus, but in a tensile condition it may be referred to as E , e.g. Young's modulus. From Eqs. 1.2 and 1.3, the relation between the stiffness and the modulus can be found as

$$G = k \frac{h}{A}. \quad (1.4)$$

The universal element used to describe the deformation of a solid is the spring. However, Robert Hooke concluded that elastic behavior is not only observed in springs, *“but in all other springy bodies whatsoever, whether Metal, Wood, Stones, baked Earths, Hair, Horns, Silk, Bones, Sinews, Glass, and the like.”* While this may be valid for metal and stone, all the other materials, some more some less, have a viscous response in addition to the elastic one, rendering them viscoelastic materials [17].

Viscoelasticity

The first to introduce the concept of viscoelasticity was James Clerk Maxwell in 1867 with his paper “On the Dynamical Theory of Gases” [18], maybe unaware he was going to start a new branch of rheology. The majority of viscoelastic materials are, but not limited to, polymers [19], [20], [21], pastes [22], [23], [24], colloidal gels [25], [26], emulsions [27], [28] and the list goes on. The materials can be continuous, like polymers, multiphase systems, like pastes and colloidal gels, or discrete, like in the case of hydrogels [29], [30]. In his model, Maxwell combined the theories of both Newton and Hooke, maybe trying to posthumously put an end to their rivalry, creating a model that uses a spring, to have an instantaneous response to deformation, connected in series with a dashpot, to capture time-dependent changes in deformation rate. With this configuration, the stress is equal on both elements, while the total strain is the sum of the strain on each element:

$$\tau_{xy} = \tau_{xy}^{\mu} = \tau_{xy}^G \quad (1.5)$$

$$\gamma_{xy} = \gamma_{xy}^{\mu} + \gamma_{xy}^G. \quad (1.6)$$

Remembering that the derivative of a sum is the sum of the derivatives, we also have

$$\dot{\gamma}_{xy} = \dot{\gamma}_{xy}^{\mu} + \dot{\gamma}_{xy}^G. \quad (1.7)$$

Combining Eqs. 1.5-1.7, and remembering that $\tau_{xy} = G\gamma_{xy}^G = \mu\dot{\gamma}_{xy}^{\mu}$ we obtain a differential equation relating the stress and the strain in the Maxwell element as

$$\dot{\gamma}_{xy} = \frac{\tau_{xy}}{\mu} + \frac{\dot{\tau}_{xy}}{G} \quad (1.8)$$

This relation is very helpful when we want to predict the stress response of a viscoelastic material under a certain stress or vice-versa, and it will be used extensively in this thesis. The relation between stress and strain of a material is the subject of study of rheology, which started as a branch of mechanics to describe the behavior of solids and fluids but has now expanded to viscoelasticity as well.

Rheology

The common ground when talking about viscoelasticity is rheology. Without a rheological study of the material, performing any simulation or designing any process would be impossible, so extracting high-quality data when setting up a rheological experiment is

extremely important. One of the most common experiments done on viscoelastic materials is the so-called oscillatory shear rheometer [31],[32]. This experiment is performed by placing a material of which the rheological properties must be defined between parallel plates, as in Fig. 2.18. Usually, to ensure no-slip conditions at the boundary between plates and material, glues are used. The bottom plate is fixed, while the top plate oscillates around its center axis with a given amplitude and frequency. What is measured is the torque on the top plate to ensure a certain amplitude and frequency, which is then converted into shear stress. If a Hookean solid, i.e. a perfectly elastic material, is placed in the rheometer, the strain input and the stress response are as follows:

$$\begin{aligned}\gamma(t) &= \gamma_0 \sin(\omega t) \\ \tau(t) &= \tau_0 \sin(\omega t)\end{aligned}\tag{1.9}$$

which means that the strain and the stress are in phase with each other [17]. When computing the elastic modulus, which we will call G when dealing with shear modulus and E when is tensile, the following is obtained

$$G = \frac{\tau_0 \sin(\omega t)}{\gamma_0 \sin(\omega t)} = \frac{\tau_0}{\gamma_0}.\tag{1.10}$$

The opposite behavior of a perfectly elastic solid is an ideal viscous fluid, where the stress is proportional to the strain rate rather than the strain, giving

$$\begin{aligned}\gamma(t) &= \gamma_0 \sin(\omega t) \\ \dot{\gamma}(t) &= \gamma_0 \omega \cos(\omega t) \\ \tau(t) &= \tau_0 \cos(\omega t) = \tau_0 \sin(\pi/2 - \omega t).\end{aligned}\tag{1.11}$$

This means that the strain and the stress are out of phase of exactly $\pi/2$ radians. Here, instead of an elastic modulus, we compute the viscosity as

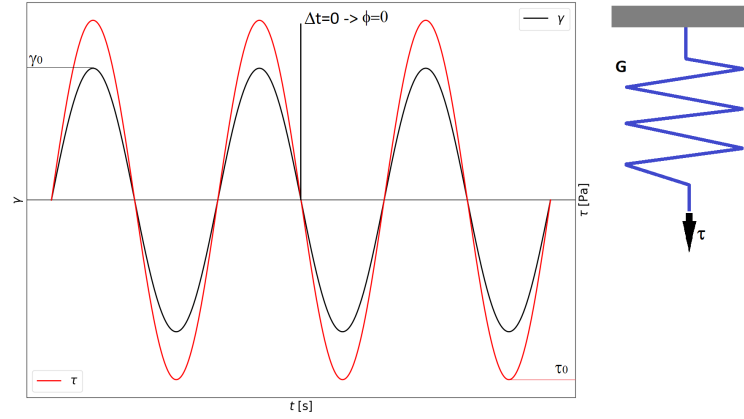
$$\mu = \frac{\tau_0 \cos(\omega t)}{\gamma_0 \omega \cos(\omega t)} = \frac{\tau_0}{\gamma_0 \omega}\tag{1.12}$$

which corresponds to the definition of a Newtonian fluid.

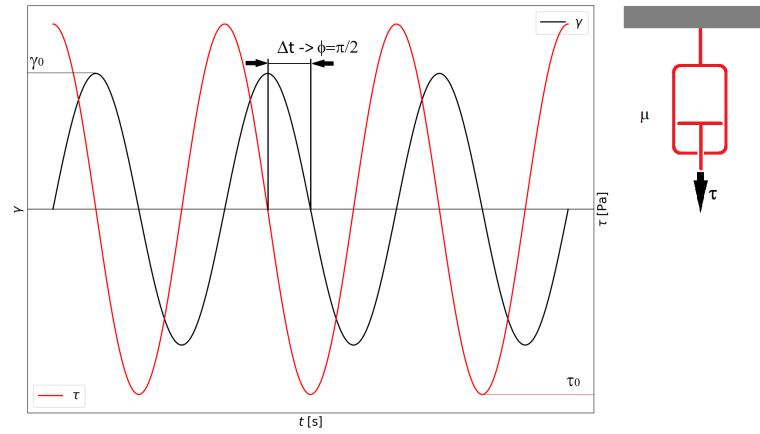
On the other hand, viscoelastic materials behave in a manner that is in between the perfect elastic and the ideal viscous fluid, depending on the time scale of the applied stress or strain. The typical response of a viscoelastic material is defined as

$$\begin{aligned}\gamma(t) &= \gamma_0 \sin(\omega t) \\ \tau(t) &= \tau_0 \sin(\omega t - \varphi),\end{aligned}\tag{1.13}$$

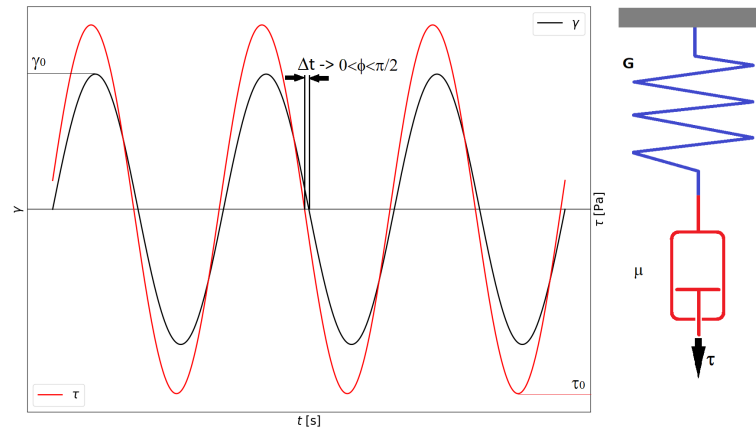
where $0 < \varphi < \pi/2$ is the phase lag between the strain input and the stress response. A nice graphical summary can be observed in Fig. 1.3



(a) Strain input and stress response of a Hookean solid and graphical representation. To be noted how stress and strain are both in phase with each other



(b) Strain input and stress response of an ideal Newtonian fluid. Here the stress lags $\pi/2$ behind the strain.



(c) Strain input and stress response of a generic viscoelastic material. The phase lag of the stress with respect to the strain is in between the Hookean solid and the ideal viscous fluid.

Figure 1.3.: Graphical representation and stress response of the typical rheological oscillatory shear test of a) Hookean solid, b) ideal fluid, and c) viscoelastic material.

1.3. Numerical models

In this thesis, we focus on predicting the rheological and mechanical properties of different viscoelastic materials using a numerical model based on the Discrete Element Method (DEM). Before diving into the specifics of DEM, we will show a brief summary of the alternative methods used so far in the characterization of viscoelastic flows.

Computational Fluid Dynamics

Solving the full set of the Navier-Stokes equations for a generic compressible unsteady flow can prove to be very hard for a complex system, if not almost impossible without the proper simplifications. With the advent of computers, scientists started implementing numerical models to characterize viscous flows in complex geometries by using the so-called Computational Fluid Dynamics (CFD).

One of the earliest, probably the first, use of computers to solve fluid flows was done by the Los Alamos National Lab led by Francis H. Harlow in 1955. He is considered one of the fathers of CFD, with focus on 2D flows. To have the first paper on a 3D CFD study we have to wait until 1967 [33].

The main idea behind a CFD code is to divide the fluid domain into finite volumes and solve, for each volume, the conservation equations for mass, momentum, and energy. The main problem is that computers cannot exactly integrate partial differential equations, but they solve a discretized version of the continuous Navier-Stokes equations, shown in Eqs. 1.14 - 1.16.

$$\frac{\partial \rho}{\partial t} + \frac{\partial}{\partial x_i} (\rho u_i) = 0 \quad (1.14)$$

$$\frac{\partial (\rho u_i)}{\partial t} + \frac{\partial}{\partial x_j} (\rho u_i u_j) - \frac{\partial \sigma_{ij}}{\partial x_j} - \rho g_i = 0 \quad (1.15)$$

$$\frac{\partial (\rho E)}{\partial t} + \frac{\partial}{\partial x_j} (\rho E u_j - \sigma_{ij} u_i + q_j) = \rho g_i u_i \quad (1.16)$$

Taking into account the moment conservation of Eq. 1.15, we can further look into the stress tensor σ_{ij} , which, for a Newtonian fluid, is defined as

$$\sigma_{ij} = -p\delta_{ij} + \tau_{ij} = -p\delta_{ij} + \mu \left(\frac{\partial u_i}{\partial x_j} + \frac{\partial u_j}{\partial x_i} \right) + \delta_{ij} \lambda \frac{\partial u_k}{\partial x_k}. \quad (1.17)$$

In Eq. 1.17, the stress tensor is composed of the sum of the mechanical pressure p and the deviatoric stress tensor τ_{ij} , which is responsible for the viscous forces. It comprises two parts; both are proportional to the strain rate, but the first part has a proportionality constant μ , which we already encountered in the previous sections, and is responsible for the deviatoric strain rate. The second part is proportional to λ , called volume viscosity, and is responsible for the viscous forces related to bulk viscosity.

As described in the previous sections, to be able to describe viscoelastic flows, we need

to introduce an elastic component in the stress tensor, such that we can also capture instantaneous responses to external deformations. The first to introduce such a concept was Giesekus [34]. He modified the stress tensor formulation to introduce different terms that accounted for different timescales. After Giesekus published his work, CFD solvers have been developed to capture the flow properties of viscoelastic materials [35], [36], [37]. The method used when solving viscoelastic flows with CFD is called Finite Volume Method (FVM). In this method, the domain is divided into smaller volumes. At the same time, the partial differential equations governing the conservation laws of the flow are discretized in their algebraic form, using volume averages [38] and solving for the fluxes of the conserved variable through the surfaces of the volume. The discretization into smaller volumes, called meshing, can become very non-trivial when dealing with complex geometries and moving boundaries. It still remains a powerful ally to engineers and physicists, but when dealing with viscoelastic materials, sometimes something simpler might be the answer.

Finite Element Methods

The close cousin of CFD and FVM is the Finite Element Method (FEM). The principle is the same, i.e., dividing the domain into finite bodies. But, while the FVM solves for fluxes, the FEM uses basis functions to approximate the integral form of the conservation laws along the elements. These elements are connected by nodes, where the dependent variables are stored. It is important to choose the correct basis function so that each node displacement is followed by a physical stress of the element. It is clear how a FVM is more prone to better capture flows and larger deformations that are usually a challenge for FEM. Given the large range of properties for viscoelastic materials, some FEM-based models have been developed to predict the viscoelastic response of more solid-like materials [3], or creep behavior in polymers [4], as well as adhesive materials [39].

If, on the one hand, CFD is more efficient for polymer flows where the viscous response is more dominant and FEM is more suited for materials with a stronger elastic response, in this work, we want to present an alternative to both of these methods by using DEM.

Discrete Element Method

DEM is relatively new when compared to other Numerical Methods, but it increased our knowledge of granular materials of several orders of magnitude in recent years. Since Cundall and Strack [40] published their paper, a great variety of models has been developed to adapt the DEM to different materials and applications. There exist, for example, models that account for cohesive powders [41, 42], irregular particle shapes [43], soft grains [44], and so on.

The main idea behind a DEM model is that of representing a real assembly of granular materials by simulating each grain as an isolated undeformable element. Each time there is a contact between two elements, forces, and torques are computed from the models listed previously, which usually depend on the relative motion between the elements, as

shown in Fig. 1.4, which defines a simple Hertz model between two spheres. It can be observed that this model could already describe viscoelastic assemblies as it contains a Maxwell element. However, since the force is computed only when two particles collide, it is limited to granular assemblies. Moreover, it can only capture one timescale since there is only one spring and one dashpot, hence it lacks generalization, as it will be better explained later.

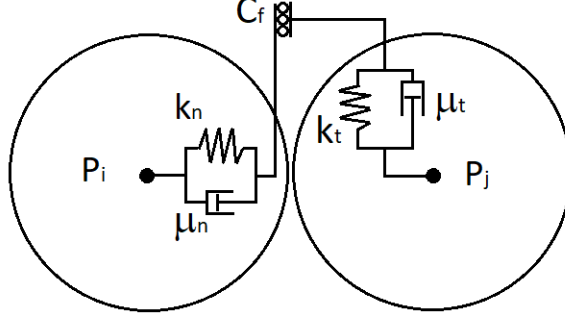


Figure 1.4.: Schematic of the Hertz model in classical DEM between two DEM spheres. The main parameters are divided into normal components k_n , μ_n , and tangential components k_t , μ_t . Additionally, a friction coefficient is responsible for energy loss due to relative tangential velocity. This is the simplest viscoelastic contact existing in DEM, but it doesn't apply to cohesive systems as it produces mostly repulsive forces.

The limitation of the classical DEM models is that they can only deal with granular assemblies. It is difficult to simulate materials that appear continuous on a large scale and can show more viscous effects. To overcome this, DEM needs to be combined with CFD or FEM to be able to characterize systems where a continuous domain is present [45]. Another way of improving classical DEM is to implement new contact models that can simulate the aggregation of the elements using numerical features.

In this work, the contact model used as a starting base is the Bonded Particle Model (BPM), introduced by Potyondy and Cundall [5]. In their original formulation, Potyondy and Cundall [5] laid the foundations of the Bonded Particle Model, by proposing a list of features that uniquely characterize the model. This list defines the way the particles interact and separate the different types of contacts that can form during the simulation. Before going through the list is important to define the main steps in the formulation.

1. **Bond initialization:** The elements are generated in the simulation domain with a certain initial position and velocity. This phase is crucial as it will determine which particles are bonded and which are not. To better understand, we can take a look at Fig. 2.1. Here two particles are bonded together even though they are

not overlapping. This is obtained by multiplying each particle's radius by a factor called the radius multiplier, indicated with λ . Moreover, a certain timestep is chosen as the bond creation timestep. When this timestep occurs, the condition for the bond creation that is checked is whether the distance between two particles is less or equal to the sum of the increased radii, i.e., $|\vec{x}_j - \vec{x}_i| \leq \lambda(r_i + r_j)$. If this condition is met, then a bond is formed, and the forces are initialized at zero. This means that the relative position at which the particles are found when the bond is formed is taken as the equilibrium position. Moreover, the bond is defined as a cylindrical beam of length $L = |\vec{x}_j - \vec{x}_i|$ and radius $r_b = \min(r_i, r_j)$.

2. **Bonded contact vs non-bonded contact:** If two particles are bonded together, each relative motion will generate a force that is computed according to the constitutive relation used. If two bonded particles overlap each other, no additional force is computed, although the amount of overlap is limited by the materials' stiffness. In other words, when a certain material is calibrated, the parameters of the constitutive relation of the bond force will act as a limiting factor to non-physical compression. However, when two elements are not connected by a bond, the Hertz contact force is computed normally as it would be done in classical DEM.
3. **Bond breakage:** Potyondy and Cundall added a bond failure to their formulation by setting a limit stress in both normal and shear direction, hence adding two more parameters to the model. The condition for bond failure is that either one between the n^{th} timestep normal stress $\sigma^n = \frac{f_{norm}^n}{A_b}$ or the n^{th} timestep shear stress $\tau^n = \frac{f_{sh}^n}{A_b}$, with $A_b = \pi r_b^2 * L$, are greater than critical values σ_{crit} or τ_{crit} respectively. To calibrate these critical stress values, additional experiments need to be performed to assess the fracture conditions of the material. However, since in this thesis we only deal with highly deformable grains and pastes, we preferred to have a simpler condition for bond breakage based solely on the maximum distance the bonded particles can go before the bond is broken and kept constant for all the simulations. In other words, we are not interested in fracture behavior, but we focus on the rheological response and mechanical properties under small strains.

In fact, the BPM has been used for such materials, ranging from rocks [46], to sea ice [47], cemented sand [48], and so on. The goal of this work is to create a new DEM-based model that can characterize both single grains and continuous systems where a viscoelastic stress component is observed, such that the final users won't have to scratch their heads jumping from a mesh-based to a mesh-less method. Still, they will be able to predict the behavior of their materials using the one tool to rule them all, i.e. the hereby proposed model. To achieve this, the BPM is modified to have a complex viscoelastic response to deformation, as opposed to the single Maxwell element of the original formulation.

1.4. Goals and Contents

The aim of this thesis is to introduce a new DEM-based model as a tool for studying ensembles of viscoelastic materials. The main goals of this work are:

1. Implement a Viscoelastic Bonded Particle Model into the open-source LIGGGHTS DEM solver.
2. Validate the convergence and stability of the model using small-scale tests.
3. Using experimental data as a benchmark, perform a calibration routine to obtain the optimal model parameters for a specific material.
4. Test the validity of the calibration process by comparing experimental and simulation data of a large-scale test.
5. Extend the model's applicability to different materials and systems, showing its flexibility to adapt to completely different scenarios.

We obtained these goals in the thesis as follows:

- In Chapter 2 we show the two viscoelastic models, namely the Burgers and the Generalized Maxwell, with their relative discretization and implementation in the code. Additionally, we show the calibration routine for both the models, with their limitations and applicability. Moreover, the validation of the models is carried out using a small scale simulation as well as a larger scale simulation, both finding good agreement with the experimental data.
- In Chapter 3 we show the application of the Generalized Maxwell model to a highly deformable viscoelastic Hydrogel sphere. We show the experiments performed, the calibration routine to obtain the optimal parameters and the validation of the model on a particle-particle contact, finding again a good agreement between the simulated data and the real worlds quantities.
- In Chapter 4 we carried out additional work on Hydrogel sphere, showing how the model is able to capture other mechanical properties just by calibrating the viscoelastic parameters. Additionally, the limitations of the model are highlighted and the initial attempts at solving these limitations are shown, as well as providing an outlook for future work.

Additionally, the model as implemented in Aspherix API as well as in LIGGGHTS is available at a public repository, whose link can be found in Appendix B. Together with the model implementation, the link to a public repository containing the codes developed to perform the main post-processing and calibration routines can be found in Appendix B.

1.5. Contributions to publications

Chapter 2 and chapter 3 are based on scientific publications. This section summarizes the author's contributions.

1.5.1. Publication on the viscoelastic paste calibration and validation

Mascara, M., Mayrhofer, A., Radl, S. and Kloss, C., 2024. Implementation and validation of a bonded particle model to predict rheological properties of viscoelastic materials. *Particuology*, 89, pp.198-210.

Mascara, M.: Conceptualization, Methodology, Software, Validation, Visualization, Writing - Original Draft.

1.5.2. Publication on the hydrogel experimental calibration and validation

Mascara, M., Shakya, C., Radl, S., Mayrhofer, A. and Kloss, C., 2024. A viscoelastic bonded particle model to predict rheology and mechanical properties of hydrogel spheres. *Granul. Matter*, 26, 64 (2024).

Mascara, M.: Conceptualization, Methodology, Software, Validation, Visualization, Writing - Original Draft.

2. Implementation and validation of a Bonded Particle Model to predict the Rheology of viscoelastic materials

2.1. Introduction

One of the first attempts at describing viscoelasticity was done by Giesekus [34]. In his mostly analytical work, he modified the stress tensor definition in the momentum equation of a fluid by considering additional linear and non-linear stress-strain constitutive relations, with tensors and parameters describing the network of a given material. Given the complexity of his formulation, an analytical solution was obtained for simple flows. With the advent of numerical methods, it has been possible to push the frontier of solving complex flows involving viscoelastic materials. Still, it simultaneously introduces all the challenges these methods may add. One degree of complexity is modeling the interface between the material and a solid surface [37], where a fine mesh size is needed to capture near-wall flows. Additionally, multi-mode analysis is needed in complex geometries to achieve a reasonable agreement with experimental data [2]. The Finite Element Method has also been used to predict the properties of viscoelastic materials [3, 4], with the limitation of being unable to deal with flowing scenarios. Hence, it is hard for this method to describe the material's behavior in an industrial application involving strong viscous effects, usually encountered with dynamically moving boundary conditions and extreme situations. At the same time, since Cundall and Strack developed the first Discrete Element Method code [40], a whole new approach was now possible, where the absence of a volumetric mesh would greatly simplify the simulations.

On the one hand, mesh-based methods are handy when describing single-phase materials. On the other hand, particle-based methods can describe heterogeneous systems with the presence of polydisperse phases [49], multi-phase conglomerates, such as oil sand [50], coke-pitch mixtures [51], and asphalt [52], to cite some. Most of the work involving numerical modeling and simulations done in literature is material specific [6, 7], i.e. it has been designed and tuned for a particular application and/or material. The idea of this work is the extension of a particle-based method to both homogeneous and inhomogeneous systems. It can predict the rheological properties of a large variety of materials equally, which can then be used to optimize a certain industrial process involving said materials. A particle-based method is described, tested, and validated against experimental data to achieve this. It is based on the Bonded Particle Model (BPM), first introduced by Potyondy and Cundall[5] where particles would interact with each other at contact through an elastic beam, to describe the amorphous properties of rocks,

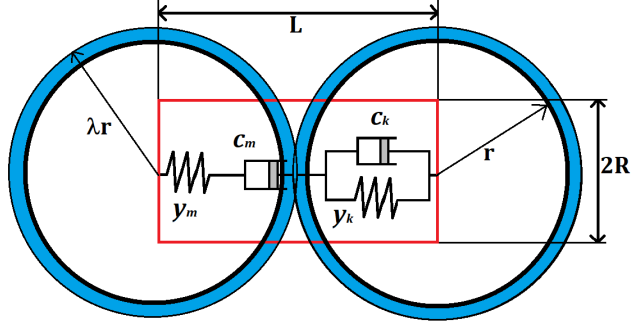


Figure 2.1.: Schematic of the Bonded Particle Model with Burgers representation for the normal direction. An equivalent representation is used for the shear direction (visualization omitted for simplicity).

defined as a heterogeneous system of irregularly shaped or spherical particles. The idea is to extend this model to viscoelastic materials by substituting the purely elastic relations used in the original BPM definition with a viscoelastic interaction. In this case, the Burgers model is initially implemented in the commercial software Aspherix[®], showing the discretization scheme for the constitutive relation. Moreover, a test calibration is performed using an existing dataset, which shows that another method is needed to improve accuracy, namely the Generalized Maxwell model.

The idea behind the realization of this paper is the creation of a unique particle-based method capable of predicting the flow of fluids and granular media whose rheological properties are known. This would then serve as an initial step to calibrating this model and tuning it so it can be used in various industrial processes dealing with viscoelastic materials without using complex mesh-based methods.

2.2. Methodology

Introducing a bond between particles opens a new door to the modeling of cohesive powders and suspensions with cohesive particles, e.g., cement. Unlike cohesive models, the BPM is not bound to purely granular materials. Still, it can be extended to various systems, where, even though two or more phases can be distinguished at a microscopic level, they are macroscopically homogeneous. Moreover, the particles do not need to be in contact to exchange forces. To achieve this, the particles radii are multiplied by a constant parameter, called the radius multiplier λ , producing an increased fictitious particles size that does not influence its volume nor its mass, but it is used merely to create a contact between particles that are not necessarily physically touching. Starting, for simplicity, with two particles with equal radii $r_i = r_j = r$, positions \vec{x}_i, \vec{x}_j , as shown in Fig. 2.1, a bond is formed when there exists an overlap between the increased particles size, i.e. the distance d between the particles is less or equal than the sum of the increased radii, or $d = |\vec{x}_i - \vec{x}_j| \leq 2\lambda r$. In general, the length and radius of the bond are defined at its creation to be, respectively, $L = d$ and $R_b = \lambda \min(r_i, r_j)$ in the case of particles

with different sizes. The value of the radius multiplier needs to be chosen according to the initial distance between particles that need to be bonded, in such a way to ensure the bond formation. For example, if two particles are distant 2 mm and their radii are 0.4 mm. Since these particles are not touching ($r_i + r_j = 0.8 \text{ mm} < 2 \text{ mm}$) if one would like for these particles to be bonded, a value of $\lambda > 1.25$ is needed to ensure overlap.

2.2.1. Modified BPM with Burgers relation

As mentioned, the purely elastic constitutive relation used in the original BPM formulation [5] is here substituted with a viscoelastic relation. Even though the original formulation of the BPM could handle viscoelasticity, since it also has a damping element in its implementation, some drawbacks must be addressed. To begin with, the original BPM implementation can be described as a Kelvin-Voigt solid, the simplest viscoelastic model, consisting of a spring and a dashpot connected in parallel. Given the target of the model described in this paper to be able to predict the behavior of a large range of materials, the Kelvin-Voigt model does not have enough timescales that would give generality to the original BPM. Moreover, calibration would be tricky because, to connect experimentally obtained rheological macro-properties with the model parameters, the analytical model response to the oscillatory shear test is needed, as it will be explained in more detail later. For this reason, it has been decided to start with at least two timescales, using a model already established as robust for a class of materials, namely the Burgers model, whose configuration is shown in Fig. 2.1. It is a combination of a Maxwell element, composed of a spring and a dashpot in series, connected in series with a Kelvin-Voigt element. The constitutive relation of Burgers materials has the following equation

$$\tau_k \tau_m \frac{d^2 \sigma}{dt^2} + \left[\tau_k + \tau_m + \frac{\mu_k}{k_m} \right] \frac{d\sigma}{dt} + \sigma = \tau_k \mu_m \frac{d^2 \varepsilon}{dt^2} + \mu_m \frac{d\varepsilon}{dt}, \quad (2.1)$$

where $\tau_m = \mu_m/k_m$ and $\tau_k = \mu_k/k_k$ are the Kelvin and Maxwell time, respectively, computed from the spring constant k and the dashpot constant μ . Furthermore, σ is the stress acting on the element, and ε is the strain. Eq. (2.1) can be converted in its respective force-displacement formulation, as it is easier to handle for the implementation in the DEM code, resulting in

$$\tau_k \tau_m \frac{d^2 f}{dt^2} + \left[\tau_k + \tau_m + \frac{c_k}{y_m} \right] \frac{df}{dt} + f = \tau_k c_m \frac{d^2 u}{dt^2} + c_m \frac{du}{dt}. \quad (2.2)$$

Where $f = \sigma/A_b$ is the force acting on the element, the Bond cross-section area [m^2] (A_b) is defined as $A_b = \pi R^2$, which is constant during contact, u is the displacement of the element, and Micro-contact viscosity of Maxwell element of Burgers model [$\text{N} \cdot \text{m}^{-1} \cdot \text{s}$] (c_m), Micro-contact viscosity of Kelvin element of Burgers model [$\text{N} \cdot \text{m}^{-1} \cdot \text{s}$] (c_k), Micro-contact stiffness of Maxwell element of Burgers model [$\text{N} \cdot \text{m}^{-1}$] (y_m) and Micro-contact stiffness of Kelvin element of Burgers model [$\text{N} \cdot \text{m}^{-1}$] (y_k) are the micro-contact parameters, which are computed from the macro-parameters as [5]:

$$c_m = \frac{A_b}{L}\mu_m, c_k = \frac{A_b}{L}\mu_k, y_m = \frac{A_b}{L}k_m, y_k = \frac{A_b}{L}k_k, \quad (2.3)$$

where L is the bond length defined at the section's beginning.

Discretization of the Burgers equation

Given certain initial conditions, the simulation can be carried out if we can close the simulation loop, making it possible to solve the system dynamics. To achieve this, we need to compute first the forces acting on the particles through the constitutive relation, then use the newly computed forces to integrate the equation of motion of each particle. To begin with, the viscoelastic constitutive relation is discretized numerically, which computes the forces acting between bonded particles as a function of the relative motion. The initial distribution of the particles acts as a boundary condition. In contrast, at the first timestep, initial conditions dictate the motion of all or some of the particles in the system. The displacement and displacement rate in the relative motion between particles are the independent variables in the discretized constitutive relations, which calculate the new forces. Ultimately, the new forces are used to numerically integrate the equation of motion to obtain new displacements, closing the computational loop. For the interested reader, please refer to the code for the calculation of Hertzian and bond forces in the Appendix to have more insights on the working principles of the numerical scheme.

The following discretization is currently used in the commercial software Aspherix and PFC3D, described in Ref. [53]. Starting from the Kelvin element and remembering that for elements in parallel, stresses are cumulative while displacements are equal, the following constitutive relation is found

$$f = y_k u_k + c_k \frac{du_k}{dt}, \quad (2.4)$$

which can be rewritten as a function of the displacement rate $\frac{du_k}{dt}$ of the Kelvin element and computed at timestep $n + \frac{1}{2}$, (please note that the superscripts in the following equations refer to the timestep at which the variables are computed and they are not exponents) leading to

$$\left. \frac{du_k}{dt} \right|_{n+\frac{1}{2}} = \frac{f^{\{n+\frac{1}{2}\}} - y_k u_k^{\{n+\frac{1}{2}\}}}{c_k}. \quad (2.5)$$

Applying a Taylor series expansion to the Kelvin element displacement, centered in $t = \Delta t(n + \frac{1}{2})$, with step width $\frac{\Delta t}{2}$, the following approximation for the first derivative is obtained

$$\left. \frac{du_k}{dt} \right|_{n+\frac{1}{2}} = \frac{u_k^{\{n+1\}} - u_k^{\{n\}}}{\Delta t} + \mathcal{O}(\Delta t^2). \quad (2.6)$$

Substituting Eq. (2.6) into Eq. (2.5), taking average values for the other variables and re-arranging the terms to obtain an equation as a function of the new timestep displacement, leads to the following

$$u_k^{\{n+1\}} = \frac{1}{2\tau_k + \Delta t} \left[\frac{\Delta t}{y_k} (f^{\{n+1\}} + f^{\{n\}}) + u_k^{\{n\}} (2\tau_k - \Delta t) \right]. \quad (2.7)$$

For the Maxwell element, the constitutive relation is obtained by considering that the stress/force seen by each element in series is equal while the deformation/displacement is different, giving

$$\frac{du_m}{dt} = \frac{1}{y_m} \frac{df}{dt} + \frac{f}{c_m}. \quad (2.8)$$

Similarly, as it has been done for the Kelvin element, the same discretization scheme can be applied to the displacement rate of the Maxwell element, with the difference that now the derivative of the force appears. Once the scheme is applied, it is possible to re-arrange the terms to obtain

$$u_m^{\{n+1\}} = \frac{f^{\{n+1\}} - f^{\{n\}}}{y_m} + \Delta t \frac{f^{\{n+1\}} + f^{\{n\}}}{2c_m} + u_m^{\{n\}}. \quad (2.9)$$

Finally, knowing that $u = u_k + u_m$, deriving it once with respect to time and applying a central difference scheme as done in Eq. (2.6), the new timestep force value can be computed from the old timestep forces and displacements as

$$f^{\{n+1\}} = \frac{u^{\{n+1\}} - u^{\{n\}} + \frac{2\Delta t}{2\tau_k + \Delta t} u_k^{\{n\}} - A f^{\{n\}}}{B}, \quad (2.10)$$

where $A = \frac{\Delta t}{2c_k + \Delta t} + \frac{1}{y_m} + \frac{\Delta t}{2c_m}$ and $B = \frac{\Delta t}{2c_k + \Delta t} - \frac{1}{y_m} + \frac{\Delta t}{2c_m}$.

Furthermore, the displacements in normal and shear directions are defined from the relative motion between the particles, which is solved at each timestep by numerically integrating Newton's second law. Eq. (2.10) is scalar, but the old force and kelvin displacement values for each direction are stored as vectors. To be able to substitute them in the discretization, a semi-projection is first carried out (it is shown for the normal direction, but exactly the same procedure stands for the shear direction)

$$\begin{aligned} f_{norm}^{\{n\}} &= \vec{f}_{norm}^{\{n\}} \cdot \hat{n}^{\{n+1\}} \\ u_{k,norm}^{\{n\}} &= \vec{u}_{k,norm}^{\{n\}} \cdot \hat{n}^{\{n+1\}}, \end{aligned}$$

where $\hat{n}^{\{n+1\}}$ is the unit vector in the relative normal direction between the particles in contact. Once the new timestep force, as well as the kelvin displacement, are computed, they are projected onto the new normal direction

$$\begin{aligned}\vec{f}_{norm}^{\{n+1\}} &= f_{norm}^{\{n+1\}} \cdot \hat{n}^{\{n+1\}} \\ \vec{u}_{k,norm}^{\{n+1\}} &= u_{k,norm}^{\{n+1\}} \cdot \hat{n}^{\{n+1\}}.\end{aligned}$$

2.2.2. The generalized Maxwell model

Together with the Burgers model, in this work, a Generalized Maxwell Model has been implemented due to the low accuracy of the former, which will be discussed later in this paper. As the name suggests, the Generalized Maxwell model is defined as a connection in parallel of a certain number of Maxwell elements, plus a spring and/or a dashpot, as depicted in Fig. 2.2. Even though it appears more complex than a Burgers model, its implementation is rather simple for two reasons. To begin with, the constitutive relation of Eq. (2.8) only contains the first derivatives in time, making it easier to discretize. Moreover, all elements undergo the same deformation, simplifying the implementation. In the current work, a 4 element model is used, plus a spring. The choice of 4 elements comes from the fact that, when trying to fit experimental data on a large dataset, it has been observed that 3 elements still lack accuracy, while 4 elements show a nice fit quality through the whole dataset, Figs. 2.15 and 2.16. A similar implementation has been used by Ren et al. [54], without bonds and in combination with different phases behaving elastically or viscoelastically depending on the nature of the contact. They obtained a relatively good agreement with experimental data. After scaling the macro-parameters into their respective micro-contact values as $y_j = k_j A_b / L$ and $c_j = \mu_j A_b / L$, the new timestep force relative to the single Maxwell element is computed from re-arranging Eq. (2.9) to give

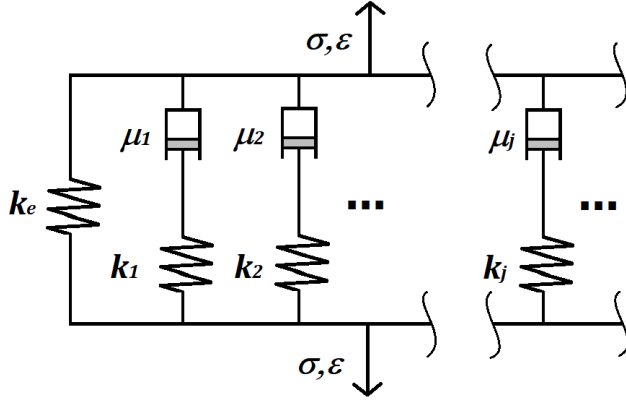


Figure 2.2.: Schematics of the Generalized Maxwell Model

$$f_j^{\{n+1\}} = \frac{u^{\{n+1\}} - u^{\{n\}} + f_j^{\{n\}} \left(\frac{1}{y_j} - \frac{\Delta t}{2c_j} \right)}{\frac{1}{y_j} + \frac{\Delta t}{2c_j}}, \quad (2.11)$$

where the subscript j expresses the j^{th} element in the model. Regarding the spring force f_{el} , a finite deformation approach is used, given that the relative positions at the bond creation are known. Hence, it is straightforward to compute the displacement relative to the bond creation timestep n_0 , leading to $f_{el}^{\{n+1\}} = y_e(u^{\{n+1\}} - u^{\{n_0\}})$, with $y_e = k_e/A_b$, where k_e is the spring coefficient. The same applies to the shear direction as done in Sec. 2.2.2. Finally, the total force is assumed to be just a sum of the single elements contribution, $f^{\{n+1\}} = \sum_j^4 f_j^{\{n+1\}} + f_{el}^{\{n+1\}}$.

Contact plane and displacements definition

In Eq. (2.10), the new timestep force is a function of the displacement $\Delta\vec{u}$, which is defined as the difference in relative distance between the particles at consecutive timesteps, $\Delta u = u^{\{n+1\}} - u^{\{n\}}$. After solving the particle's equation of motion, all the information on its position, velocity, and angular velocity are known at the timestep $n + 1$, while quantities at timestep n are saved. Let two particles i and j be in contact. Their relative displacement between two consecutive timesteps is $\Delta\vec{u} = \vec{r}^{\{n+1\}} - \vec{r}^{\{n\}}$, with $\vec{r} = \vec{x}_i - \vec{x}_j$ the relative position between the particles. While the definition of the unit normal vector is rather simple, being just the normalized \vec{r} , for the shear direction many different ways are possible, being there infinite orthogonal lines with respect to \hat{n} . The method adopted here is that of defining a contact plane between the timestep at which the bond is formed, called n_0 , and the actual timestep and considering as shear direction the unit vector orthogonal to \hat{n} which lays on said plane [55]. As a result, the unit shear vector is defined as

$$\hat{s}^{\{n+1\}} = \frac{\hat{n}^{\{n+1\}} \times (\hat{n}^{\{n+1\}} \times \hat{n}^{\{n_0\}})}{|\hat{n}^{\{n+1\}} \times (\hat{n}^{\{n+1\}} \times \hat{n}^{\{n_0\}})|}. \quad (2.12)$$

Once the principal directions at the new timestep contact are known, the semi-projected displacements in normal and shear directions are then computed similarly as done for the force and the kelvin displacement, giving

$$\begin{aligned} \Delta u_{norm} &= \Delta\vec{u} \cdot \hat{n}^{\{n+1\}} \\ \Delta u_{shear} &= \Delta\vec{u} \cdot \hat{s}^{\{n+1\}}. \end{aligned}$$

2.2.3. Simulation test case

The most common experimental setup to compute the rheological properties of viscoelastic materials is the oscillatory shear rheometer. To mimic such experiments, in this study, an ordered lattice of particles is created, both in a simple cubic and in more complex geometries, highlighting the differences. A lattice scaling is defined by a value $\delta = D(1 + \eta)$, where D is the diameter of the particles and η is a small and positive arbitrary number, which means all the particles are not overlapping. However, η is chosen according to the radius multiplier λ value so that bonds will form between neighboring

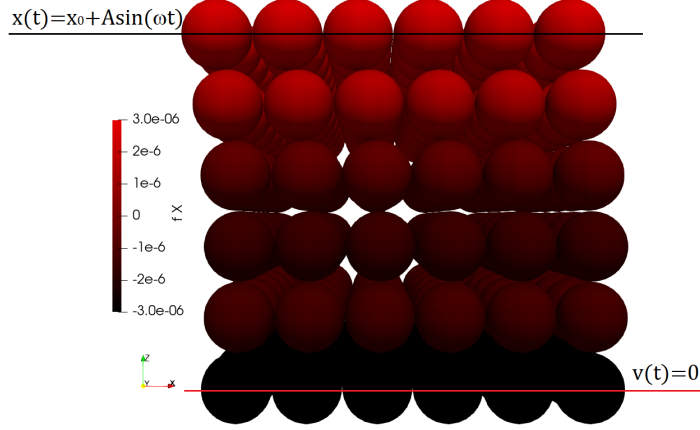


Figure 2.3.: Lattice geometry and boundary conditions. The top layer of particles is displaced with a periodic motion, governed by an amplitude of $A = 0.01(D + 5\delta)$ m and a frequency $\omega = 600$ rad/s, while the bottom layer is fixed. The coloring shows the x-component of the force on each particle expressed in Newton.

particles. The faces of the cube are normal to the orthogonal global system of coordinates, and the boundary conditions are applied to the external layer of particles normal to the z-direction, as depicted in Fig. 2.3. The periodic motion applied to the upper layer of particles is maintained in the Small Amplitude Oscillatory Shear (SAOS) regime to ensure linearity, with a strain equal to 1% [56].

First, the stress response is computed as the sum of the forces f_i acting on the top layer of particles in the z-direction to measure the rheological properties, divided by the surface area defined by the aforementioned particles. Taking as an example the configuration of Fig. 2.3, the stress is computed as

$$\tau = \frac{\sum_i^{N^2} f_i}{(D + (N_{side} - 1) \cdot \delta)^2}, \quad (2.13)$$

where $N_{side} = 6$ in this case.

It has been observed that for certain combinations of parameters and frequency applied, the eigenfrequency of the system would interfere with the stress signal, altering the output and eventually the quality of the results, Fig. 2.4. To solve this issue, a numerical fitting of the curve is needed, which is performed through a Fast Fourier Transform (FFT) analysis of the stress output, Fig. 2.5, and taking as amplitude the maximum of the FFT response and as frequency the one applied as a boundary condition, resulting in a nice fit for the stress, as observed in Fig. 2.4. Once the stress fit is complete, it is possible to compute the material's rheological properties through the complex modulus. As the name suggests, it is a complex number, defined as $G^* = G' + jG''$, where the real part G' is called storage modulus, the imaginary part G'' is the loss modulus, and j is the imaginary unit. They define the elastic and dissipative energy in

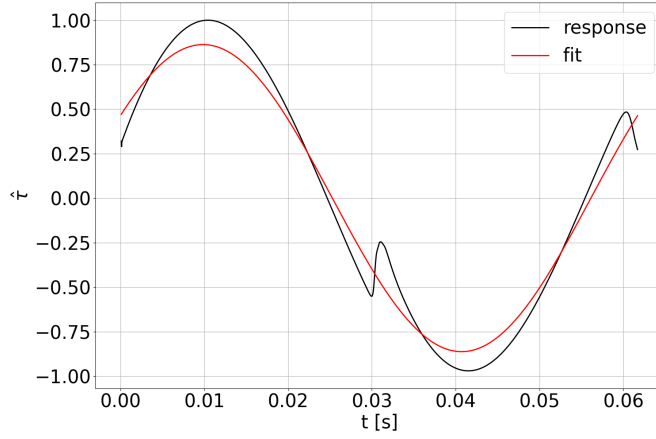


Figure 2.4.: Stress response obtained with oscillatory shear deformation, highlighting the eigenfrequency component disturbance and the fitted curve. The shear stress is normalized following $\hat{\tau} = \frac{\tau}{\max(\tau_r)}$, where τ_r is the material response stress signal.

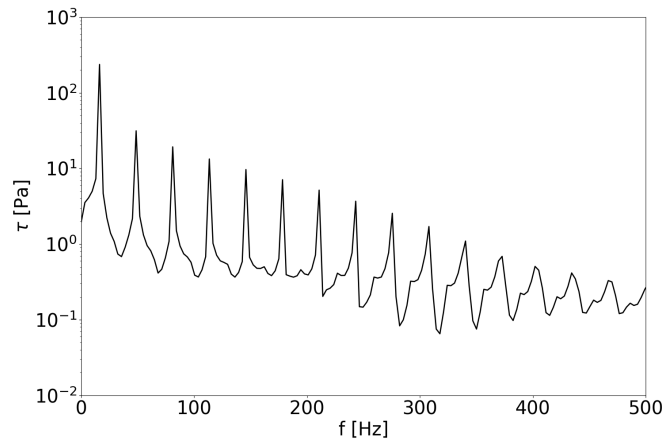


Figure 2.5.: Discrete Fast Fourier Transform of the stress signal output of an oscillatory shear rheometer simulation. The FFT analysis is performed using a Python script. Note that the presence of numerous eigenfrequencies, in addition to the frequency of oscillation, is recognizable via the multiple local maxima.

the material, respectively. In a viscoelastic material, it is expected that given an input deformation of the form $\gamma(t) = \gamma_0 \sin(\omega t)$. The stress would have a response function of the form $\tau(t) = \tau_0 \sin(\omega t + \varphi)$ where φ is the phase lag between the two signals, Fig. 2.6, which in this case is computed by interpolating the stress response with a dummy function of the form $\tau_{int} = \tau_0 \sin(\omega t + c)$ and solving for c in a Python script. Once the interpolation returns a solution, all the information needed to characterize the material

is available and the storage and loss moduli are computed respectively as $G' = \frac{\tau_0}{\gamma_0} \cos \varphi$ and $G'' = \frac{\tau_0}{\gamma_0} \sin \varphi$.

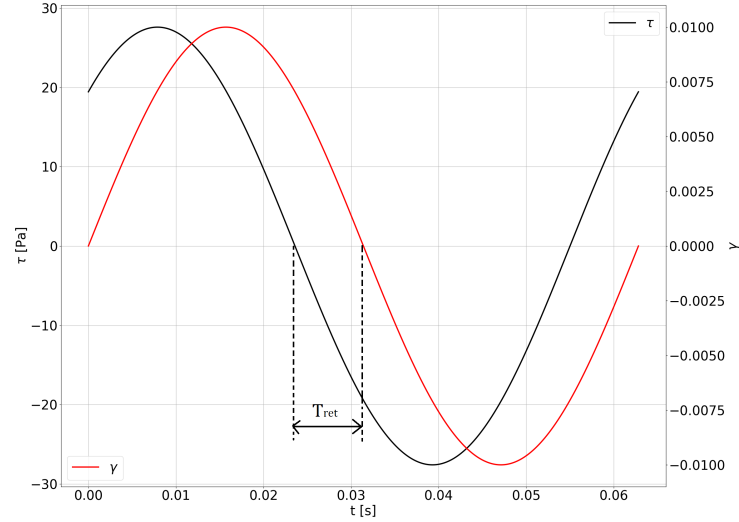


Figure 2.6.: Effect of viscoelasticity in the stress response of the material under oscillatory shear deformation. The parameters used are $\mu_m = \mu_k = 100$ Pa s, $k_m = 10$ kPa and $k_k = 1$ MPa. It is possible to observe the retardation time T_{ret} between stress and deformation, typical of viscoelastic behavior. It is related to the phase-lag φ through $T_{ret} = \frac{\varphi}{\omega}$, with ω the frequency of the applied oscillatory strain.

Effect of particles size

It has already been anticipated that the model presented in this paper aims to describe granular systems and homogeneous dispersion, which are usually granular or multiphase in the microscopic structure. DEM simulations do not need to refine their particle size to meet experimental data, as it would be done in a mesh-based method. Still, in our study, it has been observed that a decrease in particle size to simulate the same volume (hence with an increase in the number of particles per volume) would reflect a smaller error with respect to the analytical solution, as shown later in this paper.

Accuracy of the Burgers model to predict elastic behavior

To have a known solution to compare the model to, the perfectly elastic behavior of a solid is used as an analytical comparison, with Young's modulus of $E_{el} = 1$ MPa. The parameters of the Burgers model needed to obtain an elastic behavior can be found from a simple order of magnitude analysis of the constitutive relation. Specifically, if one would divide Eq. (2.1) by $\mu_m \cdot \mu_k$ and let $\mu_m, \mu_k \rightarrow \infty$, the following is obtained

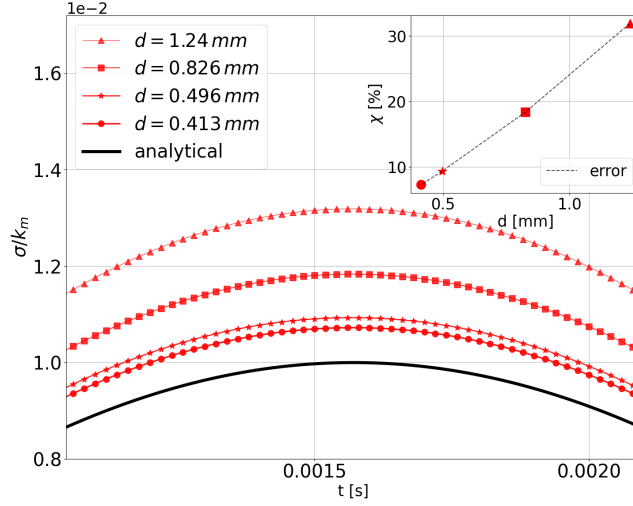


Figure 2.7.: Stress output convergence of a Simple Cubic geometry under oscillatory compression at decreasing particle size and its relative error with respect to the analytical solution. The insert shows the relative error as a function of the particle diameter.

$$\frac{1}{k_m k_k} \frac{d^2 \sigma}{dt^2} = \frac{1}{k_k} \frac{d^2 \varepsilon}{dt^2}. \quad (2.14)$$

It is straightforward to observe that by integrating twice in time and taking as initial conditions $d\sigma/dt = \sigma = 0$ and $d\varepsilon/dt = \varepsilon = 0$, the elastic relation $\sigma = k_m \varepsilon$ is obtained, hence $k_m = E_{el} = 1$ MPa. It is noteworthy that only the Maxwell spring will dictate the magnitude of the stress response, making it easier to compare with the analytical solution.

The simulation setup comprises an ordered lattice, in this case, a Simple Cubic (SC), to define a cube of constant volume $V = 0.125 \text{ cm}^3$. The cube is then deformed in a periodic uniaxial compression/expansion cycle with $\varepsilon = 0.01 \sin(\omega t)$. Moreover, 4 particle sizes are simulated. Their size is computed starting from the number of particles N_{side} laying on each side of the cube such that $D + (N_{side} - 1) \cdot \delta = V^{1/3}$, leading to the values of diameters shown in Table 2.1. Moreover, the shear component of the contact force has been turned off. Otherwise, there would be the need to scale the shear parameters with respect to the normal ones [57, 58, 59].

As shown in Fig. 2.7, the solution slowly approaches a value close to the analytical solution by decreasing the particle size in a constant volume. In particular, looking at the plot of the relative percentage error, computed as

$$\chi = 100 \left| \frac{\max(\sigma_{an}) - \max(\sigma_{sim})}{\max(\sigma_{an})} \right|, \quad (2.15)$$

Table 2.1.: Particles size relative to different number of particles N in the Simple Cubic configuration of a constant volume $V = 0.125 \text{ cm}^3$.

Type	N	d
Coarse	64	1.24 mm
Medium-coarse	216	0.826 mm
Medium-fine	1000	0.496 mm
Fine	1728	0.413 mm

a linear trend is observed where σ_{an} and σ_{sim} are the analytical and simulated stress response curves. This would imply that any further decrease in size would scale the error linearly, which is not ideal since computational time does not scale linearly with particle size. A better scenario would be if the error would decrease with a power of 2 or higher, such that an order of two higher accuracy justifies the increase in computational time.

Effect of packing geometry

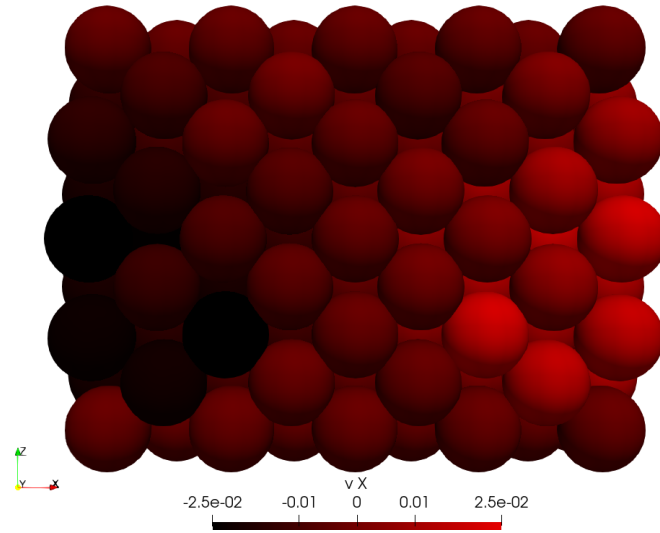


Figure 2.8.: Effect of uniaxial compression on the elastic Burgers material. Boundary conditions are applied similarly as for the shear oscillation case, with the only difference that here the periodic motion is substituted with a linear uniform velocity in the negative z -direction. It is clear how the particles at the sides are displacing laterally with respect to the direction of the applied deformation.

Remembering the simple cubic geometry of Fig. 2.3, where all the particles are perfectly aligned, it must be said that it is not representative of real-world applications. If one would want to observe the behavior of elastic material under uniaxial compression,

for example, one is expected to see a deformation in the direction normal to the compression. However, in the case of a simple cubic, even though there is an active shear component of the contact force, no lateral deformation is obtained. Hence the Poisson's ratio is equal to zero.

This is not true for other lattice geometries, for example in Fig. 2.8, where a Face Centered Cubic (FCC) lattice has been used. Here, particles are displaced in the direction of compression (z-axis) and laterally (x-axis). Furthermore, using a FCC improves the accuracy of the model, as can be observed in Fig. 2.9. The same cyclic compression test is performed for the results of Fig. 2.7, with particle sizes that are slightly different due to the different lattice scaling, as shown in Table 2.2. In this case, the error is already much smaller in magnitude even at higher diameters, showing a non-linear regression, thus reaching more accurate solutions faster than an SC. In this case, the stress response computed differently than the SC given the different configuration is compared again with the analytical solution to highlight the higher accuracy. The equation for the stress in an FCC is

$$\tau = \frac{\sum_i^{N^2} f_i}{(D + \sqrt{2}(N_{side} - 1) \cdot \delta)^2}. \quad (2.16)$$

Table 2.2.: Particles size relative to different number of particles N in the Face Centered Cube configuration of a constant volume $V = 0.125 \text{ cm}^3$.

Type	N	d
Coarse	172	0.946 mm
Medium	666	0.614 mm
Fine	1688	0.454 mm

If one performed the same test with an active shear Burgers element, there would be the need to scale shear contact parameters, as shown later in the manuscript, using [5],

$$c_m^s = \frac{c_m^n}{\alpha}, \quad (2.17)$$

with α being the scaling coefficient. The same applies for c_k^s , y_m^s , y_k^s . Moreover, the effect of different normal-to-shear ratios has been analyzed, showing the error between the analytical solution and numerical simulation in Table 2.3. It is clear that a higher ratio, hence smaller shear parameters, would reduce the intensity of the total stress response. In this case, since an elastic bulk has been simulated, hence the analytical solution is known, it would be straightforward to find the optimum ratio through a minimization algorithm, but in the case of materials in the viscoelastic regime, that change their properties depending on the time-scale of the applied stress/strain, a more detailed calibration is needed to match experimental and simulated properties as best as possible.

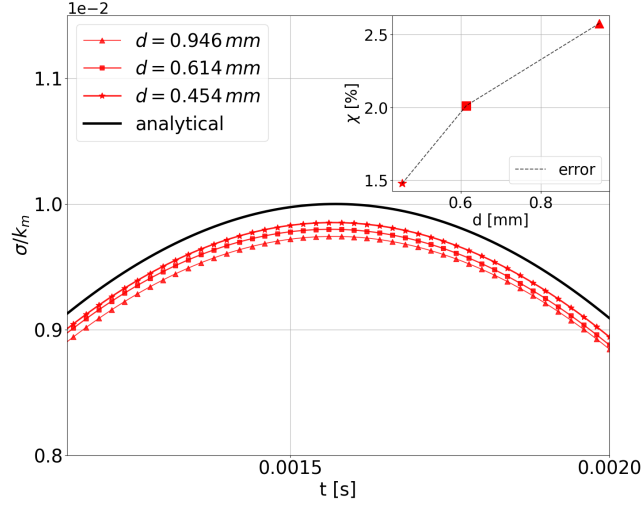


Figure 2.9.: Stress output convergence of a Face Centered Cube geometry under oscillatory compression at decreasing particle sizes and its relative error with respect to the analytical solution. Here the shear component of the force has been turned off. Differently for the Simple Cubic case, here, the error does not scale linearly, showing the importance of the packing geometry/distribution for the quality of the results.

Accuracy of Burgers model when predicting creep behavior

To further describe the model accuracy, a creep test is used as a benchmark since the analytic solution of a Burgers material under creep is well known and it reads as follows

$$\varepsilon(t) = \sigma_0 \left[\frac{1}{k_m} + \frac{1}{k_k} \left(1 - e^{-\frac{t}{\tau_k}} \right) + \frac{t}{\mu_m} \right], \quad (2.18)$$

where σ_0 is a constant stress applied on the sample. The setup is the same as Sec. 2.2, i.e. an FCC lattice cube with the tangential component of the contact force turned off, with the difference that now we are applying constant stress on the top layer of particles in the vertical direction, not in shear, and we are measuring the relative deformation. It is like we are hanging a weight on it and looking at how much it extends with respect to its original length. Once again, we observed a reduction of the error at decreasing particle size, even though it is higher in magnitude when compared with the elastic behavior, as seen in Fig. 2.10.

2.3. Calibration strategy

Every time a numerical model is implemented to solve a specific mechanical system, be it a solid structure, an airflow around a wing, and so on, an error is introduced.

Table 2.3.: Relative error between the analytical solution of elastic body and simulation of elastic Burgers materials with varying normal-to-shear parameters scaling factors α . Here, the alpha value increase has shown a corresponding relative error reduction.

α	χ
3	32.22 %
5	12.5 %
7	3.35 %
10	4.02 %

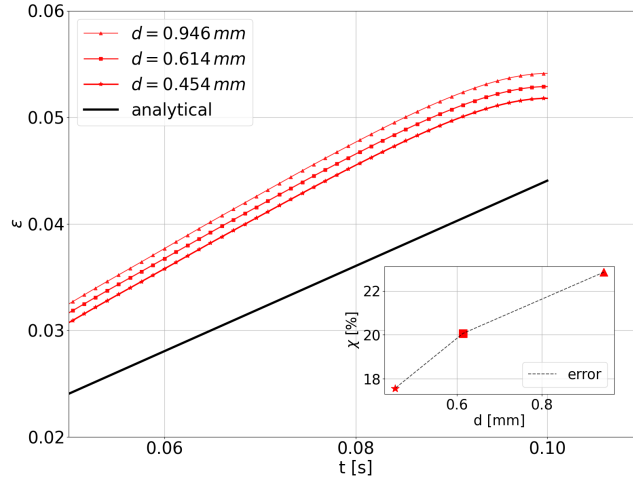


Figure 2.10.: Error reduction on a constant volume simulation of creep test at decreasing particle sizes. The zero derivative at the r.h.s. of the plot is due to a low-pass filter that is applied to filter the high-frequency oscillation in the material response.

These errors are intrinsic to the model implementation and discretization. Whenever a simulation is produced, it needs to be compared with its real-world counterpart to be sure that the variables computed in the simulation are within a relatively small margin of difference from the experimental data. Given the fact that most numerical schemes use a large set of parameters to define the model and to find the optimal parameters for a specific problem, a so-called calibration is sought out. The calibration process is usually time-consuming, as it needs to go back and forth from simulation to error evaluation until a minimum is reached. The approach here aims to reduce the number of parameters to calibrate whilst maintaining a high-quality simulation output. Most of the work in literature dealing with the Burgers model follows a similar way of approaching this problem by finding the micro-contact parameter through the minimization of a cost function and directly inserting said parameters in the model with the proper scaling

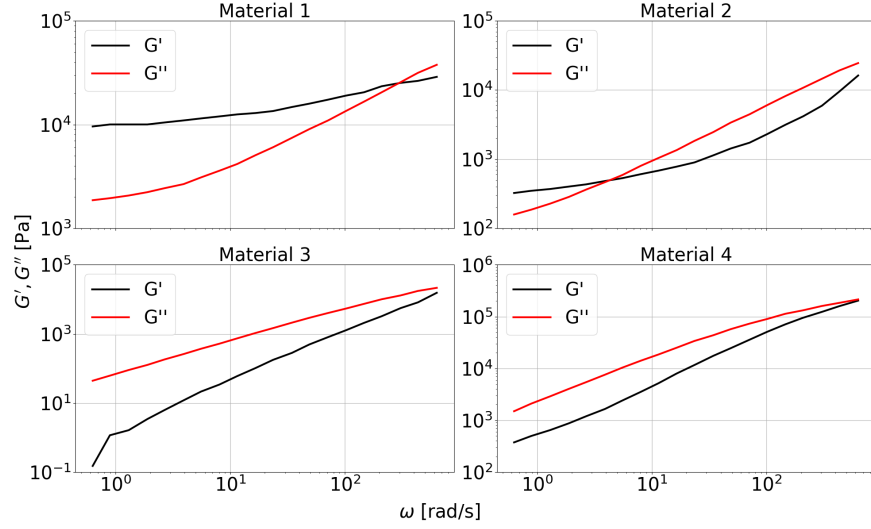


Figure 2.11.: Storage and loss modulus obtained from Oscillatory Shear Rheometer experiments of different viscoelastic materials. This is the dataset used as a base for the calibration as each material shows a noticeably different viscoelastic behavior on a wide range of frequency, hence testing the ability of the model to describe a large class of materials.

[51, 52, 59]. Some work shows also the effect of fitting the normal and shear micro-parameters separately, but with the need for Oscillatory Rheometer data in both shear and compression setups [60].

In the current study, the methodology described above will be used, which, for the Burgers model, follows these steps:

1. Rheological data from an experiment, usually in the form of the storage and loss modulus G'_{exp} , G''_{exp} is used as input in a Python script.
2. Using the following equations [61], analytical values for the rheological properties as G'_{an} and G''_{an} are computed within the Python script:

$$\begin{aligned}
 J' &= \frac{1}{k_m} + \frac{k_k}{k_k^2 + (\omega\mu_k)^2} \\
 J'' &= \frac{1}{\omega\mu_m} + \frac{\omega\mu_k}{k_k^2 + (\omega\mu_k)^2} \\
 G'_{an} &= \frac{J'}{J'^2 + J''^2} \\
 G''_{an} &= \frac{J''}{J'^2 + J''^2}
 \end{aligned}$$

with J' and J'' being the storage and loss compliances, respectively, ω is the oscillation frequency in rad/s.

3. A cost function is defined, which evaluates the difference between the experimental and analytical data

$$f_{cost} = \sum_i^m \left[\left(\frac{G'_{an}}{G'_{exp}} - 1 \right)^2 + \left(\frac{G''_{an}}{G''_{exp}} - 1 \right)^2 \right]. \quad (2.19)$$

4. The cost function is then inserted in an optimization algorithm, namely the built-in Python optimization scheme "Nelder-Mead". This algorithm minimizes the cost function by varying the model parameters μ_m , μ_k , k_m and k_k . Once the desired residuals are obtained, the optimal parameters are given and can be used as input for the DEM simulations.

Once the minimization is complete, it will return the optimal parameters, which will then be scaled as in Eq. (2.3) to define the micro-contact.

2.3.1. Limitation of Burgers model

The Burgers model has been widely used in literature to simulate the viscoelastic behavior of a wide range of materials, from asphalt[60] to oil sands[50], coke/pitch mixtures[51], to mention some. To begin with, the experimental data of Fig. 2.11 is taken as input for the calibration. This dataset is of particular relevance as not only does it show a variety of material behavior, but it also covers a wide range of applications, with an angular frequency spanning from 0.63 rad/s to 632 rad/s. If one would try to use the fitting procedure described in Sec. 2.3, let's say on material 1 of Fig. 2.11, for example, one would obtain something similar to the plot of Fig. 2.12. This is mainly due to the lack of parameters to properly fit through a large dataset [62]. Moreover, the quality of the fitting has been quantified by computing the Root Mean Square Deviation (RMSD) as

$$RMSD = \frac{100}{\max(y) - \min(y)} \sqrt{\frac{\sum_i^N (\bar{y}_i - y_i)^2}{N}}, \quad (2.20)$$

where \bar{y} is the predicted value, in this case, the simulation output, and y is the real value, with N being the number of data points.

One way to overcome this issue is to reduce the range on which the data is fitted, similarly to what Feng et al.[63] proposed, and then perform the normal calibration procedure on each data chunk separately before rejoining the data together. In particular, 5 chunks have been chosen in our study, each composed of 4 frequencies, which lead to the calibrated parameters found in Table 2.4. Even though this works quite nicely for the fitting procedure, as shown in Fig. 2.13, it leads to some problems, especially when going into the simulation realm. The biggest drawback is that a non-constant set of parameters is produced for each chunk and not only do they differ greatly, as it can be seen in Table 2.4, hence making the use of an average not feasible, but it also limits the use of this model in an industrial process simulation since there would be the need to adapt parameters to the local shear rate.

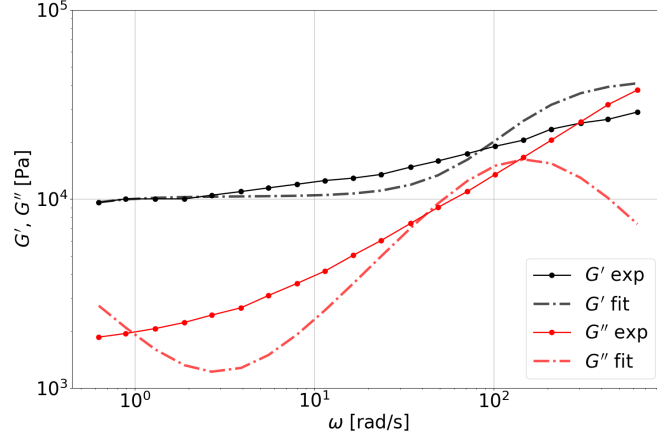


Figure 2.12.: Attempt of fitting the experimental data of material 1 using the Burgers model. Given the limited number of relaxation times of the model, it is heavily limited in accurately fitting through a wide range of frequencies, giving an RMSD of 40% for G' and 35 % for G'' .

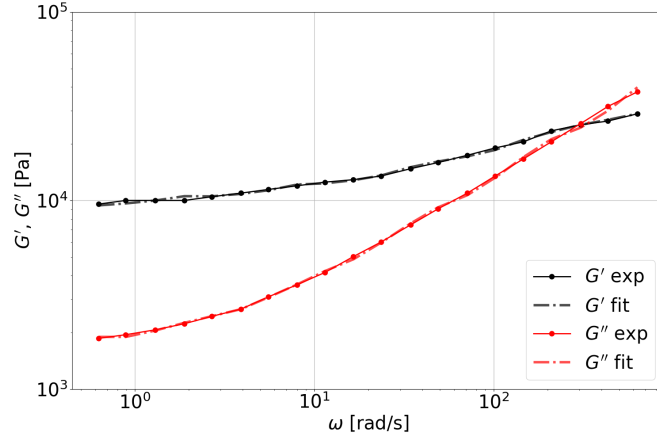


Figure 2.13.: Improved fitting of experimental data of material 1 when using the Burgers model. This result is obtained by dividing the dataset into smaller subsets and performing the analytical fitting on the latter. The fit quality is noticeably increased, giving an RMSD of 1-2% for the whole dataset. However, it produced non-constant parameters through the frequency range.

Once the parameters are known, it is possible to perform the frequency sweep simulation of the Oscillatory Shear Rheometer.

As shown in Fig. 2.14, in addition to a non-constant set of parameters, the error is not acceptable to consider this model accurate enough, at least not on a large dataset. Moreover, some notes are needed about this result. First, the amplified frequency method [64] has been used to improve the speed of the low-frequency simulations, multiplying

Table 2.4.: Calibrated parameters of Burgers model relative to material 1. The dataset has been divided into subsets with a smaller range of frequencies to obtain a good quality fit of the experimental output. To notice how certain parameters vary by some order of magnitude at increasing frequency. Damping coefficients μ_m and μ_k are in [Pa·s], and spring coefficients k_m and k_k are in [Pa]

ω range [rad/s]	μ_m	μ_k	k_m	k_k
0.6-1.9	$1.325 \cdot 10^5$	$1.55 \cdot 10^4$	$1.36 \cdot 10^4$	$3.24 \cdot 10^4$
2.7-8.1	$3.76 \cdot 10^4$	$0.31 \cdot 10^4$	$1.8 \cdot 10^4$	$2.62 \cdot 10^4$
11.5-34.1	$0.85 \cdot 10^4$	658.1	$3.22 \cdot 10^4$	$2.14 \cdot 10^4$
48.8-146.5	$0.16 \cdot 10^4$	220.2	$7.33 \cdot 10^4$	$2.56 \cdot 10^4$
209.3-632.4	$3.75 \cdot 10^2$	77.86	$5.03 \cdot 10^5$	$3.98 \cdot 10^4$

the damping coefficients and the frequency by a constant value. Even though Liu et al.[64] used this method specifically for asphalt mixtures simulations with the Burgers model, it proved to be applicable for a more general case as well. Secondly, the ratio between normal and shear parameters has been chosen to be $\alpha = 2.7$, which worked well for material 1 but not for other materials of the same dataset, meaning a proper calibration of this parameter is needed. Overall, given the limits of Burgers material to fit through the data with a unique set of parameters, which would highly compromise the applicability in industrial processes, the decision to implement a Generalized Maxwell model has been taken.

2.3.2. Fitting quality of a generalized Maxwell model

When performing the analytical fitting of experimental data with the Generalized Maxwell Model, the same procedure as the one described in Sec. 2.3 for the Burgers constitutive relation is followed, with the difference that the equations used to compute the predicted storage and loss moduli are respectively [61]

$$G' = \sum_j^4 \frac{k_j(\omega\tau_j)^2}{1 + (\omega\tau_j)^2} + k_e, \quad G'' = \sum_j^4 \frac{\omega\mu_j}{1 + (\omega\tau_j)^2}. \quad (2.21)$$

Before diving into the 4-element model, it is noteworthy to mention that a 3-element model has been previously used to fit the experimental data with poor results, Fig. 2.15, giving values of $RMSD_{G'} = 19\%$ and $RMSD_{G''} = 8\%$, which is an improvement with respect to the Burgers model, but is not enough, hence the choice for a 4-element approach. The optimization algorithm is done in Python, leading to the fit of Fig. 2.16 for material 1 of the dataset of Fig. 2.11, the same fit quality is achieved in the other materials of Fig. 2.11 as well, not shown for simplicity. Moreover, the calibrated parameters for each material are shown in Table 2.5 and the relative RMSD errors of each material fit in Table 2.6.

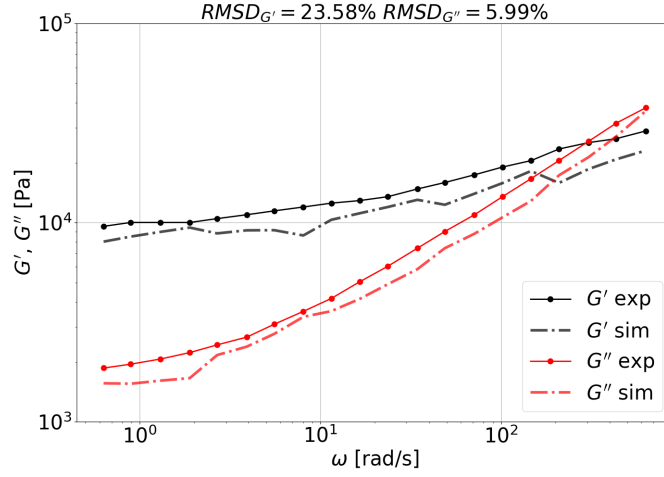


Figure 2.14.: Simulation output with fitted Burgers model parameters of Oscillatory Shear deformation of material 1. The parameters used for the simulation are shown in Table 2.4, hence with non-constant parameters throughout the dataset. The RMSD for G' is 25%, while for G'' is 21%.

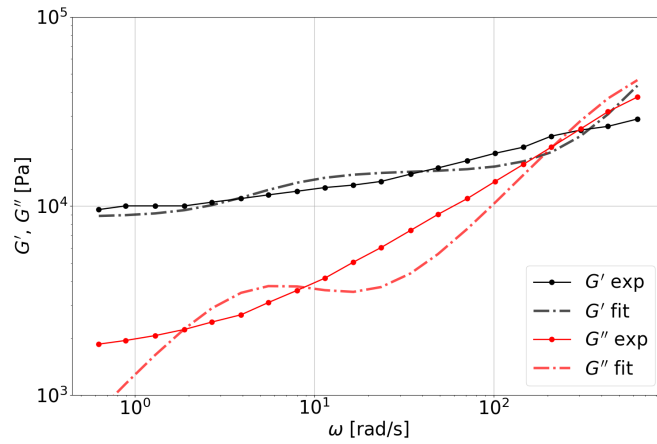


Figure 2.15.: Analytical fitting of experimental data of material 1 using the Generalized Maxwell Model constitutive relation with 3 elements and a spring. The combination of a large dataset and 3 timescales is not enough to achieve a good fit.

2.3.3. Calibrating the normal-to-shear scaling parameter

As already discussed in Sec. 2.3.1, while the use of Eq. (2.17) is largely used in literature to address the scaling between normal and shear micro-contact parameters[5, 57, 65], in this study it has been decided to improve accuracy by tuning α for each material in the experimental dataset. This is done by executing a calibration algorithm in a more classical way, i.e. by simulating a frequency sweep with a first guess value, evaluating

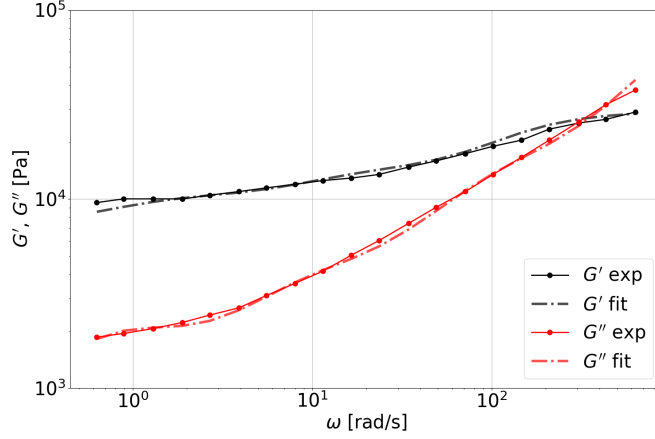


Figure 2.16.: Analytical fitting of experimental data of material 1 using the Generalized Maxwell Model constitutive relation with 4 elements and a spring. It is immediate to observe a good quality fitting through all the points, which gives 4% RMSD for G' and 3% for G'' while keeping the parameters constant. This is achieved thanks to the larger number of relaxation times of the Generalized Maxwell model.

the error with respect to the experimental data, updating the value, and re-running the frequency sweep until a minimum is reached. The value update is done separately in a Python script using a scalar minimization algorithm, namely the Bounded Brent method [66]. Moreover, given the fact that the low-frequency simulations can not be amplified in this case, as the method used in [64] has been proven to work with Burgers but not with other models, it has been decided to perform the calibration in the range of frequency $\omega > 100$ rad/s, and then run only one frequency sweep at the lower frequencies with the calibrated value of α to check if the simulation accuracy is maintained. Starting from a first guess value of $\alpha = 1$, the root mean square deviation, Eq. (2.20), is checked at each iteration, and the threshold to trigger calibration is $\max(RMSD_{G'}, RMSD_{G''}) \geq 10\%$. To be noted that a smaller value for the threshold can be used, depending on the specific application. Here, given the informatory and descriptive purpose of the manuscript, a value of 10% is used. Once the calibration procedure is completed, it gives the optimal values of α of Table 2.7.

The contact parameters and the normal-to-shear ratio are now calibrated for each material. Hence it is possible to check the quality of the simulations at lower frequencies by running a single frequency sweep in the range $\omega > 10$ rad/s. A FCC packing is used with $N=666$ particles with diameter $D = 0.4$ mm and a deformation $\gamma = 0.01$ is applied, the Oscillation amplitude (A) $A = 0.01H$, with H being the height of the cube. The aforementioned simulations produced the plots of Fig. 2.17 comparing the simulation output against its experimental counterpart. It can be immediately seen how the error is reduced with respect to the Burgers model case, both for G' and G'' , even though the frequency range is smaller. Moreover, it must be remembered that the parameters are

Table 2.5.: Calibrated macro parameters of the Generalized Maxwell model for the experimental data of Fig. 2.11. Note how the parameters stay constant for each material, unlike the Burgers model case. The need for increased relaxation times, hence more parameters, is justified. Damping coefficients $\mu_{1,2,3,4}$ are in [Pa·s] and spring coefficients $k_{1,2,3,4,e}$ are in [Pa]

Material	μ_1	μ_2	μ_3	μ_4	k_1	k_2	k_3	k_4	k_e
1	3711	108.7	63.1	373.4	3067	$1.39 \cdot 10^4$	$3.98 \cdot 10^6$	4065	7423
2	24.6	251.2	49.4	50.7	1698	160	337.4	$5.88 \cdot 10^4$	232
3	46.1	14.5	7.3	4.8	$4.78 \cdot 10^4$	1609	116.1	$9.92 \cdot 10^4$	0
4	535.2	0	927.4	681.4	$4.52 \cdot 10^5$	0	$6.73 \cdot 10^4$	3785	359.4

Table 2.6.: Root mean square deviations of the analytical fit of the experimental data of Fig. 2.11

Material	$RMSD_{G'}$	$RMSD_{G''}$
1	4.16%	3.27%
2	1.21%	1%
3	1.49%	0.57%
4	3.43%	2%

Table 2.7.: Normal-to-shear ratio calibrated parameters for the materials of the experimental dataset. Only material 1 has a ratio larger than one, being also the only material with $G' > G''$ in the whole frequency range of interest

	Material 1	Material 2	Material 3	Material 4
α	2.135	1.089	1.026	1.017

constant throughout the dataset, as opposed to the Burgers model case. Notably, all materials in the study, except material 1, produced a scaling factor $\alpha \approx 1$. This explains why material 1 is also the only one with $G' > G''$, whereas the opposite is observed for the other cases. This can be explained by the fact that a more elastic material's shear interactions are overestimated. At the same time, they have the same or even higher magnitude in more viscous materials, as expected. To conclude, not all materials managed to stay below the 10% limit error.

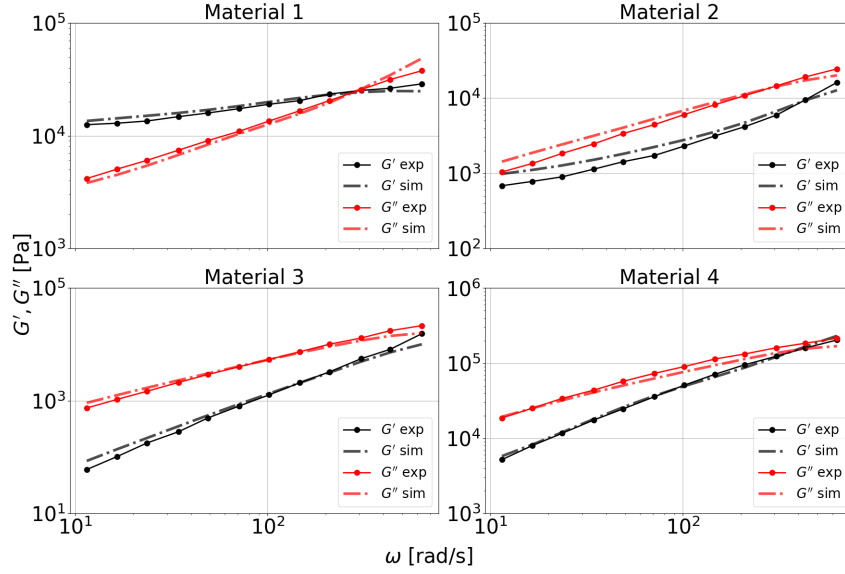


Figure 2.17.: Simulation output of the frequency sweep oscillatory shear deformation performed on the materials of Fig. 2.11, with calibrated macro parameters from Table 2.5 and normal to shear ratio from Table 2.7. Quantitatively, the rheological properties are predicted with good accuracy overall. Some inaccuracies are present qualitatively, for example regarding material 4, where the characteristic frequency at which G' and G'' overlap is highly underestimated. On the other hand, a good prediction is obtained for material 1 regarding the same quantity.

Table 2.8.: Root mean square deviation, shown as relative percentage error, of the simulation output vs the experimental data.

	Material 1	Material 2	Material 3	Material 4
$RMSD_{G'}$	9.65 %	7.01 %	10.39 %	4.38 %
$RMSD_{G''}$	9.82 %	6.36 %	9.43 %	9.94 %

2.4. Oscillatory plate-plate shear rheometer simulation

The results obtained with the cube simulations are promising but limited since they represent an ideal case with geometrical symmetry, which is far from real-world cases. For a more meaningful comparison, we decided to simulate the behavior of materials 1 and 2 in a plate-plate shear rheometer. It comprises a fixed plate on the bottom and a mechanical drive plate on the top. In between, the material is placed. Once the setup is complete, the top plate rotates around its axis with a strain-controlled motion, i.e. the oscillations follow a function of the type $\theta_0 \sin(\omega t)$, where θ_0 is the amplitude of

oscillation angle, given by $\theta_0 = \frac{180\gamma H}{\pi D}$. The value of $\gamma = s/h$ is chosen as the shear deformation at a distance $D/2$ from the center, where D is the plate diameter, s is the arc length at $D/2$, and H is the distance of the plates, Fig. 2.18. Moreover, as done for the cube, a frequency sweep is carried out in the same range.

To reduce the number of particles, instead of simulating the full disk, a ring is created with the following geometry: internal diameter $D_{int} = 0.01$ m, external diameter $D_{ext} = 0.012$ m, plate-plate distance $H = 10^{-3}$ m, particle diameter $D = 10^{-4}$ m, and deformation angle $\theta = 0.0955^\circ$. This angle is calculated starting from a deformation $\gamma = 0.01$ at the external radius, Fig. 2.19. The geometrical parameters are not representative of a real setup. Still, they are chosen according to particle size to maintain good accuracy, following the convergence study of the previous sections.

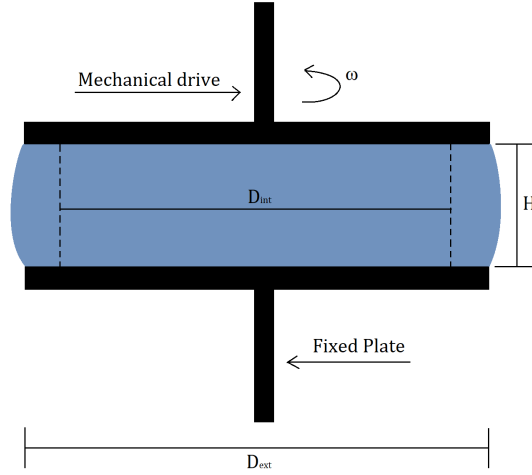


Figure 2.18.: Simple geometrical representation of plate-plate shear rheometer. In experiments, the material in between is not constrained laterally. Hence it deforms due to centrifugal inertia. This is a limitation in experiments as higher frequencies/amplitudes lead to an overflow of the sample from the setup. The simulation is based on this configuration, but it is not a digital twin of an existing setup.

An oscillatory motion is applied on the top layer of particles, with the same frequency range used on the cube. The stress is computed as the sum of the forces in the tangential direction on every single particle, given by

$$\sigma = \frac{\sum_i^N f_{i,\theta}}{A_{ring}} \quad (2.22)$$

where $f_{i,\theta} = f_{i,y} \cos\left(\text{atan2}\left(\frac{y_i}{x_i}\right)\right) - f_{i,x} \sin\left(\text{atan2}\left(\frac{y_i}{x_i}\right)\right)$ is the i^{th} particle tangential force, with $f_{i,x}$, $f_{i,y}$ its x and y force components and x_i , y_i its x and y coordinates. Moreover, atan2 is defined as

$$\text{atan2}(y, x) = \begin{cases} \arctan\left(\frac{y}{x}\right) & \text{if } x > 0, \\ \frac{\pi}{2} - \arctan\left(\frac{x}{y}\right) & \text{if } y > 0, \\ -\frac{\pi}{2} - \arctan\left(\frac{x}{y}\right) & \text{if } y < 0, \\ \arctan\left(\frac{y}{x}\right) \pm \pi & \text{if } x < 0, \\ \text{undefined} & \text{if } x = 0 \text{ and } y = 0. \end{cases} \quad (2.23)$$

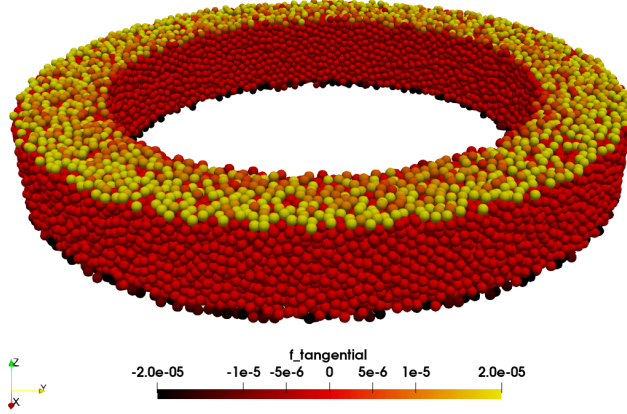


Figure 2.19.: Graphical representation of the ring shear rheometer simulation. The applied motion on the top layer of particles can be noted, given by a radial gradient of the tangential force. These are the same particles used to compute the stress as the sum of the forces on every single particle in the tangential direction, divided by the ring area.

Regarding the deformation, in a plate-plate geometry the value of γ changes linearly in the radial direction. To account for this, an average deformation is considered as $\hat{\gamma} = \frac{\gamma_{ext} + \gamma_{int}}{2} = 0.00916$. Applying the data analysis described in Sec. 2.2.3 to the stress output and using the calibrated parameters for material 1 and material 2, the plot of Figs. 2.20 and 2.21 are obtained. The model shows how, even in more complex systems, it can predict the rheology of a given material once the parameters have been calibrated for a given range of frequencies. While for material 1 the errors are both in line with what was obtained in the cube system, with $RMSD_{G'} = 14.5\%$ and $RMSD_{G''} = 11.43\%$, a different outcome is observed for material 2, where the error for G' is $RMSD_{G'} = 6.8\%$. At the same time, it is quite high for G'' , giving $RMSD_{G''} = 21.4\%$, especially due to the high-frequency results. In general, the model can behave according to the rheological properties of the calibrated material in simple and more complex systems but with reduced accuracy. It might be due to the numerical errors that arise with randomness and the increased complexity of internal structures. However, this is not clear, and it needs to be investigated further.

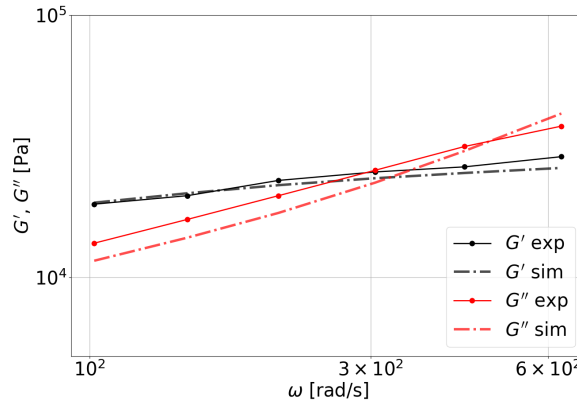


Figure 2.20.: Comparison of the simulation output from the ring shear rheometer tests and the experimental dataset used to calibrate material 1. The accuracy with respect to the cube case is only slightly decreased, and the model can predict the material's rheological properties.

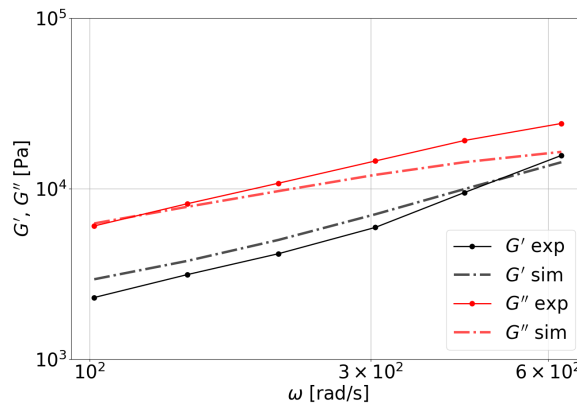


Figure 2.21.: Comparison of the simulation output from the ring shear rheometer tests and the experimental dataset used to calibrate material 2. In this case, the accuracy for the storage modulus is still maintained relatively low, while a larger divergence is observed at the higher frequency values.

2.5. Conclusions

The way the model is implemented, especially due to the presence of the bonded particles, makes it prone to disturbances in the stress response arising from the influence of the system eigenfrequencies, which are more prominent than in the experiments due to the higher inertia of the measurement instruments. Moreover, the fact that an ordered lattice is used to simulate oscillatory rheometer tests increases the magnitude of such

an effect, leading to secondary oscillations in the stress response amplitude. The use of the Fast Fourier Transform solves this issue, but not entirely, as the stress response amplitude highly depends on the particles size and lattice configuration; in other words, the mass matrix of the system is a key factor in the quality of the stress response, and an ordered lattice would increase the values on the diagonal, hence amplifying the eigenfrequency effect. This effect can be slightly countered with smaller particles, thus with lower inertia that would reduce the eigenfrequencies oscillations. Furthermore, a Burgers model has been chosen to impose the viscoelastic interaction between particles. The choice for this model resides in the fact that it has already been extensively implemented in literature, mostly for asphalt and bituminous materials [52, 57, 58, 60, 65, 67]. Moreover, since the focus of our present contribution is to obtain a model able to characterize any viscoelastic material, an experimental dataset is used, which does not comprise bitumen and/or asphalt in such a way as to test the limit of the model. The calibration is done analytically, fitting the experimental data with the Burgers model and substituting the optimal macro-parameters in the constitutive micro-contact relation after appropriate scaling. During this phase, it has been observed that the Burgers model cannot properly fit on a large dataset. Hence, the experimental data is divided into subsets, and fitting is performed on every subset. After comparing the simulation data with the experimental dataset, it has been shown that the Burgers model is not suited for any material and lacks precision when dealing with a large dataset due to its low number of parameters.

Keeping in mind the goal of the paper, which is to be able to obtain a model that maintains accuracy regardless of the size of the dataset or the material needed to be characterized, a new model with a larger number of parameters, hence more relaxation times, is implemented, namely the Generalized Maxwell model. This model immediately shows good precision when fitting the experimental data without dividing the data into subsets to maintain a good quality, hence obtaining a unique set of parameters for each material. Moreover, the model's accuracy in a more complex system has been studied, showing how the accuracy is maintained for some materials while it partially reduces for other materials, especially in the higher frequency domain.

Ultimately, this model aims at reducing the complexity of simulating processes involving viscoelastic materials using mesh-based methods. The main advantage is the meshless nature of the presented model, resulting in easier and faster modeling of the computational domain. This is of interest when dealing with moving boundaries, which are challenging to use in a mesh-based model. The use of discrete particles makes it easier to capture wall-material interactions in a more natural way, together with material flows. Future extensions of our present work could include bond breakage and particle-wall contacts and predict the non-linear behavior of real materials. In this way, it would be possible to simulate large-scale industrial processes involving viscoelastic materials and optimize those processes to reduce energy consumption, product quality, or yield.

3. A Viscoelastic Bonded Particle Model to Predict Rheology and Mechanical Properties of Hydrogel Spheres

3.1. Introduction

Hydrogels are polymer-based compounds that are highly hydrophilic. When a hydrogel absorbs water, its volume can contain up to 99% water, making it almost identical to it for some physical properties, such as refractive index [8] and density. However, its mechanical properties differ significantly from water, especially its stiffness and flow behavior. This highly hydrophilic behavior is due to the nature of the polymer chains, which are composed of many hydrophilic functional groups along the chain, attracting the hydrogen atoms in the water molecules [68]. A slight change in the composition can lead to vastly different mechanical properties. Hence, spherical hydrogels have been the focus of research in many other fields, such as biomedical, [9, 10, 11] pharmaceutical [12], agricultural [13], and so on. Given this wide range of applications, defining the mechanical properties of the hydrogels for a specific product is of utmost importance. The most common way to characterize hydrogels is experimental rheology [69], where the frequency sweep or strain sweep is the most used test since hydrogels show a viscoelastic behavior that is possible to capture with a different timescale of applied stress/strain. Alongside experiments, numerical methods have also been used to predict the behavior of hydrogels as a single particle or in a packing [14]. Each numerical model must be validated with experiments before being expanded to other applications [70]. Regarding the current work, we decided to use a bonded particle model based on the original formulation of Potyondy and Cundall [5]. Differently from other work where the viscoelastic response of deformable grains has been studied using a multi-contact model, which accounts for the increased deformability of single grains and inherently has a viscoelastic response due to the dissipative part of the contact [71, 72], here we introduce a new methodology. In our work, the single grain is composed of hard DEM spheres that do not account for multi-contact or high deformability. Still, given the bonded model's more complex viscoelastic constitutive relation used, which can predict multiple timescales, it can realistically capture high deformability for the single grain, as opposed to the multi-contact model, which is modeling the real deformation. A similar implementation is used in [15], where the single grain deformation is still modeled but with a linear, more complex viscoelastic response. Still, the goal of our work is to be able to capture the real deformation of highly deformable hydrogels and to predict the behavior of single grains and grain-grain contact. In addition, the bonded nature of

the model can describe more continuous materials, such as pastes, as done in [73]. The numerical method is first explained in detail, describing the parameters that define the forces between the discrete elements of the system. Furthermore, the experiment used as a calibration benchmark is defined such that it can be reproduced and its result is shown. Consequently, the simulation boundary and initial conditions are described, and the simulation result against the experimental data is shown with reasonable accuracy.

3.2. Methodology

The approach used here to model and simulate the response of a swollen spherical hydrogel is based on the Bonded Particle Model first introduced by Potyondy and Cundall [5]. In their original formulation, a solid bond is formed between particles when certain geometrical conditions are met. The bond produces an elastic and a dissipative force, depending on the relative motion between the particles. For this study, the forces produced by the bonds are based on the Generalized Maxwell model, which defines a viscoelastic interaction when deformed [73].

3.2.1. Bonded Particle Model

In the classical Discrete Element Method (DEM), the force between interacting particles is (almost) always repulsive, i.e., when the particles are in contact, the force is proportional to the overlap between them, and its direction is opposite to the relative normal unit vector, hence the repulsive nature of the force. However, with the Bonded Particle Model, not only are the particles not necessarily in contact, but the force can be either repulsive if the particles are getting closer to the equilibrium position or attractive if the particles are getting farther. The classical DEM contact is switched off when particles are bonded, but it is active when a particle is in contact with a particle to which it is not bonded. The model can be considered a hybrid as it allows for both a classic DEM contact and the bonded interaction, depending merely on the condition of the bond's existence. The condition for the bond creation follows the same strategy as used by Potyondy and Cundall [5], where the radii of the particles are multiplied by a constant parameter, called the radius multiplier λ , and the overlap between the increased radii is taken as a condition for the bond creation. Starting, for simplicity, with two particles i and j with equal radii r , positions \vec{x}_i, \vec{x}_j , a cylindrical bond is formed when the distance between the particles is less or equal to the sum of the increased radii, or $d = |\vec{x}_i - \vec{x}_j| \leq 2\lambda r$, with d being the distance. In general, the length and radius of the bond are defined at its creation to be $L = d$ and radius $R = \lambda \min(r_i, r_j)$ in the case of particles with different sizes. Moreover, bonds can either form continuously as the simulation advances, given the particles are close, or they are formed at a given timestep and do not form for the rest of the simulation or until a user-specified timestep. This permits the user to define separate Hydrogels that do not form bonds between them when they come into contact.

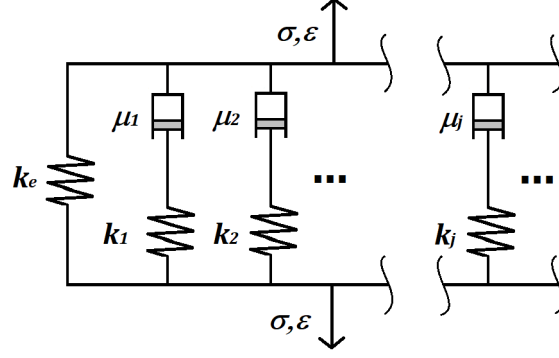


Figure 3.1.: Schematic representation of the viscoelastic element forming the Generalized Maxwell Model.

3.2.2. Generalized Maxwell Model

A Generalized Maxwell Model has been implemented to deal with the viscoelastic nature of a wide range of materials. The main reason behind this choice is the ability of the model to introduce multiple elements without necessarily making the discretization more complex. Moreover, the analytical solution is known for many simple tests, which can be helpful when validating the implementation of the model in the numerical solver. As the name suggests, the model is defined as a parallel connection of a certain number of Maxwell elements plus a spring or a dashpot, as depicted in Fig. 3.1. For this work, a version with 4 Maxwell elements and a single spring is used as this has been successfully implemented for other applications, which also shows the reason behind the choice of 4 elements [73]. Even though it appears quite complex, its implementation is relatively simple. Starting from the constitutive relation of the j^{th} single Maxwell element,

$$\frac{d\varepsilon}{dt} = \frac{1}{k_j} \frac{d\sigma_j}{dt} + \frac{\sigma_j}{\mu_j}, \quad (3.1)$$

where ε is the strain, σ is the stress, k_j is the spring stiffness, and μ_j is the damper viscosity. It is possible to transform it to its respective force-displacement relation, which reads

$$\frac{du}{dt} = \frac{1}{y_j} \frac{df_j}{dt} + \frac{f_j}{c_j}, \quad (3.2)$$

with f being the force and u the displacement. Here, a cylindrical bond shape is used to make it easier to define a limit stress for fracture, which is not implemented yet but is a natural next step to improve the model. In addition, the cylindrical shape is also used to define the micro-contact parameters and scale them with a characteristic length accordingly, resulting in $y_j = A_b/L * k_j$ and $c_j = A_b/L * \mu_j$, where A_b is the cross-section area of the bond, computed as $A_b = \pi R^2$, with L being the bond length. To conclude, the bond is merely a massless “connection” between DEM particles which carries the viscoelastic constitutive relation. Since the bond connects the centers of the

particles, L is equal to the particles' distance when the bond is formed. Hence, it is constant throughout the simulation. Moreover, a parameter called α is added, such that $k_{j, \text{shear}} = \frac{k_{j, \text{normal}}}{\alpha}$, $k_{e, \text{shear}} = \frac{k_{e, \text{normal}}}{\alpha}$ and $\mu_{j, \text{shear}} = \frac{\mu_{j, \text{normal}}}{\alpha}$, where the j subscript represents the coefficient of the spring or dashpot in the j^{th} Maxwell element and the subscript e stands for elastic and it defines the spring stiffness of the isolated spring element in the generalized Maxwell model. The choice of a single scaling parameter α is motivated by the need to keep the number of parameters (to be calibrated) as low as possible. Nevertheless, the same set of parameters is used for all the bonds in the system.

Discretization and implementation

The constitutive relation of Eq. (3.2) must be discretized in time to implement the model in the DEM code. By taking values at half timestep and computing Taylor Series expansions for the force and the displacement, centered at $t = \Delta t(n + 1/2)$, one would obtain (we note that the superscripts between curled brackets $\{\}$ in the following equations are not exponential, but they refer to the timestep index at which the variables are computed)

$$\left. \frac{du}{dt} \right|_{n+\frac{1}{2}} = \frac{u^{\{n+1\}} - u^{\{n\}}}{\Delta t} + \mathcal{O}(\Delta t^2). \quad (3.3)$$

$$\left. \frac{df}{dt} \right|_{n+\frac{1}{2}} = \frac{f^{\{n+1\}} - f^{\{n\}}}{\Delta t} + \mathcal{O}(\Delta t^2). \quad (3.4)$$

Substituting the newly found approximations for the force and displacement derivatives in Eq. (3.2), the following discretized force equation for the j^{th} Maxwell element is obtained

$$f_j^{\{n+1\}} = \frac{u^{\{n+1\}} - u^{\{n\}} + f_j^{\{n\}} \left(\frac{1}{y_j} - \frac{\Delta t}{2c_j} \right)}{\frac{1}{y_j} + \frac{\Delta t}{2c_j}}, \quad (3.5)$$

A finite deformation approach regarding the single spring force is used, given that the relative positions at the bond creation are known. Hence it is straightforward to compute the displacement relative to the bond creation timestep n_0 , leading to $f_e^{\{n+1\}} = y_e(u^{\{n+1\}} - u^{\{n_0\}})$, where y_e is the micro-contact spring stiffness of the single spring element in the generalized Maxwell computed as $y_e = A_b/L \cdot k_e$. Finally, the total force is just a sum of the Maxwell elements plus the single spring contributions, i.e. $f^{\{n+1\}} = f_e^{\{n+1\}} + \sum_j^4 f_j^{\{n+1\}}$. The new particle's position is then updated by integrating the translational equation of motion. A flowchart of the algorithm is shown in Fig. 3.2 to visualize better how particle-particle interactions are computed.

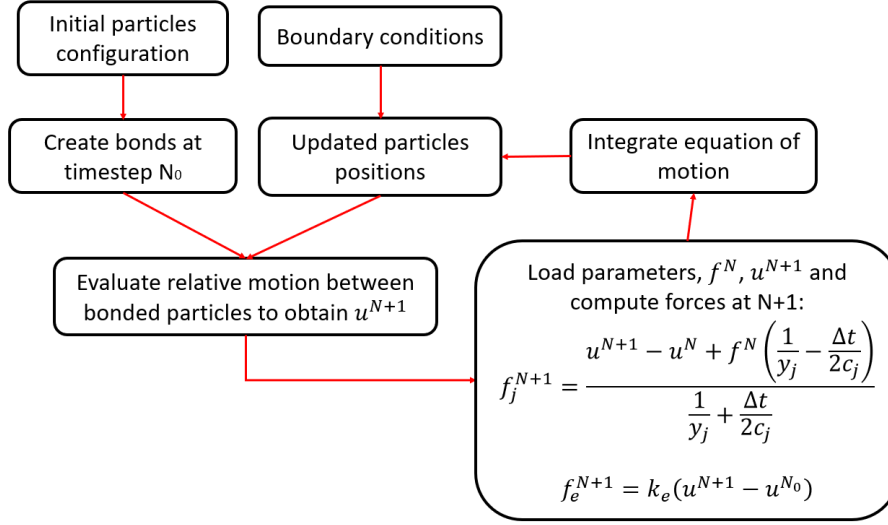


Figure 3.2.: Flowchart of the algorithm used to compute particle-particle interactions.

The rotations are turned off for bonded particles, so the model does not solve for the torques. However, it is extremely important to consider both normal and tangential displacement when computing the interactions between bonded particles. Without tangential displacement, we would lose information on the out-of-direction deformation. If we compressed a face-centered cube lattice, for example, and turned off the tangential displacement, we would not observe a lateral deformation. Such a behavior would not be physical (i.e., result in a Poisson's ratio of 0). As mentioned, the model acts in the relative normal and shear directions, with the parameters being scaled according to the value of α . Generally, the parameter α can assume any positive value, depending on the material to be calibrated and the geometry of the mechanical test used, as done in [73, 60]. In our current work, choosing α equal to unity has been found to best replicate the experimental data in Sec. 3.3.1. What is different between normal and shear directions are the values of the displacements, depending on the relative motion of the bonded particles. After solving the particle equation of motion, all the information on its position and velocity are known at the timestep $n + 1$, while quantities at timestep n are saved from previous iterations. Let two particles i and j be bonded. Their relative displacement between two consecutive timesteps is $\Delta \vec{u} = \vec{r}^{\{n+1\}} - \vec{r}^{\{n\}}$, with $\vec{r} = \vec{x}_i - \vec{x}_j$ the relative position between the particles. While the definition of the unit normal vector is relatively simple, being just the normalized \vec{r} , for the shear direction, many different ways are possible, being infinite orthogonal lines with respect to \hat{n} . The method adopted here is that of defining a bond plane between the timestep at which the bond is formed, called n_0 , and the actual timestep, considering as shear direction the unit vector orthogonal to \hat{n} which lays on said plane [55]. As a result, the unit shear vector is defined as

$$\hat{s}^{\{n+1\}} = \frac{\hat{n}^{\{n+1\}} \times (\hat{n}^{\{n+1\}} \times \hat{n}^{\{n_0\}})}{|\hat{n}^{\{n+1\}} \times (\hat{n}^{\{n+1\}} \times \hat{n}^{\{n_0\}})|}. \quad (3.6)$$

Once the principal directions at the new timestep are known, the semi-projected displacements in normal and shear directions are then computed, giving

$$\begin{aligned} \Delta u_{norm} &= \Delta \vec{u} \cdot \hat{n}^{\{n+1\}} \\ \Delta u_{shear} &= \Delta \vec{u} \cdot \hat{s}^{\{n+1\}}. \end{aligned}$$

3.3. Experimental setups on Hydrogel spheres

Two mechanical tests are conducted on the particles to observe different behaviors of the hydrogel spheres. The first experiment is on a single grain, compressed in an oscillatory motion, to measure the rheological properties under cyclic compression, which will be used as a test case to calibrate the DEM parameters. The second experiment is a particle-particle linear compression, where the two spheres are forced into contact by a vertical motion, measuring the forces in the direction of the motion.

3.3.1. Cyclic compression-extension

Sample preparation

The hydrogel used in the experiment is commercially available, with an average diameter of 19.32 mm, and kept in water until no significant increase in volume is noted.

Setup

The rheometer used is an Anton Paar MCR 702e Space. The measuring plate is an Anton Paar's PP25 with a diameter of 25 mm, while the bottom plate is an Anton Paar's L-PP50 plate with a diameter of 50 mm. Since an oscillatory compression-extension frequency sweep test is performed, the particle is placed between the moving plate and the measuring plate. To keep the hydrogel centered on the lower plate and run the experiment both in a dry and in a submerged setup, a 3D printed holder with a concave base, where the curvature radius of the base is 80 mm, has been used. This way, the hydrogel sits permanently at the center of the lower plate, maintaining a good quality measurement throughout the experiment. To better understand the setup, Figs. 3.3 and 3.4 show the sphere placement and the overall configuration of the rheometer.

Protocol

An initial preload compression strain of 5.5% of the sphere diameter was used to ensure that the contact between the measuring plate and the hydrogel would be kept during the test, thus getting the initial height to a value of $h_0 = 0.055 \cdot 19.32 \text{ mm} = 1.072 \text{ mm}$. After that, the oscillations are performed with a constant amplitude of 5% of the initial particle

diameter, resulting in a displacement of the mechanical drive of $\Delta h = 0.05 \cdot D = 0.966$ mm, giving a total strain of $\varepsilon_0 = (h_0 - \Delta h)/h_0 = 0.053$, with D the particle's diameter. The frequency sweep ranges from 0.01 rad/s to 7 rad/s, and both dry and fully submerged tests are performed.

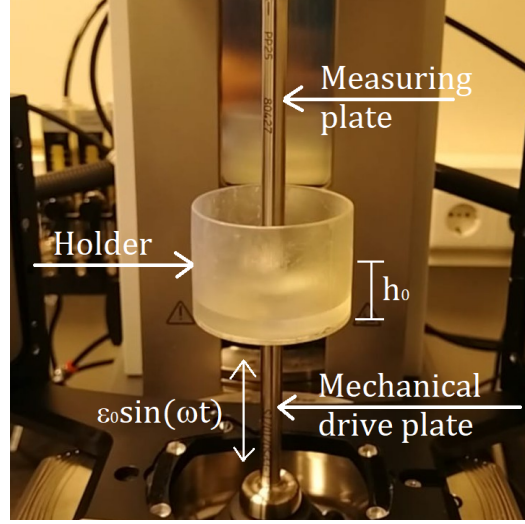


Figure 3.3.: Schematic of the experimental setup for the compression-extension oscillations on the hydrogel sphere. The sample is initially compressed to h_0 . Then, an oscillatory motion is applied from the mechanical drive with an amplitude ε_0 and frequency ω . The stress response is measured on the measuring plate and processed by the rheometer, which gives the rheological properties as output.

Unfortunately, the experimental device used in our experiments does not permit us to obtain insights on the stress distribution within the sphere. Therefore, it measures the force on the measuring plate and computes the stress σ_0 by considering the sphere as a cube with a side length equal to the sphere diameter as $\sigma_0 = f_0/D^2$, where f_0 is the force signal amplitude. Once the stress is evaluated, the rheometer compares the stress and strain signals, (the exact procedure for this has not been made known by the manufacturer), which ultimately outputs $E' = \sigma_0/\varepsilon_0 \cos \varphi$ and $E'' = \sigma_0/\varepsilon_0 \sin \varphi$, with φ being the phase shift between stress and strain waves. We understand that the quantities outputted by the rheometer are not the real E' and E'' of the material due to the stress distribution being not homogeneous in the sphere. These values simply represent the amplitude of the observed stress and its phase shift with respect to the applied strain and we call them the modified storage and loss moduli. A spherical hydrogel was used since cutting the material resulted in uncontrolled fracturing. Attempts to manufacture our own hydrogels resulted in non-uniform samples or samples whose surfaces were not flat and could not be aligned with the compression plate, producing non-uniform boundary conditions while testing. The quantities E' and E'' were used for the model calibration, and since stresses defined in the simulation were consistent, we believe there is a minimal

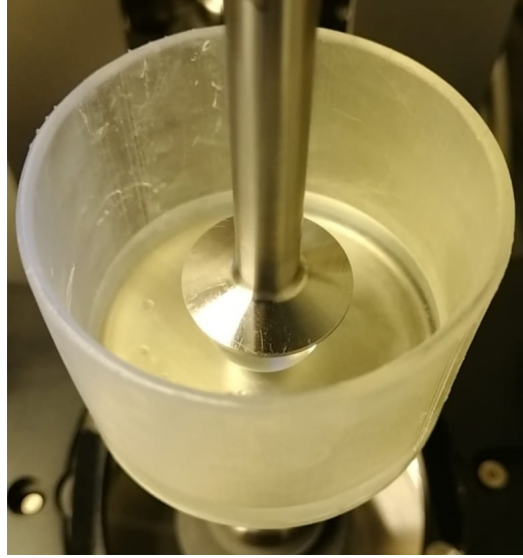


Figure 3.4.: This picture shows the placement of the hydrogel sphere, sitting on the concave bottom of the plate with the measuring plate slightly compressing to apply a preload on the sphere.

loss of information. When comparing the wet and the dry case, the same qualitative behavior is observed for both E' and E'' ; see Fig. 3.5. Additionally, a slight difference in magnitude is present. This is expected, especially at the lower frequencies, which can be explained by the fact that the rheometer first performs the oscillations at higher frequencies. Once it is time to run the lower frequencies, some water has been squeezed out of the hydrogel sphere, rendering it stiffer, thus giving higher values for the complex modulus. Given that both E' and E'' are put on the same plot in logarithmic scale, the difference only looks more prominent for E'' , although it is quite the opposite. The average difference between the dry and the wet case for E' is 863 Pa, while for E'' , it is 63 Pa. Nevertheless, the dry case is used for the calibration since considering the presence of water would significantly increase the complexity of the simulation setup.

3.3.2. Particle-Particle compression

Sample Preparation

The hydrogel spheres used in this test are similar to the ones used in section 3.3.1. Educational Innovation Inc. manufactures these. The dry hydrogels are grown in Milli-Q water mixed with Nile Blue Perchlorate dye (dissolved in absolute ethanol) for a minimum of 24 hours at a lab temperature of approximately 19 degrees Celsius. Once grown, the diameters of the spheres to be tested were measured with Vernier calipers two times in perpendicular planes. For the data sets shown in this paper, the mean diameter of the used particles is 18.365 ± 0.275 mm (upper particle) and 18.275 ± 0.275 mm (lower particle). These particles are then placed in a 3D-printed shell and clamped

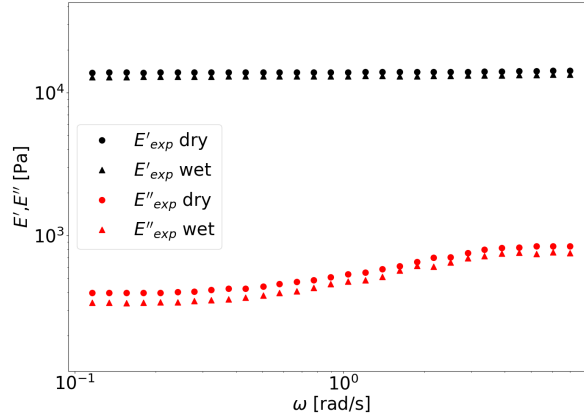
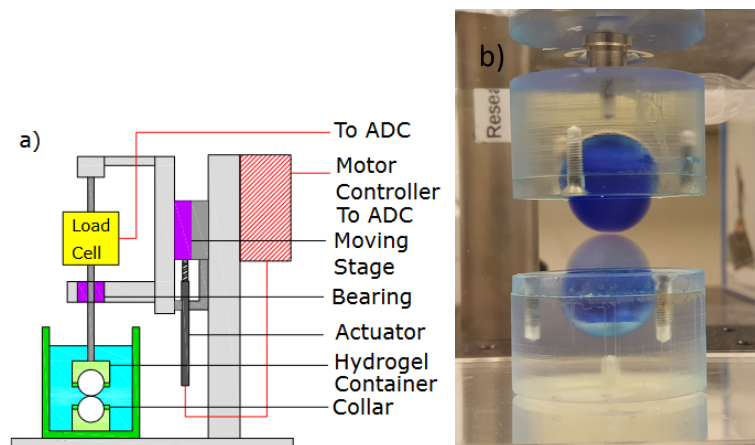


Figure 3.5.: Rheological properties of the hydrogel sphere under a cyclic compression-extension frequency sweep. The dry and the submerged cases show the same behavior with a slight difference in magnitude. The dry case is ultimately used for the calibration, but a similar result would have been obtained if the wet dataset was to be used.

down with a collar with a spherical cutout.

Setup

Based on previous work by Boots et al. [74] and Asadi et al. [75], the particle-particle compression test was conducted on a home-built setup. The schematics of the setup are shown in Fig. 3.6. In this setup, the force sensing and the motion of the particles are decoupled, meaning that there is no electronic feedback between the force measurement and the particle's motion or vice versa. The motion of the upper particle is set by an actuator (Thorlabs Z825BV) connected to a moving stage (Thorlabs MT1). It is regulated by a motor controller (Kinesis KDC 101) that can interact with a Matlab platform. Through metallic rods and posts, the moving stage is connected to a Wheatstone bridge-based S-beam load sensor (Futek LSB200 FSH03871). A strain gauge input signal conditioner (ICP DAS SG-3016) regulates the voltage supplied to the load sensor and amplifies the signal output from the load sensor. The amplified signal is then filtered through a low-pass RC filter (10Ω resistor 10nF capacitor) and converted to a digital signal with a 14-bit analog-to-digital converter (ADC) present in a National Instrument data acquisition instrument (NI DAQ 6001). This digital signal is then read into a computer using Matlab's NI Data Acquisition Toolbox. For the dataset used in this study, the sampling frequency for the load cell was set to 1 kHz. The load cell is attached to one end of a metallic rod. The other end of the rod is connected to the shell containing the hydrogel used to compress another hydrogel in a shell attached to the bottom of a static container. Both the shells and the hydrogels are immersed in Milli Q water. The alignment of the particles is done by eye and is visualized in figure 3.6b).



Protocol

The upper hydrogel is then moved down using the actuator with 0.5 mm steps at a speed of 0.3mm/s until an increment in force is detected to ascertain contact. Once contact is detected, the upper hydrogel is moved back up, and the process is repeated after a few minutes to obtain a reliable contact location.

3.4. DEM simulation

This chapter shows how the simulations for the different mechanical tests are prepared, calibrated, and performed. The calibration is the most essential element; starting from oscillatory data, it connects the real world to the simulated world.

3.4.1. Parameters calibration

At the beginning of Sec. 3.2.2, no explanation was given for why four elements for the Generalized Maxwell Model are used. Starting from the rheological properties measured, which in our case are the modified storage modulus E' and the modified loss modulus E'' as a function of the frequency ω , we will show the reason behind this choice.

3.4.2. Calibration theory

In classic DEM, the model parameters are calibrated by a simulation-evaluation-update loop. The latter consists of a loop where a simulation is run at each iteration, the corresponding output is compared with experimental or analytical values, and a cost function is evaluated and minimized, hence updating the new parameters fed into the new iteration. Here, a different approach is used, which follows the method of other works dealing with viscoelastic model calibration, i.e., finding the optimal parameters by minimization of a cost function that connects analytical and experimental data, [51, 52]. The reasons for using a different approach are mainly two. First, the number of parameters is relatively high with respect to other DEM models, making it difficult to go through the loop described above. Moreover, an analytical solution is beneficial when fitting experimental data because at least reasonable first-guess parameters can be found. Some work also shows the effect of fitting the normal and shear micro-parameters separately, but with the need for oscillatory rheometer data in both shear and compression setups [60].

In the current study, the methodology described in the following steps will be used:

1. Read rheological data from an experiment, usually in the form of the storage and loss modulus E'_{exp} , E''_{exp} .
2. Using the following equations [61] to compute E'_0 and E''_0 :

$$E'_0 = \sum_j^4 \frac{k_j(\omega\tau_j)^2}{1 + (\omega\tau_j)^2} + k_e, \quad (3.7)$$

$$E''_0 = \sum_j^4 \frac{\omega\mu_j}{1 + (\omega\tau_j)^2} \quad (3.8)$$

with $\tau_j = \mu_j/k_j$ being the timescale of the j^{th} element and the initial values are taken as unity.

3. Evaluate the cost function by comparing experimental and analytical data

$$f_{cost} = \sum_i^m \left[\left(\frac{E'_0}{E'_{exp}} - 1 \right)^2 + \left(\frac{E''_0}{E''_{exp}} - 1 \right)^2 \right]. \quad (3.9)$$

4. The cost function is then written in a Python script, where a minimization loop is chosen to find the minima of the function. For our case, a bounded Nelder-Mead algorithm is used to iterate through steps 2 and 3 until a minimum is reached, giving the optimal values of μ_j , k_j and k_e .

It is important to note that the parameters used for normal and shear directions are the same. Depending on the particles distribution and the application, the shear parameters might need to be reduced, as explained in Appendix A. Additional simulations have been performed to try and optimize the value of α , but the calibration process for this particular case would return $\alpha = 1$ as the optimal value. Hence the choice to keep $\alpha = 1$ for all the simulations. In the current work, a four elements model is chosen for the following reasons. The first and most relevant reason is that we want our model to be as general as possible and accurate for various materials on various applications. To achieve this, we want to capture the behavior of a specific material on different timescales but, at the same time, offer an efficient solver. In their book, Osswald and Rudolph [17] describe how more elements in a Generalized Maxwell model contribute to a better fit with experimental data by showing how a four elements model can predict the shape of the relaxation response function of a polystyrene melt at a given temperature.

Calibration result

We tested the fitting procedure on different data sets from different materials in our previous work [73] to determine how many elements would be good enough for a specific application. We concluded that 4 elements are best suited for general applications, whereas 3 elements lack accuracy in most cases. In our current work, fitting the experimental data with 3 or 4 elements is indifferent, as both approaches give us the same residuals shown in Fig. 3.7. However, given the fact that a 4-elements model shows increased performance on a wider range of applications, the 4-elements fit was selected. A similar implementation has been used by Ren et al. [54], without bonds and in combination with different phases behaving elastically or viscoelastically depending on the nature of the contact. They obtained a relatively good agreement with experimental data. Applying the fitting procedure to the compression-extension dataset in the dry case might prove tricky as there is more than one correct way to estimate the parameters [63]. If one tries to fit the experimental data using the method described at the beginning of this section, one will obtain the results in Fig. 3.7, which gives good quality of the fit with the root mean square errors for E' and E'' of 1.9% and 3.5%, respectively.

When calibrating the parameters of a DEM simulation, those reflect the material's behaviour under a certain range of timescales (or frequencies in this case). When using a model to simulate a process, the experiment used to calibrate the parameters needs

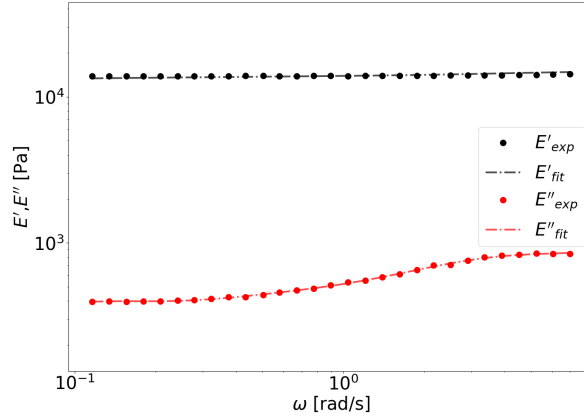


Figure 3.7.: Analytical fit of the dry oscillatory compression-extension experiment using the Generalized Maxwell model on the whole frequency range. Residuals for E' and E'' are 1.9% and 3.5%, respectively.

to have a timescale that is comparable to the one of the process, so that the model can describe the material's behaviour under the process operating conditions accurately. In our case, we show that the model maintains validity in a relatively wide range of frequencies, hence it is possible to use the same set of parameters for different operating conditions without the need to redo the calibration process. The optimal parameters are shown in Tab. 3.1. Unfortunately, there is no way of telling if the calibration falls into local minima rather than absolute ones, but this might be a realistic case. What can be said for sure is that the parameters do not directly represent, in any way, the mechanical properties of the material itself. However, combined, they can give more information on the material's mechanical properties under certain conditions. If, for example, one wanted to measure the dynamic viscosity at a given shear rate, one could apply the Cox-Merz rule [76], obtaining a relation for the dynamic viscosity at shear rates much larger or smaller than the ones used in experiments. This is true if the simulation using these parameters can reproduce the experimental data with a small error.

Table 3.1.: Optimal generalized Maxwell model parameters for the hydrogel sphere under oscillatory compression test, using a $\alpha = 1$ value. $k_{1,2,3,4}$ and k_e are the stiffness of the Maxwell elements springs, and the single spring stiffness, expressed in Pa. $\mu_{1,2,3,4}$ are the viscosity of the Maxwell elements dampers, expressed in Pa s.

ω [rad/s]	k_1	k_2	k_3	k_4	k_e	μ_1	μ_2	μ_3	μ_4
0.116-6.98	2.77e-1	9.59e2	6.6e2	7.66e4	1.31e4	1.03e5	3.99e2	4.16e3	8.34e1

3.4.3. Simulation of the single sphere cyclic compression-extension test

As mentioned before, Discrete Element Method particles are bonded together, and each bond produces a force when deformed, according to the Generalized Maxwell Model described in Sec. 3.2.2. To increase accuracy, as shown in Appendix A, the hydrogel sphere is discretized using a DEM particle diameter of $d_p = 0.35$ mm, with a total sphere diameter of $D = 6$ mm and total number of particles $N_p = 903$, as depicted in Fig. 3.8. The DEM particles are arranged by spatial discretization of the spherical coordinates defining the hydrogel sphere. Taking, for example, the top sphere, the discretization is done by first defining a shell of radius $R_0 = (D - d_p)/2$. Starting from the maximum circumference, a series of parallel circumferences are constructed, starting from the maximum one on the surface of the shell, at a distance a , called the discretization pace, with decreasing radius. This results in a distribution of points on the surface of the shell, distant from each other by less than a . The process is then repeated for each i^{th} shell with radius $R_i = R_{i-1} - ia$ until the sphere's center is reached. Different types of discretization, such as face-centered cube, simple cube, and hexagonal close-packed, have been attempted before settling for the one described above. In all cases, a good approximation of the spherical shape was not obtainable unless a very large number of particles was used. For the current discretization, which uses polar coordinates to create a sphere, good control of the internal and surface refinement levels could be achieved. The discretization of each hydrogel sphere is composed of two parts: the spatial configuration of the smaller DEM particles and their radius. As shown in Appendix A, a different spatial configuration does not affect the springs and dashpots parameters, as they are computed via analytical fitting. However, a different spatial configuration might affect the scaling between normal and shear parameters, resulting in the need to calibrate the value of α . Regarding the particles size, the choice of a smaller DEM particle radius results in more accurate simulations, but at the same time requires more computational time, hence a trade-off is needed to find the optimal DEM particles size. The timestep used in our simulations is already one order of magnitude smaller than the one used for a classical DEM-based simulation with, e.g., a Hertzian contact closure. Moreover, we simulate a smaller hydrogel than the one of the experiment. The reason behind this is to maintain accuracy whilst reducing computational time, which is done by finding a trade-off between these options.

- **Larger DEM particles for real-sized hydrogel:** this would be the most-efficient least-accurate solution, since it involves using larged DEM particles, hence lower accuracy, but with a significant lower number of particles, i.e. lower computational time, as shown in Appendix A.
- **Smaller DEM particles for real-sized hydrogel:** in terms of accuracy, this solution would deliver the best result, but given the much higher number of particles, it would be the least efficient.
- **Scaled DEM particles and hydrogel:** if we scaled down the DEM particles and the hydrogel, with a higher scaling factor for the hydrogel, we would improve

accuracy and at the same time not lose too much in efficiency. The optimum scaling ratio between the DEM particles and the hydrogel size must be chosen. It would be interesting for future applications to perform an optimization analysis on the scaling ratio that performs the best in terms of both accuracy and efficiency.

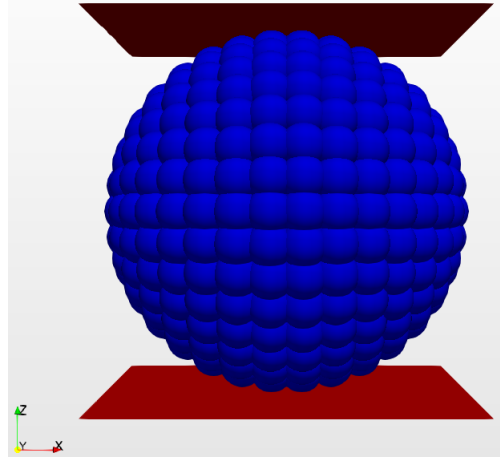


Figure 3.8.: The hydrogel sphere is discretized using smaller DEM particles bonded together. The plates are discretized using triangular elements, on which the forces are evaluated. The total force is then divided by the plate area, and the simulation output is compared with the experimental data.

Moreover, two triangular meshes are created to simulate the plates used in the rheometer. The contact between particles and the wall is treated like there is no bond. Hence, a Hertzian contact is solved at the sphere boundaries. The reason for using Hertz at the boundaries is to keep a degree of rigidity and reduce overlap. If we would, for example, fit the parameters of the Generalized Maxwell model for a very soft material by using the same parameters internally and at the boundaries, we would observe very large non-physical overlaps. This could be fixed by tuning the boundary parameters differently, but it would result in 9 additional parameters in our model. This would be sub-optimal. The parameters used for the particles are Young's modulus $E_p = 1$ GPa, Poisson's ratio $\nu_p = 0.5$, with no dissipation and no shear force, as done for the case of the particle-particle compression test, where we already discussed the effect of the Young's Modulus [Pa] (E) at the DEM particle level. In contrast, for the wall, we used Young's modulus of $E_{wall} = 1$ GPa, Poisson's ratio $\nu_{wall} = 0.5$, a Coefficient of Restitution (e) of $cor_{wall} = 0.7$ and Friction coefficient Hertz model (c_f) of $cf_{wall} = 0.25$. All parameters used in the simulation are summarized in Table 3.2. The main reason for choosing Young's modulus is to avoid excessive nonphysical overlap at the boundaries. It is chosen as the value at which no noticeable increase in the global vertical force is observed on a linear compression on the single hydrogel, obtaining the plot of force vs non-dimensional time $\hat{t} = t/t_{sim}$ of Fig 3.9. Considering that the particles at the boundaries are the first to transmit the information internally, they are not "soft" as one would expect, but they

need to be incompressible, frictionless, and very stiff. The bonds will take care of the internal dissipation and compressibility and define the particles' softness. The values for the walls of Young's modulus and Poisson's ratio are chosen so as to reflect the particles at the boundaries, while the friction coefficient and restitution coefficient are taken from the pairing of the hydrogel spheres with the rheometer plates. The stress, which will then be used to obtain the rheological properties of the sphere, is obtained by summation of the forces acting on the plate divided by the diameter of the sphere squared. This is done to maintain consistency with the rheometer measurement. The boundary conditions are applied to the top plate as follows. Considering the sphere's origin in the center of the reference frame, an initial compression of $0.055D$ is performed. The oscillation is then applied with an amplitude $A = 0.05D$, so that contact is maintained during the whole oscillation. This results in an average deformation $\varepsilon = 0.053$, which will then be used to calculate the rheological properties of the simulated hydrogel.

Table 3.2.: Parameters used in the single particle compression oscillation test.

d_p [mm]	D [mm]	N_p	a [mm]	E_p [Pa]	ν_p	E_{wall} [Pa]	ν_{wall}	cor_{wall}	cf_{wall}
0.7	3	903	1	1e9	0.5	1e9	0.5	0.7	0.25

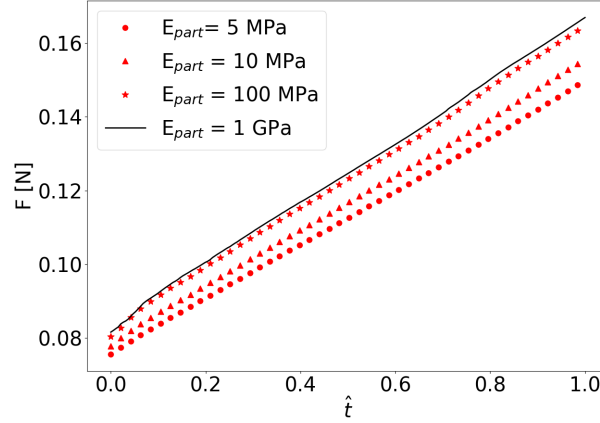


Figure 3.9.: Global vertical force measured during a linear compression of the hydrogel used for the oscillatory testing against non-dimensional time $\hat{t} = t/t_{sim}$, where t_{sim} is the total simulation time. The walls, the discretization, and the viscoelastic parameters are kept constant, and only the Young's modulus of the DEM particles is changed to show that at certain values, no notable increase of global vertical force is observed. The errors of the 5 MPa, 10 MPa, and 100 MPa w.r.t the 1 GPa data are 9.8%, 6.4%, and 1.2%, respectively.

Simulation output and comparison with experiment

The frequency range used to run the frequency sweep is reduced with respect to the experimental data to speed up the process, starting from a minimum frequency of $\omega = 1.04 \text{ rad/s}$. Regardless, the parameters used in the simulations are shown in Tab. 3.1. Before computing the modified storage and loss moduli, the stress response is filtered using a Fast Fourier Transform, such that the secondary eigenfrequencies oscillations are smoothed out [77]. Once the FFT is applied to the stress response signal, the largest amplitude is taken as the stress amplitude of the system, which is also found at the value of the applied frequency.

Furthermore, a dummy function of the form $\sigma = \sigma_0 \sin(\omega t + \varphi)$ is computed to evaluate the phase lag between the stress and the applied strain fitted to the stress response, where σ_0 is the stress amplitude found before. The fit would return φ , hence giving the phase shift in radians. Once amplitude and phase shift are known, it is possible to compute the modified storage and loss moduli as $E' = \sigma_0/\varepsilon_0 \cos \varphi$ and $E'' = \sigma_0/\varepsilon_0 \sin \varphi$, resulting in the plot of Fig. 3.10. It is also noted that E' has a lower error than E'' . This reflects what is observed already during the fitting procedure done in Sec. 3.4.1, where the error on E' is lower than E'' , Fig. 3.7. These differences are then amplified in the simulation due to numerical errors that propagate. It is noteworthy to mention that the model parameters are valid as long as the chosen process has a timescale that falls within the range of frequencies on which the parameters are fitted. Otherwise, a new experimental setup is needed to include the timescale of the given process and a new fitting procedure must be sought to find the new optimal model parameters.

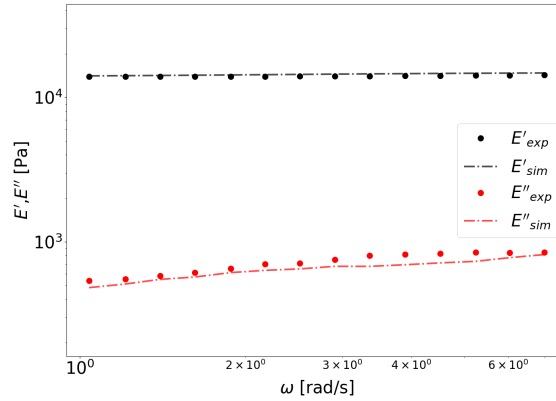


Figure 3.10.: Rheological properties of the hydrogel sphere under cyclic compression, comparison of experimental data and simulation output obtained with parameters of Tab. 3.1. The root mean square error for E' and E'' are 2.9% and 11.3%, respectively.

3.4.4. Validation of the particle-particle compression test

The second experiment to be simulated is the particle-particle compression shown in Sec. 3.3.2. Here, to reduce the number of particles, two half spheres are used, maintaining the same size as the spheres of the experiment. As explained in section Sec. 3.3.2, the spheres do not have a constant diameter, depending on the point at which they are measured. To align with the experiment, the spheres have been created with an average diameter between the ones measured in the vertical and horizontal direction, obtaining $D_{top} = 18.365$ mm for the top sphere and $D_{bot} = 18.275$ mm for the bottom sphere. Once a DEM particle diameter $d_p = 0.5$ mm, is chosen, together with $a = 0.8$ mm, the system of Fig. 3.11 is obtained, resulting in a total number of particles of $N_p = 2361$. All parameters are summarized in Table 3.3. Moreover, while the experiment is performed until a 1.82 mm contact depth is achieved, in the simulation, we stop at a value of 1.2 mm to reduce computational time, considering that when looking at the experimental data, going into higher compressions beyond the value at which we stop the simulations, we observed that the force does not diverge from the relative fitting function, hence it does not add any value to the data in the lower range of compression. In the experiment, the spheres are constrained by (slightly more than) half into the holders. Our simulations modelled this by not considering the constrained half and applying appropriate boundary conditions. A constant motion is forced on the top disk of the upper half-sphere. This means that, regardless of the interaction forces, the particles belonging to this region will keep their velocity constant. Another condition is applied to the bottom disk of the lower half-sphere; the particles belonging to this region are not integrated. Hence, they will have a value of interaction force different from zero but will not move.

Table 3.3.: Parameters used in the particle-particle compression test.

d_p [mm]	D_{top} [mm]	D_{bot} [mm]	N_p	a [mm]	E_p [Pa]	ν_p	v_{comp} [mm/s]
0.5	18.365	18.275	2361	0.8	1e9	0.5	3-1-0.5

Since the Hydrogel sphere is composed of many DEM particles - thanks to the bonds and the lack of Hertzian contact between particles inside the same sphere – it can deform internally following the viscoelastic interaction with the same parameters found in Sec. 3.4.1. At the contact interface between different spheres, a Hertzian elastic non-dissipative force is computed, where there is no friction and no shear forces, the reasons behind these choices are explained.

Regarding dissipation, it can be proven that most energy loss happens internally in the sphere. Two test simulations with a non-dissipative ($e = 1$) and a dissipative Hertzian contact ($e = 0.01$), with e being the coefficient of restitution, resulted in perfectly overlapping functions for the global vertical force on the sphere with a deviation between the dataset of 0.18 %. This means that the contribution to dissipative forces due to interface contact is negligible compared to the contribution of the dissipative forces due to internal deformation.

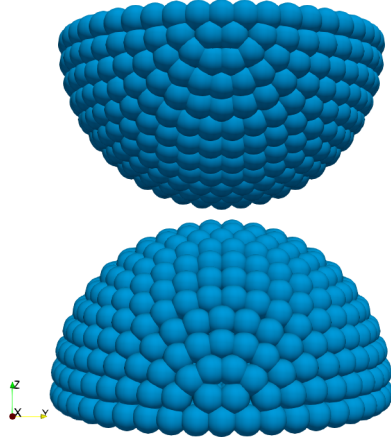


Figure 3.11.: Simulation setup for the particle-particle linear compression test. Two half spheres are discretized. A constant motion is applied on the upper sphere's top disk while the lower sphere's bottom disk is not integrated, resulting in it not displacing. The force is measured on the top disk of the upper sphere as the sum of the forces on each DEM particle.

The friction coefficient of hydrogel spheres is relatively low, with values ranging from 0.001 to 0.02, depending on the composition and the sliding velocity, [78]. Moreover, given the compression direction is aligned with the spheres' centers, the contribution of shear forces at the contact interface to the global vertical force is close to zero. In addition, given the discrete nature of the particles, if we wanted to simulate a shear contact between the particles, we would observe a dissipation force even in the absence of dissipative contact forces in the Hertzian formulation, due to numerical friction [79, 80, 81]. Numerical friction is an issue that is observed when discrete elements are used to describe larger particles. It is observed in multisphere models, SPH, and our bonded model. Numerical friction is observed when there is a relative tangential motion between the larger particles, which produces a “stick and slide” type of motion at the boundaries (like real friction works but on a larger scale). This results in non-physical oscillations in the macroscopic force that alters the simulation output. Unfortunately, such oscillations are still an open problem in DEM, and research has been going on to solve this issue. Moreover, for a reason already explained in Sec. 3.3.1, the Young's Modulus of the DEM particles is chosen to be $E_p = 1$ GPa.

Simulation output and comparison with experiment

The only parameter not in line with experiments is the compression velocity. While in the experiments, the compression speed is $v_{comp} = 0.09$ mm/s, different values have been used in the simulation to address the impact of such a parameter on the output force. Moreover, the choice of higher compression speeds used in the simulation is to

reduce computational time significantly. If we had matched the experimental speed in the simulation, it would have required a not-feasible amount of time to complete these simulations. It must be pointed out that, as we explained in Sec. 3.4.1, when simulating a process or an experiment, to obtain accurate results, we need to use a set of parameters that have been fitted on a range of frequencies that includes the characteristic time of said process or simulation. In this case, the experiment strain rate is 0.002/s, which is not in either the whole or the reduced range of frequencies of the single compression. However, for the reason explained before, the simulations are run at much higher speeds, namely 3 mm/s, 1 mm/s, and 0.5 mm/s. If we compute the average strain rate for all three cases, we would obtain 0.163 Hz, 0.055 Hz and 0.0225 Hz, which are all higher than the minimum frequency of the whole range of 0.0185 Hz. Since the simulations are run with strain rates that fall within the experimental range, the output can be considered to be accurate. The force output is then evaluated against time, directly related to displacement, since the compression velocity is constant. To show the effect of compression velocity on the simulation output, the force is fitted with a function $f = f_{max} \cdot \hat{t}^m$, with f_{max} being the maximum force of the dataset and $\hat{t} = t/t_{max}$ the non-dimensional time. The fitting quality and the raw data are shown in Fig. 3.12 to highlight the quality of both the fitting and the simulation raw data.

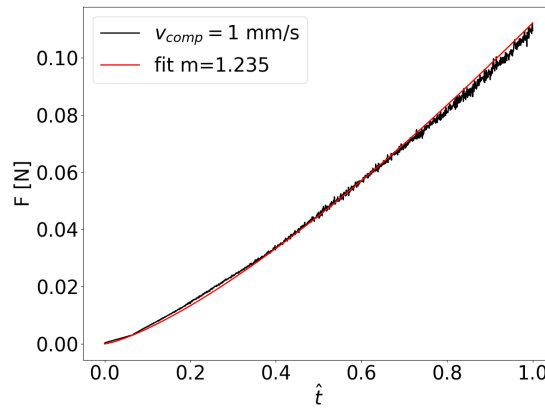


Figure 3.12.: Fitting of the global vertical force for the case with compression velocity $v = 1$ mm/s.

Plotting the fitted force output for the three velocities against the experimental data, we obtain the graph of Fig. 3.14. The main effect of the compression velocity is on the exponent of the fitting function, with a higher value for lower speed. The fitting function aims to highlight the effect of the compression speed, showing us how the hydrogel behavior aligns with its rheological properties. This means faster compression results in higher deformations at the same compression level, since the loss modulus E'' increases at higher frequencies, rendering the hydrogel a bit softer.

Additionally, given the very low timescale of the simulation, it is cause for concern that the dampers would be ineffective, given that they have enough time to relax. Hence, the model would produce an almost purely elastic response. To confirm so, a simulation

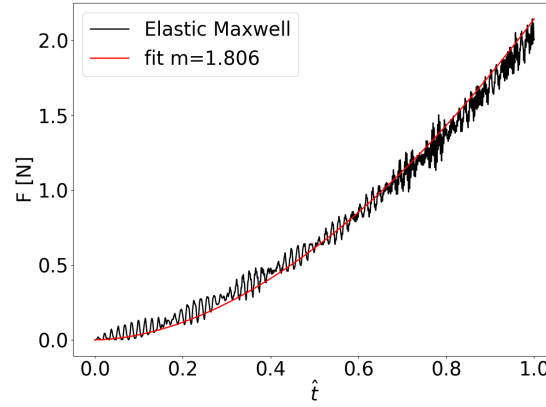


Figure 3.13.: Raw data and relative fitting of the purely elastic simulation for the particle-particle compression. The parameters used are $\mu_i = 1e20$ Pa s, $k_i = k_e = 1e4$ Pa. Notably, the exponent deviates from the experimental data and Hertz contact law. This is because no dissipation is present in the purely elastic case, since dampers are ineffective. The conclusion is that the dampers' effect is significant in the simulations.

is run with a purely elastic relation, obtained by taking the constitutive equation 3.1 and letting $\mu_i \rightarrow \infty$, obtaining $\dot{\varepsilon}_i = \dot{\sigma}_i/k_i$. By setting as initial conditions $\varepsilon_i^0 = \sigma_i^0 = 0$, and integrating the last equation once, we obtain $\sigma_i = k_i \varepsilon_i$. Following this, the simulation of the purely elastic case is run with $\mu_i = 1e20$ Pa s, and $k_i = k_e = 1e4$ Pa. The reason for choosing $k_i = k_e = 1e4$ Pa is that we want to check if the exponent of the fitting function of the global vertical force will change with respect to the case where the dampers are active, so we look into a qualitative match rather than a quantitative one. Finally, plotting the global vertical force of the purely elastic case, 3.13, we note that the fitting exponent is much higher than the one obtained in both the experiment and the damped simulations, concluding that the dampers are active even at much lower strain rates.

Looking again at Fig. 3.14 and comparing the simulated force with the experimental one, we observe how the main difference is in the exponent of the fitting function, which for the experimental data is $m = 1.45$. The reason behind this needs to be investigated further. We speculate that the particle distribution and the nature of the discretization play a role. This statement needs to be supported with data, but that would require a significant amount of work and time, and it goes beyond the scope of this paper, which focuses on calibrating and validating a viscoelastic bonded model for simulating the mechanical properties of hydrogels. Notably, the hydrogels used in particle-particle compression differ in size from those used in single-particle compression. Moreover, the single compression is oscillatory in nature while the particle-particle compression is performed with a constant velocity. However, our data in Fig. 3.14 indicate that bond parameters calibrated in the oscillatory single-particle experiment can be used in particle-particle compression experiments. Unfortunately, a generalization to particle

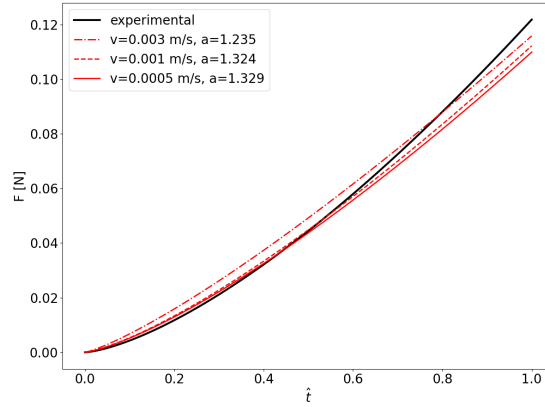


Figure 3.14.: Comparison of the global vertical forces output in the simulation of the particle-particle compression test against experimental data. Three compression velocities are used, showing an increase of the exponent m for the fitting function at decreasing speed. The independent variable used is a non-dimensional time \hat{t}

geometries other than spheres cannot be guaranteed and has not been tested in our current study.

3.5. Conclusions and Outlook

A Bonded Particle DEM model has been implemented, where the constitutive relation between particles follows a Generalized Maxwell equation. This formulation proves robust in describing single-particle deformations that classical DEM could not otherwise capture. This tool has been developed to aid both experimental research and process optimization. Regarding the experiments, once the model is fitted and calibrated with a specific data set, it is possible to use the optimized model to extend the experiment limits, for example, by exciting the material at higher frequencies, applying larger deformations, or running the same tests and gain knowledge at much smaller timescales, that would be impossible to capture due to instruments limitations. For example, one could use the calibrated bonded particle model to make predictions of particle deformation. Such information could be useful for further improving so-called multi-contact DEM models [82, 72], or novel types of contact force models for extremely deformed particles. Additionally, our model can improve on existing mesh-based methods such as FEM. For example, when dealing with flow situations with moving boundaries, using the BPM in such scenarios would greatly simplify the simulation setup (no re-meshing). Also, bond breakage (and reformation or healing) can be easily handled in our bonded particle model, which is highly problematic in FEM-based models. Two experimental setups have been shown, which can be reproduced on hydrogels with different properties to compare their rheological and mechanical properties. Starting from the single particle compression test as a benchmark, we showed that the model could capture the rheological

properties of a given hydrogel and reproduce them with reasonable accuracy, obtaining a relative error of 2.9 % for E' and 11.3 % for E'' . Even though we obtain an average error of 7.1 % , we have room for improvement by adding, for example, an additional Maxwell element. The applied preload strain and the oscillatory strain (maximum 10.8%) might motivate a future improvement of the bond model (e.g., by accounting for non-linearity). However, we could reproduce a non-linear force-displacement relationship upon particle compaction, the same as suggested by Hertz's theory, as shown in Fig. 3.12. Thus, it appears sufficient to consider a linear viscoelastic bond model based on our test with hydrogel spheres. If one changed the hydrogel properties and ran the same test by fitting the new dataset, one could reproduce the rheology of the new hydrogel in the model. This could drastically improve the wide range of applications hydrogels are used for. At the same time, the same parameters fitted using the compression test are used to replicate data from a particle-particle compression test. A good agreement is obtained regarding the global vertical force. Since this force is more related to the compression of the hydrogel spheres, it shows the robustness of the model in capturing compressive forces and its validity in obtaining meaningful data on different setups starting from a benchmark oscillatory test used to calibrate the model parameters. As introduced at the end of Sec. 3.4.4, the simulated force from the particle-particle compression test differs qualitatively from the experimental data. This difference, reflected in the exponent of the fitting function for the global vertical force against time, is intrinsic in the model, but its origin is still unknown. We observed the effect of the compression velocity on the exponent, with an increase at a lower speed, showing a convergence towards the experimental case. However, we believe that other more fundamental elements are responsible for this behavior, and we will investigate this further in the future.

4. Additional work on hydrogels

Given the calibration process shown in the previous section and the relative validation, we observed that it could be interesting how the model behaves in predicting other mechanical properties of the hydrogels. Specifically, we simulated two different tests: one is a free bouncing to measure the coefficient of restitution, while the other is a particle-particle shear test, to check the accuracy in predicting tangential forces as well as normal forces.

4.1. Simulation of coefficient of restitution

For the coefficient of restitution, we use the experimental dataset of Fig. 4.1 [83] as a benchmark to obtain a qualitative prediction. The first remark to highlight is that the coefficient of restitution is not a constant value, but it changes according to the impact velocity of the particle on the surface. This is too complex to be handled by classical DEM, which takes the coefficient of restitution as a constant parameter, properly calibrated. In our work, we want to show that, without using any constant value for the coefficient of restitution but solely the parameters obtained by the calibration of the Generalized Maxwell model, we obtain a similar result for the single hydrogel sphere.

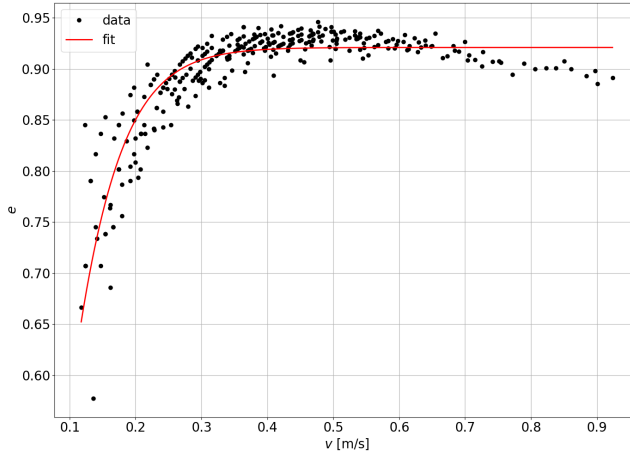


Figure 4.1.: Experimental dataset for the coefficient of restitution of a hydrogel sphere [83]. It is important to mention that the hydrogel used in this experiment is not the same as the one used to calibrate the model parameters. The function used to fit the data is Eq. 4.1, with parameters $A = -0.44$ and $b = -51.67 \text{ s}^2/\text{m}^2$.

To begin with, we fit the experimental data. We do so by using the following fitting function [84],

$$e(v) = e_0(1 + A \cdot e^{bv^2}) \quad (4.1)$$

with A and b constant parameters, while e_0 is the coefficient of restitution computed at the first impact. For the data of Fig. 4.1 we have obtained $A = -0.44$ and $b = -51.67 \text{ s}^2/\text{m}^2$. A discretized hydrogel is formed following the same discretization procedure explained in Chapter 3 to obtain a nice comparison with the experimental data. The hydrogel diameter is chosen to be $D = 4 \text{ mm}$ with a DEM particle diameter of $d_p = 0.25 \text{ mm}$, totaling a number of 517 particles. Additionally, the simulations are run without gravity, and the sphere's initial velocity is set to be $V_0 = 1 \text{ m/s}$, aligned with the z -axis. Two flat plates are inserted at a distance $\Delta = 6 \text{ mm}$, parallel to the xy -plane, Fig. 4.2. Given the lack of information on the chemical composition of the hydrogel used to produce the data of Fig. 4.1, we decided to use the parameters obtained by the calibration of the hydrogel used in Chapter 3. Regarding the simulated hydrogel size, we decided to opt for a smaller hydrogel than the one used in the experiment, similarly as done in the previous chapter, to increase accuracy by using smaller DEM particles whilst maintaining a relatively low number of particles.

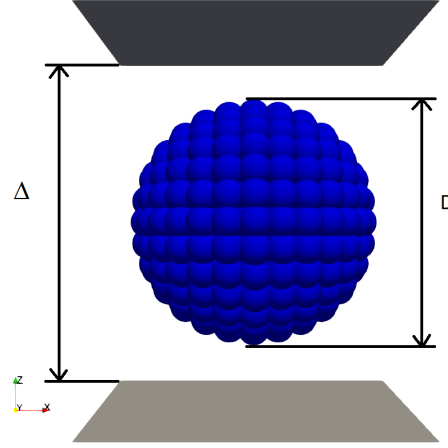


Figure 4.2.: Simulation setup for calculating the coefficient of restitution of hydrogel spheres.

Our goal is to obtain a qualitative match between the simulation and the given dataset so as to show that it is possible, through our bonded model, to obtain an accurate prediction of the internal dissipation that occurs in these viscoelastic spheres under impact. To evaluate the loss of energy, we measure the velocity of the hydrogel before and after the impact by means of the velocity of its center of mass, resulting in the plot of Fig. 4.3. From this data, we do some post-processing to obtain the discrete values of velocities before/after impact, resulting in the black dots, which we will use to

compute the coefficient of restitution. Once the coefficient of restitution is computed, we fit it using Eq. 4.1, which results in the plot of Fig. 4.4. The first thing we can observe is how, qualitatively, we have a good agreement with the experimental data, given the fact that the same fitting function is used for both datasets. However, there is a consistent difference in the parameters used in the fitting function and in the values of the coefficient of restitution. This is due to the fact that the two hydrogels are not the same, both in composition and size, hence the quantitative difference between the two.

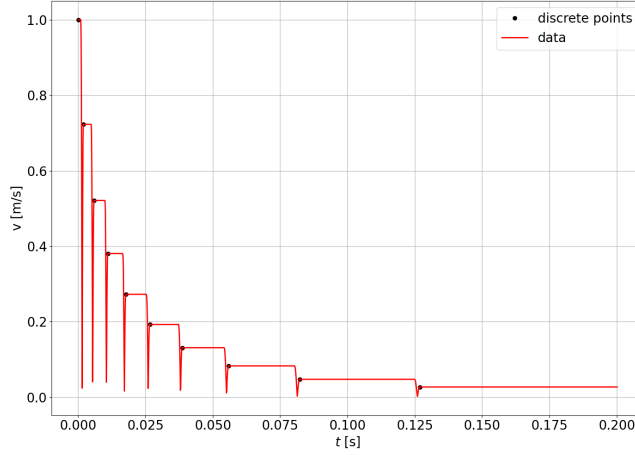


Figure 4.3.: Velocity of the center of mass of the simulated hydrogel. Notice that some post-processing is needed to obtain the values before and after impact, as some relaxation time is observed.

4.2. Low impact velocity simulation

Another simulation is run, this time with a much lower initial hydrogel velocity, to be exact $V_0 = 0.01$ m/s, in order to check if there are substantial differences with respect to the higher speed case. The boundary conditions and the size of the hydrogel sphere, as well as the DEM particles, are the same as in the previous simulation. The same procedure is used to quantify the velocities before and after impact, resulting in the plot of Fig. 4.5.

As in the previous simulation, we use the same fitting function of Eq. 4.1 to fit the coefficient of restitution in function of the velocity, obtaining the plot of Fig. 4.6. Moreover, the parameters found here are $A = 0.05$ and $b = -1.202e5$ s²/m².

The first remark about this result is that the behavior of the coefficient of restitution is exactly the opposite of the higher impact speed case, i.e., we have an increasing e at decreasing impact speed. As a consequence of this, we are not able to accurately predict the data with the same function as in Eq. 4.1. This means that a different equation must be used to fit this data. We try a similar formulation, resulting in

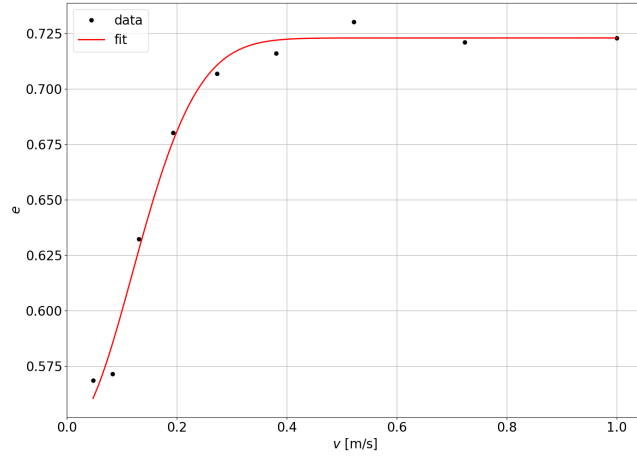


Figure 4.4.: Coefficient of restitution of the simulated hydrogel as a function of the velocity. The function used to fit the data is Eq. 4.1, with parameters $A = -0.24$ and $b = -35.78 \text{ s}^2/\text{m}^2$. It is noted how the same fitting function used for the experimental data works also for the simulated data, proving a qualitative match.

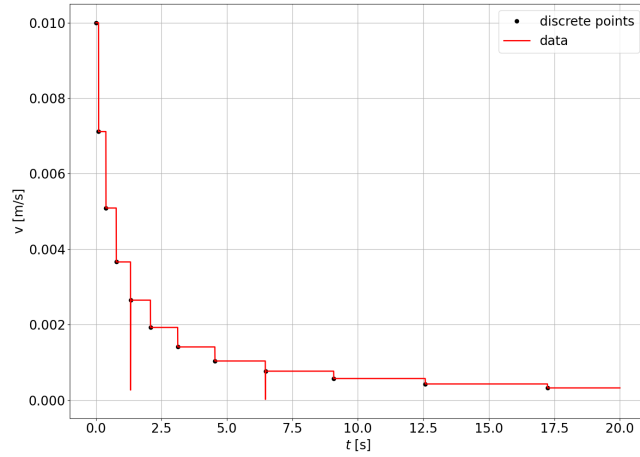


Figure 4.5.: Velocity of the center of mass of the simulated hydrogel with initial velocity $V_0 = 0.01 \text{ m/s}$. The same post-processing is used as in Fig. 4.3 to obtain the values of velocities before and after impact.

$$e(v) = e_0(1 + A \cdot e^{bv}). \quad (4.2)$$

Using this last equation and trying again to fit the data, we obtain the plot of Fig. 4.7, with fitting parameters $A = 0.067$ and $b = -429.17 \text{ s/m}$. This function returns a much better prediction for the low-speed coefficient of restitution. It is important to notice that the e does not only increase at decreasing impact velocity, but its variation

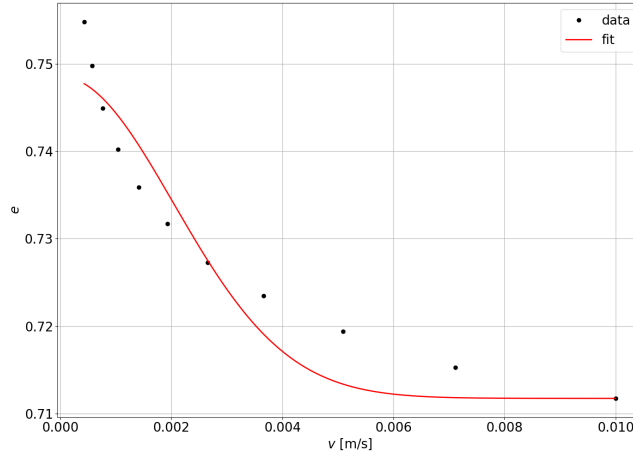


Figure 4.6.: Coefficient of restitution of the simulated hydrogel as a function of the velocity. The function used to fit the data is Eq. 4.1, with parameters $A = 0.05$ and $b = -1.202e5 \text{ s}^2/\text{m}^2$.

is much smaller than the one for the high-speed case. To be specific, in the high-speed case, the change of the value of e relative to the first impact is 21.4 %, while for the low-speed, we obtain a change of just 6 %. This result is very interesting, as it would be very hard to measure the coefficient of restitution at such low-speed hence, here, the model is able to give insights on the mechanical properties of the hydrogel in a limit case for experiments, which is one of the main innovations of the model.

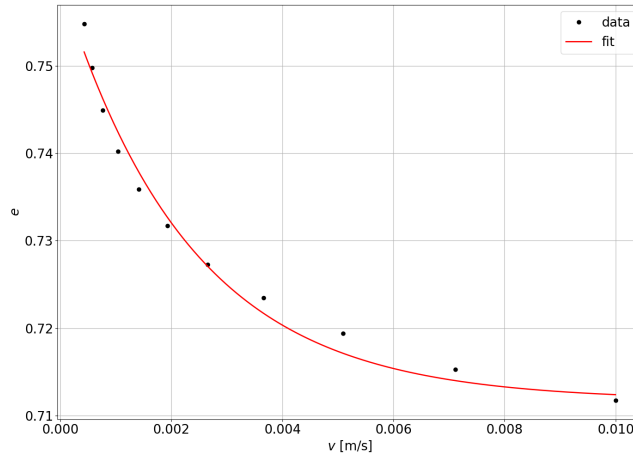


Figure 4.7.: Coefficient of restitution of the simulated hydrogel as a function of the velocity. The function used to fit the data is Eq. 4.2, with parameters $A = 0.067$ and $b = -429.17 \text{ s/m}$.

4.2.1. Prediction of the impact velocity using a variable coefficient of restitution

In the previous section, we showed how the calibrated hydrogel in the simulation behaves in accordance with real-case scenarios when it comes to energy dissipation during impacts. We measured the velocity of the sphere before and after each impact, and we predicted the change of the coefficient of restitution in function of the velocity. For some applications, it might be relevant to predict the velocity change of the hydrogel at each impact, and to do so, we tried to come up with a way of fitting the impact velocities as a function of time, based on a set of hypotheses and definitions, which are:

- The velocity as a function of the coefficient of restitution has the following form:

$$v(e) = V_0 e^{-\frac{D}{e\Delta}} \quad (4.3)$$

- The total path distance covered by the hydrogel is defined as:

$$D = \int v(t) dt \quad (4.4)$$

- The e as a function of velocity follows Eq. 4.1 or 4.2, depending if dealing with a high-speed or a low-speed impact. We are showing the low-speed impact here hence we will use Eq. 4.2 for the e .

Since we want to end up with a relation between velocity and time, we must go through some mathematical passages first. The first step is to rearrange Eq. 4.3 so that we can isolate D and substitute its definition, resulting in

$$e\Delta \ln \frac{v}{V_0} = - \int v(t) dt. \quad (4.5)$$

To remove the integral from the above equation, we derive once with respect to time, resulting in

$$v(t) = -\Delta \left(\frac{de}{dv} \frac{dv}{dt} \ln \frac{v}{V_0} + \frac{e}{v} \frac{dv}{dt} \right). \quad (4.6)$$

By substituting Eq. 4.2 and its derivative into the above equation, we obtain

$$\frac{dv}{dt} = -\frac{v}{\Delta} \left[e_0 A b e^{bv} \ln \frac{v}{V_0} + \frac{e_0(1 + A e^{bv})}{v} \right], \quad (4.7)$$

which can be solved via numerical integration. For this case, the simple Forward Euler's method is used, resulting in a discrete expression for the velocity in the function of time, which is then compared with the simulation output in Fig. 4.8. We can observe how Eq. 4.7 accurately predicts the velocity loss of a bouncing hydrogel. We did the same procedure for the high-speed case, obtaining a similar result. In conclusion, we are

able, with the presented model, to accurately predict the variable coefficient of restitution of a single hydrogel sphere just by calibrating the model parameters, together with the prediction of the velocity loss in function of time. Additionally, we can gain insights into the behavior at lower speeds where the experiments struggle to capture information accurately, hence expanding the knowledge of such materials beyond the experimental limits.

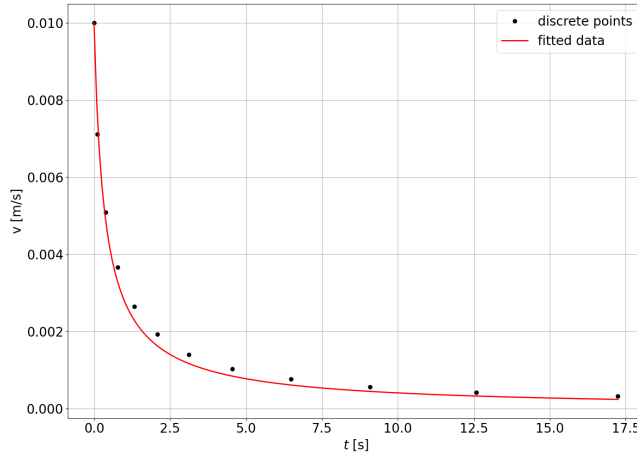


Figure 4.8.: Comparison between the impact velocity obtained from the simulation output and the predicted velocity computed by numerical integration of Eq. 4.7. The good agreement lets us predict the velocity as a function of time in a bouncing hydrogel.

4.3. Hydrogel Particle-particle shear test

Experimental setup and output

Another test that was simulated to obtain a match with experimental data is the particle-particle shear contact test. The setup is similar to the one used to perform the particle-particle normal compression of Chapter 3, with the difference that this time the upper particle does not move vertically but horizontally. In order to ensure contact, the tool is lowered 1 mm at a time and manually rotated to check for contact. Once contact is detected the probe is moved 2 mm up and a measurement system inertia calibration is done. Then, the probe is moved 1mm down and locked at the instrument 0 deflection angle reference position. Moreover, the tool rotates at 0.5 rpm. During this rotation, when a torque of 0.0002 Nm is detected, the rotating arm is forced to stop. If the specified torque level is not detected, the tool will move down 0.1 mm until contact is detected. Once contact is detected, the moment arm will rotate back to a fixed angle [85]. Then, the tool will rotate at 0.008 rpm for 3000 seconds in the clockwise direction. The instrument measures data on the global vertical force, torque, angular displacement from a fixed reference (deflection angle), and the vertical position of the moving probe with respect to the container floor throughout the duration of this protocol. A summary of the above-described procedure setup, together with the output of global vertical and horizontal (computed from the torque) forces is shown in Fig. 4.9.

4.3.1. Simulation setup, output and comparison with experiment

Similarly as done for the simulation of the particle-particle compression in Chapter 3, to reduce the number of particles, two half spheres are used, maintaining the same size as the spheres of the experiment. As explained in section Sec. 3.3.2, the spheres do not have a constant diameter, depending on the point at which they are measured. To align with the experiment, the spheres have been created with the diameter measured along the vertical direction, with $D_1 = 18.16\text{ mm}$ the diameter of the top sphere and $D_2 = 18.79\text{ mm}$ the one of the bottom sphere. The DEM particles are arranged by the same spatial discretization used in Chapter 3, with a particle diameter of $d_p = 0.001\text{ m}$, resulting in the initial configuration of Fig. 4.10.

While the experiment is run at a much lower speed of the top sphere, it has been found that its velocity has a marginal effect on the vertical force, as shown in Fig. 4.11. Hence, the simulations are run with a velocity of the top sphere of $v_{top} = 0.02\text{ m/s}$, to reduce computational time. Moreover, the same boundary conditions of the particle-particle compression test are used.

We start by plotting the vertical force against the experimental output, Fig. 4.12, and immediately notice two things. First, the amplitude of the forces does not match, and there is a high relative error between them. This needs to be addressed by tuning the normal to shear ratio α introduced in Chapter 2, for the model parameters. Given the high computational time needed to run the simulations, proper calibration of this parameter would be too time-consuming, so we run one simulation with a value of $\alpha = 5$, observing a consistent reduction of the force intensity. However, this data is not shown.

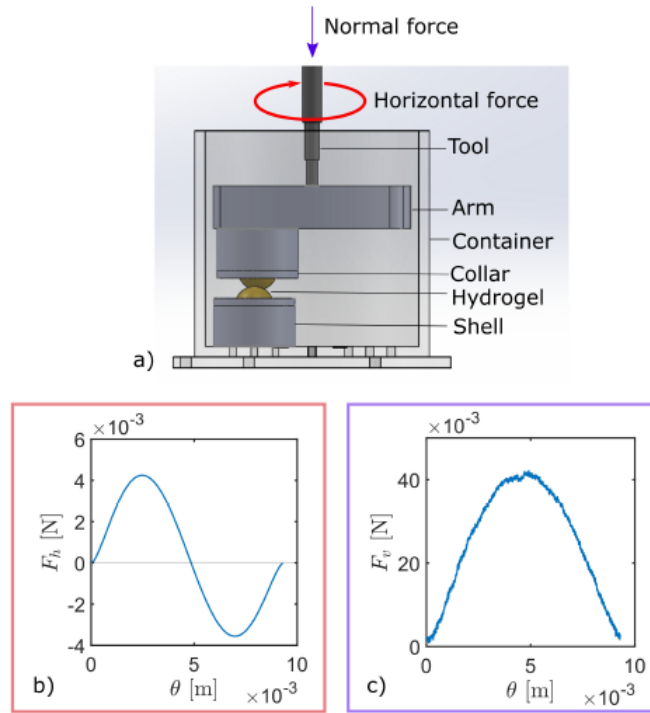


Figure 4.9.: a) Experimental Setup: Inter-particle shear. b) Forces in the horizontal direction vs. displacement in the rotational direction c) Forces in the vertical direction vs. displacement in the rotational direction

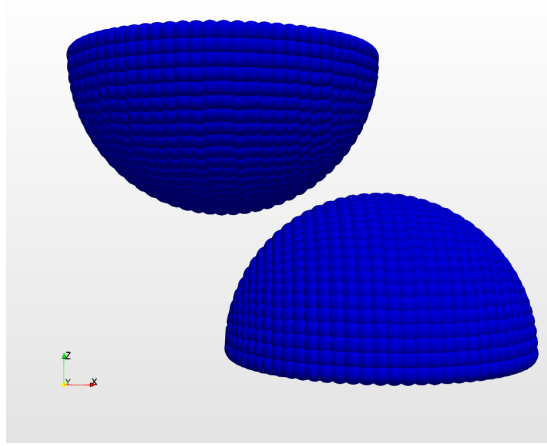


Figure 4.10.: Initial condition for the particle-particle shear simulation. The top half-sphere moves with a constant linear velocity towards the bottom half-sphere, which is maintained in the same position. The force is measured as the total force acting on the particles on the top disc of the top half-sphere.

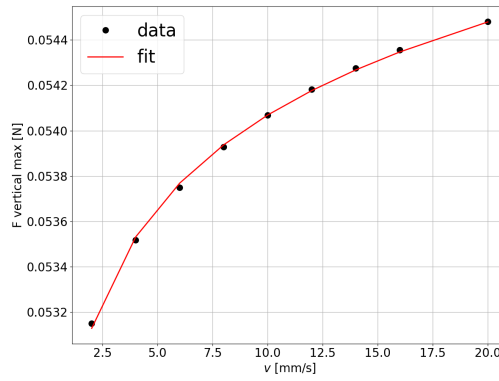


Figure 4.11.: Effect of the velocity of the top hydrogel sphere on the maximum vertical force measured in the simulation. It can be seen how a large change in velocity, from 1.8 to 20 m/s, results in a small change of the maximum vertical force of around 2.5 %. It can be concluded that the speed of the upper sphere does not influence the measured force intensity.

The second thing we notice is the high-frequency oscillations present in the simulation output. This effect is due to numerical friction, which we will investigate further in the next section.

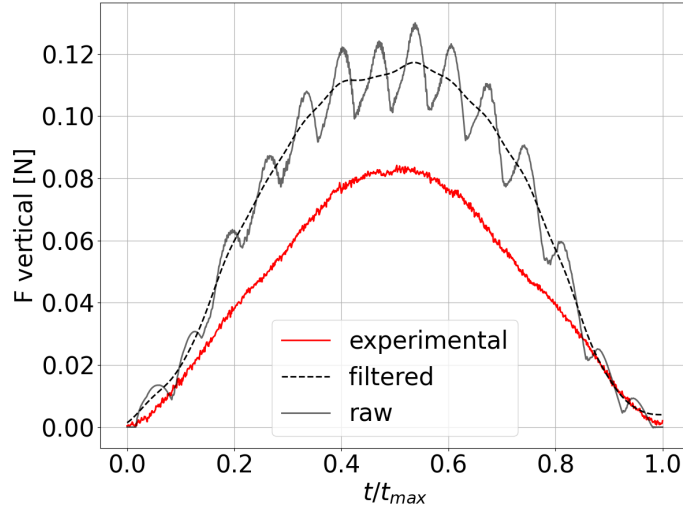


Figure 4.12.: Vertical force output of the particle-particle shear simulation setup. Large oscillations are observed, due to the discrete nature of the hydrogel spheres. The raw data has been filtered with a low-pass filter, which works well for the vertical force due to the lower intensity of the oscillations, when compared to the horizontal force.

4.3.2. Numerical friction

In this section, we show the challenge arising from the output of the horizontal force, where large oscillations due to numerical friction are observed. Fig. 4.13.

Three methods have been used to eliminate the oscillations and get an output comparable to the experimental data. To begin with, a low pass filter is applied, which results in the plot of Fig. 4.14. As it stands, the low pass filter is not a good solution. If, on the one hand, it shows that the data is qualitatively comparable with the experiment, on the other hand, it lacks robustness [86].

The other method used to reduce data noise is to run a series of simulations where the relative angle between the spheres is changed by a constant value. The idea is to obtain a large dataset of not overlapping oscillations that should cancel each other out when a simple averaging is done. To achieve this, the bottom half-sphere is kept in the original orientation. In contrast, the top half-sphere is rotated around its y-axis (the same would be obtained with a rotation around the x-axis due to symmetry) from 0° to 45° , using 9° increments. It is noteworthy to mention the discretization of the hydrogel spheres is coarser with respect to the one used in the Chapter 3. The choice for a coarser discretization is to decrease the computational time since these simulations are done to test the applicability of the average method. Finally, the plot of Fig. 4.15 is obtained. We can observe some potential in this method, although a larger number of simulations might be needed to achieve a better result, rendering this option not feasible due to the large computational cost.

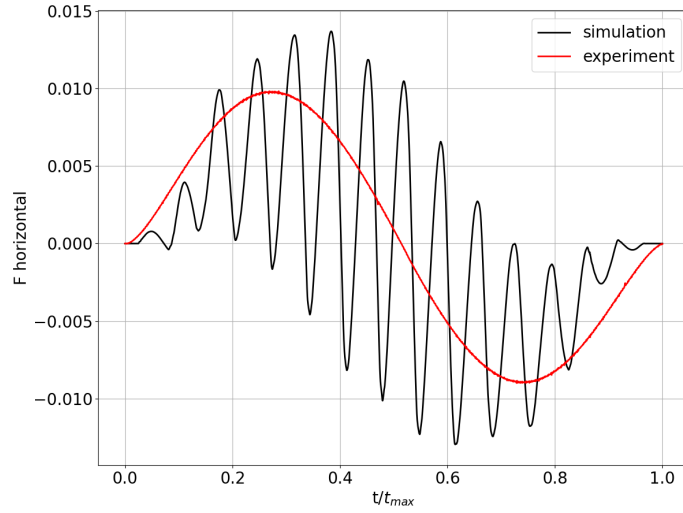


Figure 4.13.: Horizontal force output of the particle-particle shear simulation setup. Large oscillations are observed, due to the discrete nature of the hydrogel spheres. This phenomenon, although present on both the vertical and horizontal force, is more evident on the latter because it has a lower magnitude with respect to the former, which is in line with the experimental data.

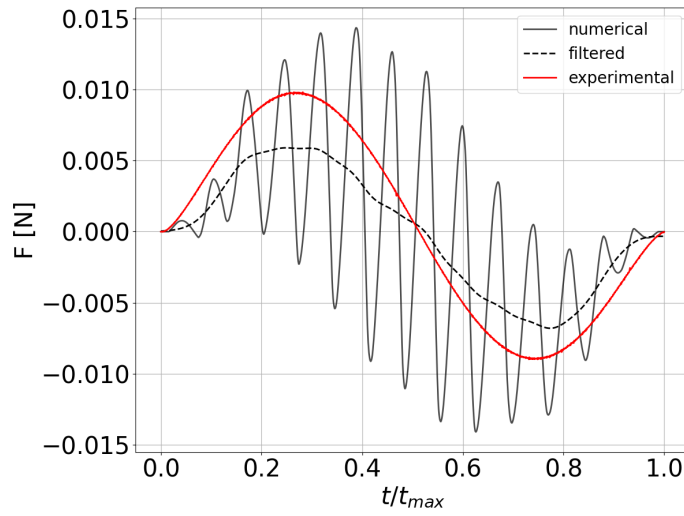


Figure 4.14.: Filtered and raw data for the horizontal force output of the particle-particle shear test. It can be observed how the filtered data is behaving accordingly to the experimental counterpart, even though the noise-to-signal ratio is very large, suggesting another approach is needed to solve the issue.

A third method has been implemented to solve the issue. Here, we tried to solve the problem on a more fundamental level. Knowing that the cause of the oscilla-

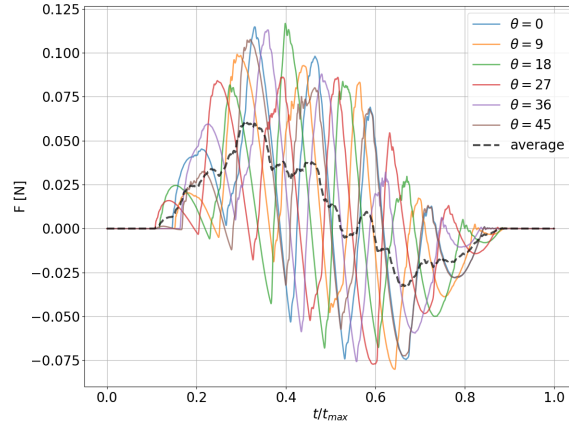


Figure 4.15.: Averaged raw data with different relative contact angles between the top and bottom hydrogel spheres. An improvement is obtained with respect to the raw data, but this method requires a series of simulations to be run, which ultimately increases computational time. Nevertheless, this result proves that the oscillations are purely numerical artifacts and are highly affected by the nature of the discretization.

tions is to be found in the Hertzian part of the contact, and knowing that some DEM particles might have a contact direction not aligned with the main contact direction of the hydrogel spheres they belong to [79], a modification in the algorithm of the Hertzian force computation is implemented. Normally, the Hertzian force is computed as $f_{Hz} = \frac{4}{3}E_{eff}r_{eff}^{1/2}d^{3/2}$, where $E_{eff} = \frac{E}{1-\nu^2}$ is the effective Youngs' Modulus, with E the Youngs' Modulus and ν the Poisson ratio of the DEM particles, r_{eff} is the effective radius, which for mono-disperse systems is $r_p/2$, with r_p being the radius of the particles, and d is the overlap. In the algorithm, f_{Hz} is computed as a scalar and then multiplied with the unit normal vector connecting the centers of the particles in contact, $\hat{n} = \frac{\vec{r}_i - \vec{r}_j}{|\vec{r}_i - \vec{r}_j|}$. In the modified implementation, instead of multiplying the scalar value of the force with the local unit normal vector, it is multiplied with the macro unit normal vector, which connects the centers of the hydrogel spheres [80], $\hat{N} = \frac{\vec{r}_{top} - \vec{r}_{bot}}{|\vec{r}_{top} - \vec{r}_{bot}|}$. The idea behind this is that, at the micro-level, some contacts are not aligned with the main contact direction, hence implementing this simple modification, should eliminate unwanted out-of-plane forces that may cause numerical friction. Contrary to the vertical force, where we had to tune the Young's Modulus to match the experimental data, here we used a value close to the real measured stiffness of the hydrogels, i.e. $Y = 10kPa$, obtaining the plot of Fig. 4.16. The first take from this result is that the experimental data fits the raw data nicely, without increasing the Young's Modulus, which here is chosen as $Y = 10kPa$. If one runs the same simulation with the original projection, one would obtain a much lower force, hence the higher value used in Sec. 3.4.4 for the

vertical force. The second take is that there is still the presence of oscillations, at a much higher frequency but a lower magnitude, except for the three larger peaks, whose nature is still unknown.

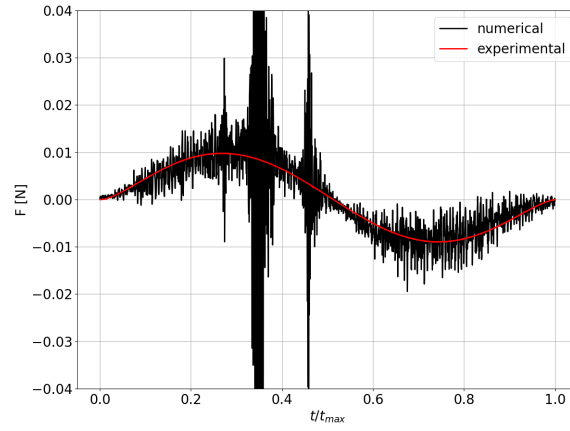


Figure 4.16.: Horizontal force output for the case of normal contact forces projected onto the macro-normal direction instead of the local particle-particle normal direction.

5. Conclusions and outlook

In this chapter, we summarize the main findings of this thesis while addressing the limitations and potential improvements that can be implemented in the future.

5.1. Conclusions from chapter 2

Our research takes a unique approach to viscoelastic materials, a significant component of materials used in industrial processes. We demonstrated the feasibility of a hybrid model that combines a classical DEM approach with bonded particles. This innovative model can handle both discrete and continuous materials, and its bonded contact's constitutive relation can describe a wide range of materials, from purely elastic to purely Newtonian fluids. Given the large number of possible combinations of springs and dampers to define the constitutive relation of the viscoelastic bonds, we used two models that are extensively used in literature and compared their output to assess which one is better suited for use. In order to compare the Burgers and the generalized Maxwell model, we set up a simple test case to simulate oscillatory shear rheometer tests. To do so, we defined a cubic lattice and applied oscillatory motion to the top layer of particles, observing the resulting stress.

The first observation is that the system is a multimode frequency oscillator. The presence of multiple frequencies is due to the presence of multiple elements. No matter what the distribution nor the mass of the particles is, secondary frequencies are always creating instabilities [77]. In our case, we are interested in the frequency connected to the highest amplitude since we need the amplitude and frequency of the response to measure the material's rheological properties. If one took the amplitude of, for example, the second eigenfrequencies, that would result in a significant underestimation of the stress. That is why the stress response is fitted using a single frequency, a decision supported by the fact that the stress amplitude is in line with experimental data. Before simulating the lattice, the model parameters are calibrated by fitting the experimental data analytically, using the constitutive relation of the model. Moreover, we observed that when using the Burgers model to calibrate the parameters on an experimental dataset composed of a wide range of frequencies, it lacked accuracy, hence highlighting the limitation of this model. The generalized Maxwell model has been implemented to overcome this, showing a much more robust fitting quality on the same range of frequencies. The reason behind that is that the generalized Maxwell model has more characteristic times than the Burgers model, rendering it more suitable for general applications. Our model's versatility was further demonstrated when we successfully validated it on a more complex system, a ring oscillatory shear rheometer with a random distribution of particles. This

successful validation on a complex system underscores the model's potential for real-world applications and its ability to accurately simulate a variety of scenarios.

5.2. Conclusions from chapter 3 and chapter 4

Once the model has been validated on a continuous paste, we wanted to investigate its applicability to granular materials, in this case, hydrogel spheres. To do so, we first designed a custom experiment to calibrate the model parameters. Since producing a cubic hydrogel to perform oscillatory shear is very difficult, we opted for oscillatory compressions on the sphere. We followed the same calibration process as for Chapter 2, with the difference that only the generalized Maxwell model was used now. Once the model parameters are obtained, a discretized hydrogel, made by bonded DEM particles, is defined. The experimental setup is recreated as a scaled digital twin to reduce computational time, and the output is compared with experimental data, obtaining 7 % relative error, on average, for the complex moduli. This result brought it one step further by validating the model on a sphere-sphere linear compression test. In the experiment, two hydrogel spheres are in contact and compressed along the normal direction by imposing a constant velocity on one of the spheres and measuring the total force produced in the compression direction. In the simulation, two half spheres are discretized, and the compression velocity is increased to reduce computational time while maintaining the same deformation values. As expected, we observed an effect of the compression velocity on the exponent of the fitting function for the force due to the viscoelastic behavior of the hydrogel, but we obtained a good fit regarding the force magnitude.

In order to further validate and test the model on hydrogel spheres, we replicated two additional experiments. For the first one, we simulated a bouncing hydrogel to measure the effect of impact velocity on the coefficient of restitution. The exact initial velocity of the experiment is used, and after some post-processing and analytical fitting, we obtain a qualitative match with the experimental data. Since we want to highlight the model's innovation to investigate scenarios that are otherwise impossible to observe experimentally, we set up a simulation with a much smaller impact velocity, observing an exciting trend. On the one hand, the coefficient of restitution increased at decreasing velocity, which is the opposite of the behavior observed at higher velocity. On the other hand, the velocity reduction between the first and last impact was around 6 %, while the higher impact speed was around 21 %. These are valuable results, as observing this in an experimental setup would be extremely challenging.

5.3. Model limitations and outlook

The model presented in this thesis could correctly predict viscoelastic materials' rheological and mechanical properties. From the paste-like behavior of the materials in Chapter 2 to the hydrogel spheres of Chapters 3 and 4, the model consistently matched experimental data with good accuracy. However, the model is imperfect, and some limitations will be highlighted here, as well as future improvements.

To begin with, a high computational time was observed in every case because many contacts need to be solved at each timestep due to the presence of the bonds. This means that, concerning the classical DEM simulations, where particles are in contact for a limited number of time steps, bonded particles are in contact for the whole simulation duration, hence increasing the computational time. One way to overcome this is to allow bonds to break. The current model has this feature implemented, although it has yet to be chosen not to activate it. This choice is because the breakage conditions add additional parameters to the model, which need to be calibrated with more tests, such as fracture or tensile tests, that were not available for the type of material simulated. Hence, it would be an interesting future application to be able to correctly predict the fracture of viscoelastic materials with our model.

Another interesting point is the use of mono-dispersed systems rather than poly-dispersed ones. Again, the choice of mono-dispersed systems is driven by the need to reduce computational time since a poly-dispersed system would account for more bonds. A crucial future improvement of the model would be then to increase its efficiency and computational cost to allow for finer simulations and larger systems behavior, which would be of interest to the industrial applications involving such materials.

Last, the numerical friction encountered in Chapter 4 is a significant limitation, standard in SPH and multi-sphere simulations when boundaries are in contact. This effect limits the model's applicability to more general applications and must be the main focus for future work looking at improving the current model. The solutions shown in this thesis might be used as a starting point of reflection, but different approaches were not investigated for lack of time. It would be highly beneficial to this work and the whole particles-based simulations community to find a solution to this fundamental problem.

A. Validation of the bonded generalized Maxwell model

The simulation is defined to resemble the single particle compression-extension experiment under dry conditions as accurately as possible, where the limiting factor is the number of particles used to discretize the hydrogel sphere. In general, the higher the number of particles, the higher the computational cost of the simulation, but the better accuracy is achieved and vice-versa. Some models try to apply a so-called "coarse-graining", which aims to reduce the number of particles in the simulation without losing the information a larger system gives. Similarly, in this case, we want to check the effect of particle size on the variables computed in the simulation. A simple test case is defined, and its output is compared with analytical values. The test case is an oscillatory compression-extension motion similar to the one used in the cyclic compression experiment but applied to a cube this time. The cube is formed by a Face Centered Cube lattice, as shown in Fig. A.1.

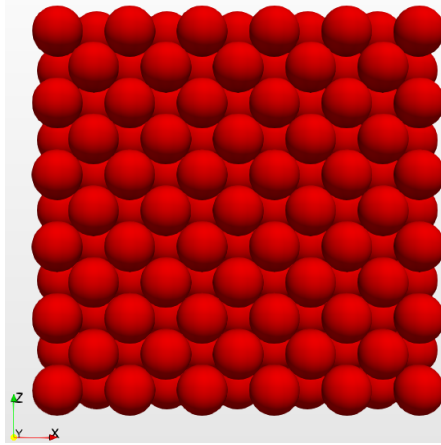


Figure A.1.: Geometrical representation of the FCC lattice cube used for the convergence study and validation of the model.

Three different particle sizes are used to study the effect on the output. The size is computed such that the total volume of the cube is kept constant according to the number of particles on one side of the cube. The particles aligned vertically have a distance of $\delta l = 1.001 \cdot \sqrt{2} \cdot d$ between each other, accounting for a total length of the cube side of $L = \delta l \cdot (N - 1) + d = 0.005$ m, with N being the number of particles on the side of the cube and d being the diameter of the particles. It is straightforward to conclude that, given the fixed length of the cube and, hence, the volume, the relative

diameter of the DEM particles can be calculated by changing the number of particles. If one blindly computed the system's stress response and compared it to the analytical solution, one would obtain a great difference in magnitude. This is because the lattice configuration used here, together with the direction of the deformation, would produce both normal and shear force components that are not aligned with the deformation, which means that the shear component of the force must be reduced using the ratio introduced in Sec. 3.2.2 between the normal and shear parameters.

To determine the optimal parameter α , the classical approach used in determining DEM simulation parameters is used, which consists of simulating with a first guess parameter, evaluating the macro-properties to compare with analytical or experimental solutions, computing a residual and repeating the loop until the residual is minimized. The latter is a well-known and established method to calibrate parameters in a model. However, it lacks generality as it is usually optimized for specific applications, and the procedure must be repeated each time something in the original setup is changed. The cost function used in this case is similar to the one used in Eq. 3.9, with the difference that now we do not have a frequency sweep but only one frequency, and instead of comparing storage and loss modulus, we are comparing the amplitude and the phase shift of the stress response, since those are the quantities that we want to minimize the difference of, giving

$$f_{cost} = \left(\frac{\sigma_{0,an} - \sigma_{0,sim}}{\sigma_{0,an}} \right)^2 + \left(\frac{\varphi_{an} - \varphi_{sim}}{\varphi_{an}} \right)^2, \quad (\text{A.1})$$

where the analytical solution, in this case, is known as [17]

$$\sigma(t) = \sum_j^4 \frac{k_j \gamma_0 \omega \tau_j}{1 + (\omega \tau)^2} (\omega \tau_j \sin \omega t + \cos \omega t). \quad (\text{A.2})$$

The stress in the DEM simulation is computed as the average force on the top layer of particles of the cube, divided by the face area

$$\sigma_{sim}(t) = \frac{1}{L^2} \sum_i^{N_{top}} f_i(t). \quad (\text{A.3})$$

with N_{top} being the number of particles on the top layer of the cube. Once the stresses are known, the analytical and the simulated phase lags are computed by fitting the relative stresses with a function of the form $y = A \sin(\omega t + \varphi)$.

To begin with, the smallest particle size is chosen to perform the calibration, which returns a value of $\alpha = 9.1$. This parameter is then used with the three different particles' sizes to produce the plot of Fig. A.2, which is a zoomed-in version of the total stress response, to observe better the effect of the particles' size on the amplitude and the phase of the stress signal. It is clear how the particle size does not affect the accuracy too much since the error is below 3% for all sizes. In detail, no effect is observed on the phase shift error χ_φ , as observed in the inset graph of Fig. A.2, with a relative error that is almost constant and below 2%. A more significant effect is observed for the amplitude error χ_σ .

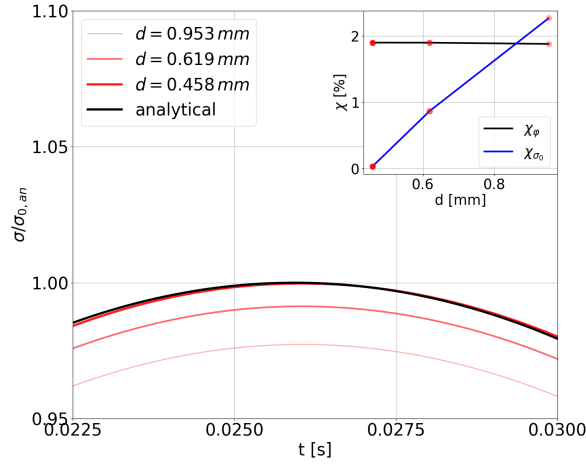


Figure A.2.: Zoomed particular of the stress response of the FCC lattice cube under cyclic compression, when using the parameters of Tab. 3.1, with relative errors for phase and amplitude showing on the inset graph. All errors are measured against the analytical solution given by Eq. A.2, resulting in values well below 3%, making the model valid for predicting the stress response in oscillatory deformation, regardless of particle size. To note the relative errors for both phase shift and amplitude in the inset graph. Stress is normalized with respect to the amplitude of the analytical stress $\sigma_{0,an}$.

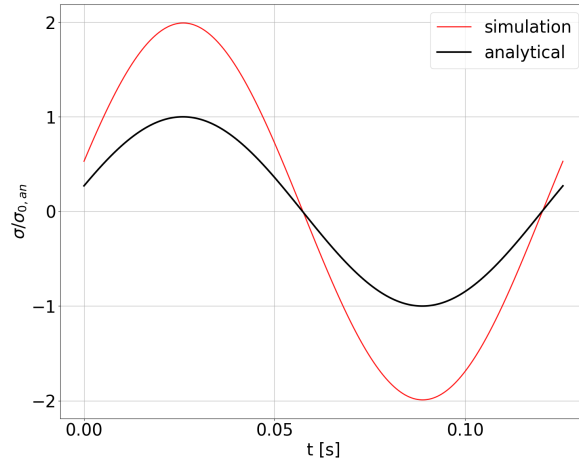


Figure A.3.: Stress response of the BCC lattice for the same parameters of the FCC case. Here, the value of α found for the FCC lattice can not be used, showing how this parameter needs to be optimized for each specific system when changing either the lattice configuration and/or the particle size.

To check the generality of α , when using a body-centered cube lattice to compute the stress response of the same volume, the plot of Fig. A.3 is obtained, where the particle size used is computed according to $d = \frac{L}{(N-1) * 1.001 + 1}$, giving $d = 5 \cdot 10^{-4}$ m for $N=10$. In general, scaling the shear parameters with respect to the normal ones has a visible effect on the predicted stress and is highly dependent on the lattice configuration.

B. Post processing and modelling codes

This GitHub repository contains some of the codes used to create the BPM model as well as the calibration and post-processing routines used in the thesis: https://github.com/mikemask/Codes_public.

The following link contains a GitHub repository with the modified files to implement the BPM model with Generalized maxwell relation into LIGGGHTS: https://github.com/mikemask/liggghts_visco.

Bibliography

- [1] J.L. Favero et al. “Viscoelastic flow analysis using the software OpenFOAM and differential constitutive equations”. In: *Journal of Non-Newtonian Fluid Mechanics* 165 (2010), pp. 1625–1636. ISSN: 0377-0257. DOI: 10.1016/j.jnnfm.2010.08.010. URL: <https://dx.doi.org/10.1016/j.jnnfm.2010.08.010>.
- [2] Wan-Chi Tsai and Gregory H. Miller. “Numerical simulations of viscoelastic flow in complex geometries using a multi-mode Giesekus model”. In: *Journal of Non-Newtonian Fluid Mechanics* 210 (2014), pp. 29–40. ISSN: 0377-0257. DOI: 10.1016/j.jnnfm.2014.05.002. URL: <https://dx.doi.org/10.1016/j.jnnfm.2014.05.002>.
- [3] Marina Bottoni, Claudio Mazzotti, and Marco Savoia. “A finite element model for linear viscoelastic behaviour of pultruded thin-walled beams under general loadings”. In: *International Journal of Solids and Structures* (2008). DOI: 10.1016/j.ijsolstr.2007.08.028.
- [4] Mostafa Katouzian, Sorin Vlase, and Maria Luminita Scutaru. “Finite Element Method-Based Simulation Creep Behavior of Viscoelastic Carbon-Fiber Composite”. In: *Polymers* (2021). DOI: 10.3390/polym13071017.
- [5] D.O. Potyondy and P.A. Cundall. “A bonded-particle model for rock”. In: *International Journal of Rock Mechanics and Mining Sciences* (2004). DOI: 10.1016/j.ijrmms.2004.09.011.
- [6] Wei Cao. “General fractional models for linear viscoelastic characterization of asphalt cements”. In: *Journal of Rheology* 64 (2020), pp. 1439–1453. ISSN: 0148-6055, 1520-8516. DOI: 10.1122/8.0000096. URL: <https://dx.doi.org/10.1122/8.0000096>.
- [7] M. A. P. Mohammed et al. “Mechanical characterization and micromechanical modeling of bread dough”. In: *Journal of Rheology* 57 (2013), pp. 249–272. ISSN: 0148-6055, 1520-8516. DOI: 10.1122/1.4768463. URL: <https://dx.doi.org/10.1122/1.4768463>.
- [8] E. P. Chang and Daniel Holguin. “Electrooptical Light-Management Material: Low-Refractive-Index Hydrogels”. In: *The Journal of Adhesion* 83 (2007), pp. 15–26. ISSN: 0021-8464, 1545-5823. DOI: 10.1080/00218460601102803. URL: <https://dx.doi.org/10.1080/00218460601102803>.
- [9] Yali Li, K.G. Neoh, and E.T. Kang. “Poly(vinyl alcohol) hydrogel fixation on poly(ethylene terephthalate) surface for biomedical application”. In: *Polymer* 45 (2004), pp. 8779–8789. ISSN: 0032-3861. DOI: 10.1016/j.polymer.2004.10.077. URL: <https://dx.doi.org/10.1016/j.polymer.2004.10.077>.

- [10] Mingcui Zhai et al. “Keratin-chitosan/n-ZnO nanocomposite hydrogel for antimicrobial treatment of burn wound healing: Characterization and biomedical application”. In: *Journal of Photochemistry and Photobiology B: Biology* 180 (2018), pp. 253–258. ISSN: 1011-1344. DOI: 10.1016/j.jphotobiol.2018.02.018. URL: <https://dx.doi.org/10.1016/j.jphotobiol.2018.02.018>.
- [11] Yi Deng et al. “Dual Physically Cross-Linked κ -Carrageenan-Based Double Network Hydrogels with Superior Self-Healing Performance for Biomedical Application”. In: *ACS Book Mater. Interfaces* 10 (2018), 37544–37554. DOI: 10.1021/acsami.8b15385. URL: <https://pubs.acs.org/doi/10.1021/acsami.8b15385>.
- [12] E. Susilowati, Maryani, and Ashadi. “Green synthesis of silver-chitosan nanocomposite and their application as antibacterial material”. In: *Journal of Physics: Conference Series* 1153 (2019), p. 012135. ISSN: 1742-6588, 1742-6596. DOI: 10.1088/1742-6596/1153/1/012135. URL: <https://dx.doi.org/10.1088/1742-6596/1153/1/012135>.
- [13] Anubhuti Bhatnagar et al. “Hydrogels: A Boon for Increasing Agricultural Productivity in Water-Stressed Environment”. In: *Current Science* 111 (2016), p. 1773. ISSN: 0011-3891. DOI: 10.18520/cs/v111/i11/1773-1779. URL: <https://dx.doi.org/10.18520/cs/v111/i11/1773-1779>.
- [14] Dong Wang et al. “The structural, vibrational, and mechanical properties of jammed packings of deformable particles in three dimensions”. In: *Soft Matter* 17 (2021), pp. 9901–9915. ISSN: 1744-683X, 1744-6848. DOI: 10.1039/d1sm01228b. URL: <https://dx.doi.org/10.1039/d1sm01228b>.
- [15] Wei-Ming Lu et al. “Compression of deformable gel particles”. In: *Powder Technology* 116 (2001), pp. 1–12. ISSN: 0032-5910. DOI: 10.1016/S0032-5910(00)00357-0. URL: [https://dx.doi.org/10.1016/S0032-5910\(00\)00357-0](https://dx.doi.org/10.1016/S0032-5910(00)00357-0).
- [16] Isaac Newton. “Philosophiae naturalis principia mathematica”. In: (1687). DOI: 10.5479/sil.52126.39088015628399.
- [17] Natalie Rudolph and Tim Osswald. *Polymer Rheology*. Carl Hanser Verlag GmbH & Co. KG, 2015. DOI: 10.1007/978-1-56990-523-4.
- [18] James Clerk Maxwell. “On the Dynamic Theory of Gases”. In: *Royal Society* (1867).
- [19] Alexander Rock et al. “On the Role of Polymer Viscoelasticity in Enhanced Oil Recovery: Extensive Laboratory Data and Review”. In: *Polymers* 12.10 (2020), p. 2276. DOI: 10.3390/polym12102276. URL: <https://doi.org/10.3390/polym12102276>.
- [20] Fan Liu et al. “Experimental and modeling study of the viscoelastic-viscoplastic deformation behavior of amorphous polymers over a wide temperature range”. In: *Mechanics of Materials* 167 (2022), p. 104246. ISSN: 0167-6636. DOI: 10.1016/j.mechmat.2022.104246. URL: <https://dx.doi.org/10.1016/j.mechmat.2022.104246>.

- [21] C. P. Lowe. “Simulating the long-time viscoelastic response of long polymers”. In: *AIP Conference Proceedings*. AIP, 2004. DOI: 10.1063/1.1764125. URL: <https://doi.org/10.1063%2F1.1764125>.
- [22] Dengwu Jiao and Geert De Schutter. “Insights into the viscoelastic properties of cement paste based on SAOS technique”. In: *Construction and Building Materials* 357 (2022), p. 129320. DOI: 10.1016/j.conbuildmat.2022.129320. URL: <https://doi.org/10.1016%2Fj.conbuildmat.2022.129320>.
- [23] Romano Lapasin et al. “Viscoelastic properties of solder pastes”. In: *Journal of Electronic Materials* 27.3 (1998), pp. 138–148. DOI: 10.1007/s11664-998-0204-2. URL: <https://doi.org/10.1007%2Fs11664-998-0204-2>.
- [24] Shuxin Huang. “Viscoelastic Characterization of Corn Starch Paste: (I) The First Normal Stress Difference of a Cross-Linked Waxy Corn Starch Paste with Sucrose”. In: *Bioengineering* 9.9 (2022), p. 465. DOI: 10.3390/bioengineering9090465. URL: <https://doi.org/10.3390%2Fbioengineering9090465>.
- [25] Roberta Massaro et al. “Viscoelastic cluster densification in sheared colloidal gels”. In: *Soft Matter* 16.10 (2020), pp. 2437–2447. DOI: 10.1039/c9sm02368b. URL: <https://doi.org/10.1039%2Fc9sm02368b>.
- [26] C. J. Rueb and C. F. Zukoski. “Viscoelastic properties of colloidal gels”. In: *Journal of Rheology* 41.2 (1997), pp. 197–218. DOI: 10.1122/1.550812. URL: <https://doi.org/10.1122%2F1.550812>.
- [27] J. F. Palierne. “Linear rheology of viscoelastic emulsions with interfacial tension”. In: *Rheologica Acta* 29.3 (1990), pp. 204–214. DOI: 10.1007/bf01331356. URL: <https://doi.org/10.1007%2Fbf01331356>.
- [28] Tharwat Tadros. “Viscoelastic properties of sterically stabilised emulsions and their stability”. In: *Advances in Colloid and Interface Science* 222 (2015), pp. 692–708. DOI: 10.1016/j.cis.2015.03.001. URL: <https://doi.org/10.1016%2Fj.cis.2015.03.001>.
- [29] Rok Kocen et al. “Viscoelastic behaviour of hydrogel-based composites for tissue engineering under mechanical load”. In: *Biomedical Materials* (2017). DOI: 10.1088/1748-605x/aa5b00.
- [30] Ludovica Cacopardo et al. “Engineering hydrogel viscoelasticity”. In: *Journal of the Mechanical Behavior of Biomedical Materials* (2019). DOI: 10.1016/j.jmbbm.2018.09.031.
- [31] George B. Thurston and Alfred Martin. “Rheology of Pharmaceutical Systems: Oscillatory and Steady Shear of Non-Newtonian Viscoelastic Liquids”. In: *Journal of Pharmaceutical Sciences* (1978). DOI: 10.1002/jps.2600671103.
- [32] Alec Otto Cookman, Michael J. Farrar, and Jean-Pascal Planche. “Nonlinear oscillatory shear tests applied to bitumen: analysis and application of large amplitude oscillatory shear (LAOS)”. In: *Proceedings of 6th Eurasphalt I& Eurobitume Congress* (2016). DOI: 10.14311/ee.2016.189.

- [33] J.L. Hess and A.M.O. Smith. “Calculation of potential flow about arbitrary bodies”. In: *Progress in Aerospace Sciences* (1967). DOI: 10.1016/0376-0421(67)90003-6.
- [34] H. Giesekus. “A simple constitutive equation for polymer fluids based on the concept of deformation-dependent tensorial mobility”. In: *Journal of Non-Newtonian Fluid Mechanics* 11.1-2 (1982), pp. 69–109. DOI: 10.1016/0377-0257(82)85016-7. URL: <https://doi.org/10.1016%2F0377-0257%2882%2985016-7>.
- [35] Wan-Chi Tsai and Gregory H. Miller. “Numerical simulations of viscoelastic flow in complex geometries using a multi-mode Giesekus model”. In: *Journal of Non-Newtonian Fluid Mechanics* (2014). DOI: 10.1016/j.jnnfm.2014.05.002.
- [36] F. Pimenta and M.A. Alves. “Stabilization of an open-source finite-volume solver for viscoelastic fluid flows”. In: *Journal of Non-Newtonian Fluid Mechanics* (2017). DOI: 10.1016/j.jnnfm.2016.12.002.
- [37] J.L. Favero et al. “Viscoelastic flow analysis using the software OpenFOAM and differential constitutive equations”. In: *Journal of Non-Newtonian Fluid Mechanics* (2010). DOI: 10.1016/j.jnnfm.2010.08.010.
- [38] Robert Eymard, Thierry Gallouët, and Raphaële Herbin. “Finite volume methods”. In: *Handbook of Numerical Analysis, Solution of Equation in R^n (Part 3), Techniques of Scientific Computing (Part 3)* (2000). DOI: 10.1016/s1570-8659(00)07005-8.
- [39] Pablo A. Prieto-Muñoz, Huiming M. Yin, and Rene B. Testa. “Mechanics of an Adhesive Anchor System Subjected to a Pullout Load. II: Viscoelastic Analysis”. In: *Journal of Structural Engineering* (2014). DOI: 10.1061/(asce)st.1943-541x.0000822.
- [40] P. A. Cundall and O. D. L. Strack. “A discrete numerical model for granular assemblies”. In: *Géotechnique* (1979). DOI: 10.1680/geot.1979.29.1.47.
- [41] Corné J. Coetzee and Otto C. Scheffler. “Review: The Calibration of DEM Parameters for the Bulk Modelling of Cohesive Materials”. In: *Processes* (2022). DOI: 10.3390/pr11010005.
- [42] Stefan Luding. “Cohesive, frictional powders: contact models for tension”. In: *Granular Matter* (2008). DOI: 10.1007/s10035-008-0099-x.
- [43] Tijan Mede et al. “A medial axis based method for irregular grain shape representation in DEM simulations”. In: *Granular Matter* (2018). DOI: 10.1007/s10035-017-0785-7.
- [44] Nazanin Ghods et al. “Discrete element modeling of strongly deformed particles in dense shear flows”. In: *Powder Technology* (2022). DOI: 10.1016/j.powtec.2022.117288.

- [45] Tuo Wang et al. “A review of methods, applications and limitations for incorporating fluid flow in the discrete element method”. In: *Journal of Rock Mechanics and Geotechnical Engineering* 14 (2022), pp. 1005–1024. ISSN: 1674-7755. DOI: 10.1016/j.jrmge.2021.10.015. URL: <https://dx.doi.org/10.1016/j.jrmge.2021.10.015>.
- [46] Christian Ergenzinger, Robert Seifried, and Peter Eberhard. “A discrete element model to describe failure of strong rock in uniaxial compression”. In: *Granular Matter* 13 (2010), pp. 341–364. ISSN: 1434-5021, 1434-7636. DOI: 10.1007/s10035-010-0230-7. URL: <https://dx.doi.org/10.1007/s10035-010-0230-7>.
- [47] Agnieszka Herman. “Discrete-Element bonded-particle Sea Ice model DESIgn, version 1.3a – model description and implementation”. In: *Geoscientific Model Development* 9 (2016), pp. 1219–1241. ISSN: 1991-9603. DOI: 10.5194/gmd-9-1219-2016. URL: <https://dx.doi.org/10.5194/gmd-9-1219-2016>.
- [48] Martin Obermayr et al. “A bonded-particle model for cemented sand”. In: *Computers and Geotechnics* 49 (2013), pp. 299–313. ISSN: 0266-352X. DOI: 10.1016/j.compgeo.2012.09.001. URL: <https://dx.doi.org/10.1016/j.compgeo.2012.09.001>.
- [49] Alexandr Zubov et al. “Numerical Modeling of Viscoelasticity in Particle Suspensions Using the Discrete Element Method”. In: *Langmuir* 35 (2019), pp. 12754–12764. ISSN: 0743-7463, 1520-5827. DOI: 10.1021/acs.langmuir.9b01107. URL: <https://dx.doi.org/10.1021/acs.langmuir.9b01107>.
- [50] Eric Gbadam and Samuel Frimpong. “Micromechanical and microstructural DEM modeling of the viscoelastic behavior of oil sands”. In: *Advanced Material Science* 2 (2017), Not available. ISSN: 2398-6883. DOI: 10.15761/ams.1000116. URL: <https://dx.doi.org/10.15761/ams.1000116>.
- [51] Behzad Majidi et al. “Discrete Element Method Modeling of the Rheological Properties of Coke/Pitch Mixtures”. In: *Materials* 9 (2016), p. 334. ISSN: 1996-1944. DOI: 10.3390/ma9050334. URL: <https://dx.doi.org/10.3390/ma9050334>.
- [52] G. Dondi et al. “Modeling the DSR complex shear modulus of asphalt binder using 3D discrete element approach”. In: *Construction and Building Materials* 54 (2014), pp. 236–246. ISSN: 0950-0618. DOI: 10.1016/j.conbuildmat.2013.12.005. URL: <https://dx.doi.org/10.1016/j.conbuildmat.2013.12.005>.
- [53] E. K. Gbadam. “Characterization and Numerical Simulation of the Microstructural and Micromechanical Viscoelastic Behavior of Oil Sands Using the Discrete Element Method”. Ph.D. thesis. Missouri University of Science and Technology, 2017.
- [54] Jiaolong Ren and Lu Sun. “Generalized Maxwell Viscoelastic Contact Model-Based Discrete Element Method for Characterizing Low-Temperature Properties of Asphalt Concrete”. In: *Journal of Materials in Civil Engineering* 28 (2016). ISSN: 0899-1561, 1943-5533. DOI: 10.1061/(asce)mt.1943-5533.0001390. URL: [https://dx.doi.org/10.1061/\(asce\)mt.1943-5533.0001390](https://dx.doi.org/10.1061/(asce)mt.1943-5533.0001390).

- [55] Yucang Wang and Fernando Alonso-Marroquin. “A finite deformation method for discrete modeling: particle rotation and parameter calibration”. In: *Granular Matter* 11 (2009), pp. 331–343. ISSN: 1434-5021, 1434-7636. DOI: 10.1007/s10035-009-0146-2. URL: <https://dx.doi.org/10.1007/s10035-009-0146-2>.
- [56] Ozlem Caglar Duvarci, Gamze Yazar, and Jozef L. Kokini. “The SAOS, MAOS and LAOS behavior of a concentrated suspension of tomato paste and its prediction using the Bird-Carreau (SAOS) and Giesekus models (MAOS-LAOS)”. In: *Journal of Food Engineering* 208 (2017), pp. 77–88. DOI: 10.1016/j.jfoodeng.2017.02.027. URL: <https://doi.org/10.1016/j.jfoodeng.2017.02.027>.
- [57] W. Cai, G.R. McDowell, and G.D. Airey. “Discrete element visco-elastic modelling of a realistic graded asphalt mixture”. In: *Soils and Foundations* 54 (2014), pp. 12–22. ISSN: 0038-0806. DOI: 10.1016/j.sandf.2013.12.002. URL: <https://dx.doi.org/10.1016/j.sandf.2013.12.002>.
- [58] A. C. Collop, G. R. McDowell, and Y. Lee. “On the use of discrete element modelling to simulate the viscoelastic deformation behaviour of an idealized asphalt mixture”. In: *Geomechanics and Geoengineering* 2 (2007), pp. 77–86. ISSN: 1748-6025, 1748-6033. DOI: 10.1080/17486020701243128. URL: <https://dx.doi.org/10.1080/17486020701243128>.
- [59] Yu Liu, Qingli Dai, and Zhanping You. “Viscoelastic Model for Discrete Element Simulation of Asphalt Mixtures”. In: *Journal of Engineering Mechanics* 135 (2009), pp. 324–333. ISSN: 0733-9399, 1943-7889. DOI: 10.1061/(asce)0733-9399(2009)135:4(324). URL: [https://dx.doi.org/10.1061/\(asce\)0733-9399\(2009\)135:4\(324\)](https://dx.doi.org/10.1061/(asce)0733-9399(2009)135:4(324)).
- [60] Huan Feng, Matteo Pettinari, and Henrik Stang. “Study of normal and shear material properties for viscoelastic model of asphalt mixture by discrete element method”. In: *Construction and Building Materials* 98 (2015), pp. 366–375. ISSN: 0950-0618. DOI: 10.1016/j.conbuildmat.2015.08.116. URL: <https://dx.doi.org/10.1016/j.conbuildmat.2015.08.116>.
- [61] H. A. Barnes. *A Handbook of Elementary Rheology*. Institute of Non-Newtonian Fluid Mechanics, University of Wales, 2000.
- [62] Grzegorz Mazurek and Marek Iwański. “Modelling of Asphalt Concrete Stiffness in the Linear Viscoelastic Region”. In: *IOP Conference Series: Materials Science and Engineering* 245 (2017), p. 032029. ISSN: 1757-8981, 1757-899X. DOI: 10.1088/1757-899x/245/3/032029. URL: <https://dx.doi.org/10.1088/1757-899x/245/3/032029>.
- [63] H. Feng, M. Pettinari, and H. Stang. “8th RILEM International Symposium on Testing and Characterization of Sustainable and Innovative Bituminous Materials”. In: RILEM. Elsevier, 2015, pp. 423–433.
- [64] Yu Liu and Zhanping You. “Determining Burger’s Model Parameters of Asphalt Materials Using Creep-Recovery Testing Data”. In: *Pavements and Materials* (2008). DOI: 10.1061/41008(334)3. URL: [https://dx.doi.org/10.1061/41008\(334\)3](https://dx.doi.org/10.1061/41008(334)3).

- [65] Huanan Yu and Shihui Shen. “A micromechanical based three-dimensional DEM approach to characterize the complex modulus of asphalt mixtures”. In: *Construction and Building Materials* 38 (2013), pp. 1089–1096. ISSN: 0950-0618. DOI: 10.1016/j.conbuildmat.2012.09.036. URL: <https://dx.doi.org/10.1016/j.conbuildmat.2012.09.036>.
- [66] John L. Gustafson. “Brent’s Theorem”. In: *Encyclopedia of Parallel Computing*. Ed. by David Padua. Boston, MA: Springer US, 2011, pp. 182–185. ISBN: 978-0-387-09766-4. DOI: 10.1007/978-0-387-09766-4_80. URL: https://doi.org/10.1007/978-0-387-09766-4_80.
- [67] He Wang et al. “Development of two-dimensional micromechanical, viscoelastic, and heterogeneous-based models for the study of block cracking in asphalt pavements”. In: *Construction and Building Materials* 244 (2020), p. 118146. ISSN: 0950-0618. DOI: 10.1016/j.conbuildmat.2020.118146. URL: <https://dx.doi.org/10.1016/j.conbuildmat.2020.118146>.
- [68] Elena V. Vashuk et al. “Water-absorbing properties of hydrogels based on polymeric complexes”. In: *Materials Research Innovations* 4 (2001), pp. 350–352. ISSN: 1432-8917, 1433-075X. DOI: 10.1007/s100190000115. URL: <https://dx.doi.org/10.1007/s100190000115>.
- [69] Van Nga Nguyen et al. “Rheological characterization of mechanical properties of chemically crosslinked microspheres”. In: *Journal of Applied Polymer Science* 128 (2012), pp. 3113–3121. ISSN: 0021-8995, 1097-4628. DOI: 10.1002/app.38510. URL: <https://dx.doi.org/10.1002/app.38510>.
- [70] Xiuhua Zeng et al. “Real-time quantitative measurement of mechanical properties of spherical hydrogels during degradation by hydrodynamic loading and numerical simulation”. In: *Polymer Degradation and Stability* 202 (2022), p. 110055. ISSN: 0141-3910. DOI: 10.1016/j.polymdegradstab.2022.110055. URL: <https://dx.doi.org/10.1016/j.polymdegradstab.2022.110055>.
- [71] K. Giannis et al. “Stress based multi-contact model for discrete-element simulations”. In: *Granular Matter* 23 (2021). ISSN: 1434-5021, 1434-7636. DOI: 10.1007/s10035-020-01060-8. URL: <https://dx.doi.org/10.1007/s10035-020-01060-8>.
- [72] Nazanin Ghods et al. “Discrete element modeling of strongly deformed particles in dense shear flows”. In: *Powder Technology* 401 (2022), p. 117288. ISSN: 0032-5910. DOI: 10.1016/j.powtec.2022.117288. URL: <https://dx.doi.org/10.1016/j.powtec.2022.117288>.
- [73] Michael Mascara et al. “Implementation and validation of a bonded particle model to predict rheological properties of viscoelastic materials”. In: *Particuology* 89 (2024), pp. 198–210. ISSN: 1674-2001. DOI: 10.1016/j.partic.2023.11.001. URL: <https://dx.doi.org/10.1016/j.partic.2023.11.001>.

- [74] J. N. M. Boots et al. “Development of a multi-position indentation setup: Mapping soft and patternable heterogeneously crosslinked polymer networks”. In: *Review of Scientific Instruments* 90 (2019). ISSN: 0034-6748, 1089-7623. DOI: 10.1063/1.5043628. URL: <https://dx.doi.org/10.1063/1.5043628>.
- [75] Vahid Asadi et al. “Tuning moduli of hybrid bottlebrush elastomers by molecular architecture”. In: *Materials & Design* 234 (2023), p. 112326. ISSN: 0264-1275. DOI: 10.1016/j.matdes.2023.112326. URL: <https://dx.doi.org/10.1016/j.matdes.2023.112326>.
- [76] W. P. Cox and E. H. Merz. “Correlation of dynamic and steady flow viscosities”. In: *Journal of Polymer Science* 28 (1958), pp. 619–622. ISSN: 0022-3832, 1542-6238. DOI: 10.1002/pol.1958.1202811812. URL: <https://dx.doi.org/10.1002/pol.1958.1202811812>.
- [77] T. Bakri, R. Nabergoj, and A. Tondl. “Multi-frequency oscillations in self-excited systems”. In: *Nonlinear Dynamics* 48 (2006), pp. 115–127. ISSN: 0924-090X, 1573-269X. DOI: 10.1007/s11071-006-9077-1. URL: <https://dx.doi.org/10.1007/s11071-006-9077-1>.
- [78] Nicholas L. Cuccia et al. “Pore-size dependence and slow relaxation of hydrogel friction on smooth surfaces”. In: *Proceedings of the National Academy of Sciences* 117 (2020), pp. 11247–11256. ISSN: 0027-8424, 1091-6490. DOI: 10.1073/pnas.1922364117. URL: <https://dx.doi.org/10.1073/pnas.1922364117>.
- [79] Francisco Javier Castro and Stefan Radl. “A combined SPH-DEM approach for extremely deformed granular packings: validation and compression tests”. In: *Computational Particle Mechanics* (2023). ISSN: 2196-4378, 2196-4386. DOI: 10.1007/s40571-023-00616-8. URL: <https://dx.doi.org/10.1007/s40571-023-00616-8>.
- [80] Nathan Berry, Yonghao Zhang, and Sina Haeri. “Contact models for the multi-sphere discrete element method”. In: *Powder Technology* 416 (2023), p. 118209. ISSN: 0032-5910. DOI: 10.1016/j.powtec.2022.118209. URL: <https://dx.doi.org/10.1016/j.powtec.2022.118209>.
- [81] Y. Fukunishi et al. “Attempt to Suppress Numerical Viscosity in Incompressible SPH Method”. In: *Journal of Applied Fluid Mechanics* 12 (2019), pp. 1231–1240. DOI: 10.29252/jafm.12.04.29633.
- [82] Nicolas Brodu, Joshua A. Dijksman, and Robert P. Behringer. “Multiple-contact discrete-element model for simulating dense granular media”. In: *Physical Review E* 91 (2015). ISSN: 1539-3755, 1550-2376. DOI: 10.1103/physreve.91.032201. URL: <https://dx.doi.org/10.1103/physreve.91.032201>.
- [83] B. F. Gorin. “Impacts of drops and soft solids”. Ph.D. thesis. University van Amsterdam, 2024.

- [84] Yifei Duan and Zhi-Gang Feng. “Incorporation of velocity-dependent restitution coefficient and particle surface friction into kinetic theory for modeling granular flow cooling”. In: *Physical Review E* 96 (2017), Not available. ISSN: 2470-0045, 2470-0053. DOI: 10.1103/physreve.96.062907. URL: <https://dx.doi.org/10.1103/physreve.96.062907>.
- [85] Chandan Shakya, Jasper van der Gucht, and Joshua A. Dijksman. “Viscoelastic material properties determine the contact mechanics of hydrogel spheres”. In: *Frontiers in Physics* 12 (2024). DOI: 10.3389/fphy.2024.1334325.
- [86] Przemysław Pietrzak, Michal Meller, and Maciej Niedźwiecki. “Dynamic mass measurement in checkweighers using a discrete time-variant low-pass filter”. In: *Mechanical Systems and Signal Processing* 48 (2014), pp. 67–76. DOI: 10.1016/j.ymssp.2014.02.013.